

Alma Mater Studiorum - Università di Bologna

**DOTTORATO DI RICERCA IN
AUTOMOTIVE PER UNA MOBILITÀ INTELLIGENTE**

Ciclo XXXV

Settore Concorsuale: 09/E2 - INGEGNERIA DELL'ENERGIA ELETTRICA
Settore Scientifico Disciplinare: ING-IND/32 - CONVERTITORI, MACCHINE E
AZIONAMENTI ELETTRICI

**HIGH PERFORMANCE BATTERY CHARGERS FOR
FULL ELECTRIC AND HYBRID CARS**

Presentata da: Alessandro Campanini

Coordinatore Dottorato
Nicolò Cavina

Supervisore
Claudio Rossi
Co-supervisore
Mattia Ricco

Esame finale anno 2023

"My best race? Still to come. I believe in moving forwards and moving on. Time is a one way street, and I want to go with the times. Looking back is only going to slow you down."

Sebastian Vettel

Abstract

This Doctoral Thesis aims to study and develop advanced and high-efficient battery chargers for full electric and plug-in electric cars. The document is strictly industry-oriented and relies on automotive standards and regulations. In the first part a general overview about wireless power transfer battery chargers (WPTBCs) and a deep investigation about international standards are carried out. Then, due to the highly increasing attention given to WPTBCs by the automotive industry and considering the need of minimizing weight, size and number of components this work focuses on those architectures that realize a single stage for on-board power conversion avoiding the implementation of the DC/DC converter upstream the battery. Based on the results of the state-of-the-art, the following sections focus on two stages of the architecture: the resonant tank and the primary DC/AC inverter. To reach the maximum transfer efficiency while minimizing weight and size of the vehicle assembly a coordinated system level design procedure for resonant tank along with an innovative control algorithm for the DC/AC primary inverter is proposed. The presented solutions are generalized and adapted for the best trade-off topologies of compensation networks: Series-Series and Series-Parallel. To assess the effectiveness of the above-mentioned objectives, validation and testing are performed through a simulation environment, while experimental test benches are carried out by the collaboration of Delft University of Technology (TU Delft).

Index Terms: Automotive, battery electric cars, plug-in cars, hybrid cars, battery chargers, wireless power transfer, power electronics, control algorithms.

Acknowledgements

First and foremost, I would like to express my gratitude to my supervisor Prof. Claudio Rossi for his great support, guidance and mentoring. I would also like to thank my technical mentor Ing. Matteo Marano for his valuable time, kindness and contribution. I big thanks also to all the people present at the LEMAD laboratory. I really enjoyed working with all of you.

A special thanks to Ing. Mattia Simonazzi for sharing the daily challenges and for the very fruitful collaboration. I am grateful also to all the other colleagues and friends who I worked with along this journey.

Over the last year I had the chance and pleasure to collaborate with Silk-FAW Automotive Group Italy and McLaren Applied UK. These experiences enriched my knowledge and my experience as a researcher and as an expert in the field.

Finally, without taking anything away from everyone else, the biggest thanks goes to my family and to my girlfriend for unconditional love and always supporting my choices no matter what.

Alessandro Campanini

Bologna, Italy

October, 2022

Contents

Abstract	i
Acknowledgements	ii
Contents	iv
List of Figures	xi
List of Tables	xiii
Nomenclature	xiv
1 Introduction	1
1.1 Motivations	1
1.2 Scope and Contribution of the Thesis	2
1.3 Thesis Outline	3
2 Fundamentals of Battery Chargers	4
2.1 Problem Background	4
2.2 Wireless Battery Chargers Overview	7
2.2.1 International Standards	8
2.2.2 SAE J2954 Reference Standard	9
3 Resonant Tank Optimization	15
3.1 Resonant Tank System Requirements	15
3.2 Mathematical Description	17
3.2.1 Matching Coils	17

3.2.2	Resonant Tank	21
3.2.3	Generalized Approach for Efficiency Calculation	24
3.2.4	Load Modelling	26
3.3	Design Methodology	30
3.3.1	Series-Parallel (S-P)	32
3.3.2	Series-Series (S-S)	46
4	Power Electronics Control Optimization	53
4.1	Power Electronics Circuit Topology	53
4.2	Power Electronics Control Techniques	58
4.3	Primary Inverter Control	61
4.3.1	S-P Compensation	61
4.3.2	S-S Compensation	75
5	Results and Discussion	81
5.1	Resonant Tank Outcomes	82
5.1.1	S-P Compensation	82
5.1.2	S-S Compensation	87
5.2	Power Electronics Control Outcomes	91
5.2.1	S-P Compensation	94
5.2.2	S-S Compensation	97
5.3	System Comparison	100
5.3.1	Energy Assessment	104
6	Conclusions and Future Work	108
6.1	Conclusions	108
6.2	Future Work	109
	Bibliography	120

List of Figures

2.1	Greenhouse gas emissions in the World and in EU, with a focus on to the transportation sector. Greenhouse gas emissions are measured in tonnes of carbon dioxide-equivalents (CO ₂ e).	6
2.2	Functional block diagram of IPT systems for electric vehicles.	7
2.3	Definition of coil ground distance.	12
2.4	Typical functional elements of wireless charging system.	12
2.5	Vehicle proximity detection.	13
2.6	EMF and contact current limit region (a) top view and (b) front view.	14
3.1	DC/DC power conversion stage for a WPT battery charger system. The dotted converter upstream the battery might be avoided if the system is properly designed.	16
3.2	Transformer representation of WPT matching coils for (a) electrical circuitry based on self-inductances and mutual inductance, while (b) avoiding the use of system parameters and defining the voltage ration n	18
3.3	T model representation of WPT matching coils.	18
3.4	T model representation with leakage inductances.	19
3.5	Updating of (a) transformer model and (b) T model according to leakage inductances for WPT resonant tank.	19
3.6	Equivalent load impedance seen at the output terminals of the resonant tank for a) series compensation and b) parallel compensation.	22
3.7	Integration of both primary compensation capacitor and equivalent impedance load into a matching coils network.	23

3.8	Resonant tank efficiency stages. Matching coils are represented by a transformer T model.	25
3.9	Simplified high frequency WPT circuit for generalized efficiency calculation.	25
3.10	Experimental data from CC-CV charging cycle of Molicel INR-21700-P42B cell for a 100S battery pack configuration and SAE J2954 WPT1. The time is normalized with respect to the end-of-charge time.	28
3.11	Battery power and load resistance variation for (a) complete CC-CV charging cycle and (b) with zoomed scale for the CC region. The time is normalized with respect to the end-of-charge time.	29
3.12	Flowchart for S-P compensation illustrating the design procedure for constant output voltage. The load resistance R_l and the coupling coefficient k refer to actual parameters during variable operating conditions.	35
3.13	Voltage gain behavior for S-P compensation at (a) different equivalent loads (b) different coupling coefficients, for a load of $R_{ac} = 60[\Omega]$. . .	37
3.14	Transconductance gain behavior for S-P compensation at (a) different equivalent loads (b) different coupling coefficients, for a load of $R_{ac} = 60[\Omega]$	37
3.15	Equivalent input impedance seen at the terminals of the primary side, which corresponds to the middle point outputs of the inverter legs. (a) Input impedance module and (b) input impedance phase angle. . .	38
3.16	Effects of sensitivity analysis when changing the reference resonant frequency for (a) voltage gain for different loads (b) voltage gain for different coupling coefficients (c) transconductance gain for different loads (d) transconductance gain for different coupling coefficients (e) input impedance module and (f) input impedance phase angle. The reference resonant frequency is set to 86 kHz.	39

3.17	Effects of sensitivity analysis when changing the reference maximum voltage gain for (a) voltage gain for different loads (b) voltage gain for different coupling coefficients (c) transconductance gain for different loads (d) transconductance gain for different coupling coefficients (e) input impedance module and (f) input impedance phase angle. The reference maximum voltage gain is set to 0.9.	41
3.18	Effects of sensitivity analysis when changing the reference coupling coefficient for (a) voltage gain for different loads (b) voltage gain for different coupling coefficients (c) transconductance gain for different loads (d) transconductance gain for different coupling coefficients (e) input impedance module and (f) input impedance phase angle. The reference coupling coefficient is set to 0.22.	43
3.19	Effects of sensitivity analysis when changing the reference equivalent for (a) voltage gain for different loads (b) voltage gain for different coupling coefficients (c) transconductance gain for different loads (d) transconductance gain for different coupling coefficients (e) input impedance module and (f) input impedance phase angle. The reference equivalent load is set to 60 [Ω].	45
3.20	Flowchart for S-S compensation illustrating the design procedure for constant output current. The load resistance R_l and the coupling coefficient k refer to actual parameters during variable operating conditions.	48
3.21	Voltage gain behavior for S-S compensation at (a) different equivalent loads (b) different coupling coefficients, for a load of $R_{ac} = 40[\Omega]$. . .	50
3.22	Transconductance gain behavior for S-S compensation at (a) different equivalent loads (b) different coupling coefficients, for a load of $R_{ac} = 40[\Omega]$	51
3.23	Equivalent input impedance seen at the terminals of primary side, which corresponds to the middle point outputs of the inverter legs. (a) Input impedance module and (b) input impedance phase angle. .	51

4.1	Power electronics stages for WPTBCs.	54
4.2	Current-fed converter.	55
4.3	Matrix converter for G2V applications.	56
4.4	Multiphase converter for G2V applications.	56
4.5	Modular high power converter for G2V applications.	57
4.6	Parallel LCL-T topology for high-power G2V applications.	57
4.7	Cascade multilevel converter for G2V applications.	58
4.8	Single stage system architecture for power electronic control of (a) S-P compensation and (b) S-S compensation.	59
4.9	Frequency control scheme.	63
4.10	(a) Sampled battery voltage and battery current operating points at reference coupling coefficient k_0 . (b) Optimum transconductance gain to match the reference battery current and the input voltage. (c) Operating frequency in S-P compensation under FC, for controlling the battery current.	64
4.11	Total gain \hat{G}_{Tr} for different phase-shift values, calculated at reference coupling coefficient k_0 . Three different equivalent loads are considered: (a) $R_{ac,min}$, (b) $R_{ac}@P_{max}$, (c) $R_{ac,max}$	66
4.12	Phase-shift control scheme.	67
4.13	Selected operating point by the PSC control scheme for (a) transconductance gain, (b) total gain and finally (c) shows the delta values.	68
4.14	Turn-off process of MOSFET switch S_1	70
4.15	Hybrid phase-shift and frequency control flowchart for primary inverter control.	73
4.16	Hybrid control algorithm outputs showing, as a function of the load, (a) the frequency values and (b) the phase-shift values.	74
4.17	Hybrid control algorithm outputs showing (a) the resulting frequency phase-shift 2D map and (b) 3D representation of the frequency and phase-shift map for the N pairs for any operating point.	75

4.18	(a) Sampled battery voltage and battery current operating points at reference coupling coefficient k_0 . (b) Optimum transconductance gain to match the reference battery current and the input voltage. (c) Operating frequency in S-S compensation under FC, for controlling the battery current.	76
4.19	Total gain \hat{G}_{Tr} for different phase-shift values and for S-S compensation, calculated at reference coupling coefficient k_0 . Three different equivalent loads are considered: (a) $R_{ac,min}$, (b) $R_{ac}@P_{max}$, (c) $R_{ac,max}$	77
4.20	Selected operating point by the PSC control scheme for (a) transconductance gain, (b) total gain and finally (c) shows the delta values for S-S compensation.	78
4.21	Hybrid control algorithm outputs showing, as a function of the load, (a) the frequency values and (b) the phase-shift values for S-S compensation.	79
4.22	Hybrid control algorithm outputs showing (a) the resulting frequency phase-shift 2D map and (b) 3D representation of the frequency and phase-shift map for the N pairs for any operating point for S-S compensation.	80
5.1	Resonant tank optimum primary and secondary inductance variation, according to reference parameters for S-P compensation. Figures (a), (c), (e) show both parameters, while figures (b), (d), (f) zoom the secondary inductance variation.	84
5.2	Resonant tank optimum primary and secondary capacitance variation, according to reference parameters for S-P compensation. Figures (a), (c), (e) show both parameters, while figures (b), (d), (f) zoom the primary capacitance variation.	85

5.3	Efficiency evaluation for S-P compensation as a function of the frequency for (a) different loads in a wide frequency range, (b) different loads in the SAE J2954 range, (c) different coupling coefficients in a wide frequency range and (d) different coupling coefficients in the SAE J2954 range.	87
5.4	Resonant tank optimum primary and secondary side inductances and capacitances variation, for S-S compensation, as a function of (a) and (b) reference frequency, (c) and (d) reference coupling coefficient, (e) and (f) reference load.	89
5.5	Efficiency evaluation for S-S compensation as a function of the frequency for (a) different loads in a wide frequency range, (b) different loads in the SAE J2954 range, (c) different coupling coefficients in a wide frequency range and (d) different coupling coefficients in the SAE J2954 range.	90
5.6	Experimental prototype realized by Delft University of Technology. Transmitting and receiving coils are shown in (a) front view, while (b) shows a different angulation and includes pad dimensions.	92
5.7	Experimental prototype realized by Delft University of Technology. (a) Primary inverter and LaunchPad while (b) H-bridge diodes rectifiers.	93
5.8	The resulting frequency and phase-shift value of the HPSFC are benchmarked with (a) FC and (b) PSC for S-P compensation.	95
5.9	(a) Efficiency of the proposed HPSFC compared with stand-alone FC and PSC, while (b) highlights the improvement between HPSFC and PSC.	96
5.10	(a) 3D efficiency-frequency-load map for S-P compensation, while (b) highlights the frequency influence and (c) the load influence.	97
5.11	The resulting frequency and phase-shift value of the HPSFC are benchmarked with (a) FC and (b) PSC for S-S compensation.	98
5.12	(a) Efficiency of the proposed HPSFC compared with stand-alone FC and PSC, while (b) highlights the improvement between HPSFC and PSC for S-S compensation.	99

5.13 (a) 3D efficiency-frequency-load map for S-P compensation, while (b) highlights the frequency influence and (c) the load influence for S-S compensation.	100
5.14 Cumulative energy assessment for (a) S-S compensation and for (b) S-P compensation. Time is normalized with respect to the time of end of charge.	105
5.15 Bar chart in [p.u.]	107

List of Tables

2.1	International standards for WPT for BEV and PHEV.	9
2.2	WPT power and frequency levels according to SAE J2954.	10
2.3	WPT interoperability classes according to power levels, as defined by SAE J2954.	11
2.4	WPT ground clearance range according to SAE J2954.	11
2.5	PT misalignment distance according to SAE J2954.	11
2.6	Magnetic field, electric field and contact current exposure standard level.	14
3.1	T model matching coils system parameters.	18
3.2	System parameters of Fig. 3.4.	19
3.3	Battery pack parameters for BEVs and PHEVs, considering the cell "Molicel INR-21700-P42B".	27
3.4	Representative resistance values in a complete CC-CV charging cycle for WPT1 class, adpoting a 100S battery pack configuration for BEVs and PHEVs.	29
3.5	System specifications for the resonant tank design.	32
3.6	System parameters, for S-P compensation, obtained from the opti- mum design procedure.	36
3.7	System parameters, for S-S compensation, obtained from the opti- mum design procedure.	49
5.1	S-P compensated resonant tank dependency to reference parameters.	82
5.2	S-S compensated resonant tank dependency to reference parameters. .	88
5.3	Components mounted on the experimental set-up.	91

5.4	C2000 Delfino DSP characteristics.	94
5.5	Comparison between resonant tank parameters of S-P and S-S compensation.	102
5.6	Efficiency comparison including resonant tank and primary inverter control, between S-P and S-S compensation.	104
5.7	Energy values for each control techniques, for both compensation topologies, normalized with respect to the reference battery energy of 85 kW/h.	106

Nomenclature

List of Acronyms

EV	Electric Vehicle
BEV	Battery Electric Vehicle
PHEV	Plug-in Electric Vehicle
WPT	Wireless Power Transfer
CC-CV	Constant-Current Constant-Voltage
ZVS	Zero Voltage Switching
BC	Battery Charger
WPTBC	Wireless Power Transfer Battery Charger
CO ₂	Carbon Dioxide
CO ₂ e	Carbon Dioxide Equivalents
DC	Direct Current
AC	Alternating Current
EU	European Union
IPT	Inductive Power Transfer
PF	Power Factor
GA	Ground Assembly
VA	Vehicle Assembly
EMF	Electro Magnetic Field
RMS	Root Mean Square
S-S	Series-Series
S-P	Series-Parallel
HVAC	Heat Ventilation and Air Conditioning

NMC	Nickel Manganese Cobalt
LiFePo4	Lithium Iron Phosphate
P-S	Parallel-Series
P-P	Parallel-Parallel
ZPA	Zero Phase Angle
MIMO	Multiple-input-multiple-output
THD	Total Harmonic Distortion
G2V	Grid to Vehicle
V2G	Vehicle to Grid
FC	Frequency Control
PSC	Phase-shift Control
HPSFC	Hybrid Phase-shift Frequency Control
MPPT	Maximum Power Point Tracking
PI	Proportional Integral
BMS	Battery Management System
LEMAD	Laboratory of Electrical Machines and Drives

List of Symbols

L_1	Primary self-inductance	[H]
L_2	Secondary self-inductance	[H]
C_1	Primary compensation capacitor	[F]
C_2	Secondary compensation capacitor	[F]
M	Mutual inductance	[H]
k	Coupling coefficient	-
N_1	Number of primary turns	-
N_2	Number of secondary turns	-
n	Turn ratio	-
V_1	Resonant tank primary voltage	[V]
V_2	Resonant tank secondary voltage	[V]
V_{dc}	DC bus rated voltage	[V]
I_1	Resonant tank primary current	[A]
I_2	Resonant tank secondary current	[A]
L_{lk1}	Primary leakage inductance	[F]
L_{lk2}	Secondary leakage inductance	[F]
L_μ	Magnetizing inductance	[F]
L'_{lk1}	Primary leakage inductance referred to primary side	[F]
L'_{lk2}	Secondary leakage inductance referred to primary side	[F]
L'_μ	Magnetizing inductance referred to primary side	[F]
V'_2	Resonant tank secondary voltage referred to primary side	[V]
j	Imaginary unit	-
f	Frequency	[Hz]
ω	Angular frequency	[rad/s]
Z_{ac}	Equivalent load impedance at secondary side terminals	[Ω]
G_v	Voltage gain	-
R_1	Primary lumped equivalent series resistance	[Ω]
R_2	Secondary lumped equivalent series resistance	[Ω]

R_{load}	Load resistance	[Ω]
V_{batt}	Battery pack voltage	[V]
P_{batt}	Battery pack power	[W]
Z_1	Primary impedance	[Ω]
Z_2	Secondary impedance	[Ω]
G_{tr}	Transconductance gain	-
P_1	Resonant tank input power	[W]
P_1	Resonant tank output power	[W]
η_{tot}	Total resonant tank efficiency	-
η_{pc}	Primary compensation network efficiency	-
η_p	Primary side efficiency	-
η_s	Secondary side efficiency	-
η_{sc}	Secondary compensation network efficiency	-
N_s	Series cells	-
N_p	Parallel cells	-
$V_{c,rated}$	Cell rated voltage	[V]
$V_{c,min}$	Cell minimum voltage	[V]
$V_{c,max}$	Cell maximum voltage	[V]
$C_{c,rated}$	Cell rated capacity	[Ah]
$V_{batt,min}$	Battery minimum voltage	[V]
$V_{batt,max}$	Battery maximum voltage	[V]
I_{cc}	CC reference current	[A]
$R_{ac,SP}$	Equivalent S-P load resistance	[Ω]
$R_{ac,SS}$	Equivalent S-S load resistance	[Ω]
f_0	Resonant frequency	[Hz]
Q_1	Primary inductor quality factor	-
Q_2	Secondary inductor quality factor	-
η_{link}	Resonant tank efficiency	-
ω_1	Primary angular frequency	[rad/s]
ω_2	Secondary angular frequency	[rad/s]

$R_{ac,0}$	Reference equivalent load resistance	[Ω]
f_0	Reference frequency	[Hz]
fk_0	Reference coupling coefficient	-
$G_{v,0}$	Reference voltage gain	-
$L_{1,opt}$	Optimum primary self-inductance	[H]
$L_{2,opt}$	Optimum secondary self-inductance	[H]
$C_{1,opt}$	Optimum primary compensation capacitor	[F]
$C_{2,opt}$	Optimum secondary compensation capacitor	[F]
S_i	Switch i	-
S_a	MOSFET gate signal	-
Z_{in}	Equivalent impedance seen at primary side	[Ω]
ϕ_{in}	Equivalent impedance angle	[deg]
δ	Phase-shift between inverter legs	[deg]
D	Duty cycle of primary inverter	-
G_{Tv}	Total voltage gain	-
G_{Ttr}	Total transconductance gain	-
η_i	Inverter efficiency	-
P_{cond}^{MOS}	MOSFETs total conduction losses	[W]
$R_{ds,on}$	MOSFET drain-source resistance	[Ω]
$P_{sw,off}^{MOS}$	MOSFETs total turn-off switching losses	[W]
$P_{sw,off}^{S_i}$	MOSFET i turn-off switching losses	[W]
$i_{off,i}$	MOSFET i turn-off current	[A]
$v_{ds,i}$	MOSFET i turn-off drain-source voltage	[V]
$i_{r,i}$	MOSFET i resonant current	[A]
$i_{disch,i}$	MOSFET i discharge current	[A]
C_{oss}	MOSFET output capacitance	[F]
R_g	MOSFET gate resistance	[Ω]
Q_{gd}	MOSFET gate-drain charge	[C]
v_{gs}	MOSFET Miller plateau voltage	[V]
t_f	MOSFET turn-off time	[s]

η_{dr}	H-bridge diode rectifiers efficiency	-
P_{cond}^{Diodes}	Diodes total conduction losses	[W]
$P_{sw,off}^{Diodes}$	Diodes total switching losses	[W]
V_F	Diode forward voltage	[V]
I_F	Diode forward current	[A]
E_{RR}	Diode energy loss per pulse	[J]
I_{RRM}	Diode peak recovery current	[A]
t_{rr}	Diode reverse recovery time	[s]

Chapter 1

Introduction

1.1 Motivations

Nowadays environmental issues and technological improvements have pushed towards the direction of investing in electric mobility. The last frontier of power electronics and modern lithium-ion batteries have made battery electric vehicles (BEVs) and plug-in electric vehicles (PHEVs) an efficient, low polluting and reliable alternative to traditional vehicles fed by fossil fuels. However, both BEVs and PHEVs suffer from problems related to charging time and therefore it becomes fundamental charging at high power. In this frame, the trend is to adopt power electronics components able to operate at high frequency, close to hundreds of kHz, reducing the switching losses and consequently reducing size, weight and allowing the power rating to be increased. On top of that, the transition from fuel-based cars to electric ones can also be supported by an easier and safer charging method: wireless power transfer (WPT). WPT systems for automotive applications are based on inductive coupling coils, fed by a high frequency current, which in turns generates the magnetic field necessary to transfer the power. However, switching at these frequencies while maintaining reasonable switching losses, is only possible when adopting SiC or GaN devices. When it comes to creating an innovative and highly optimized WPT battery charger, which avoids the implementation of the DC/DC converter upstream the battery, there are two main open issues in literature: the design of the WPT resonant tank and the control strategy of primary inverter, in order to minimize losses

and, at the same time, being able to follow the constant current - constant voltage (CC-CV) charging cycle required by lithium-ion cells. Furthermore, the solutions found in literature are often interesting concepts at a prototype level but hardly implementable with a low cost manufacturing process for industrialization.

1.2 Scope and Contribution of the Thesis

Considering the previous discussion, several combinations of resonant tank compensation topologies are available and analyzed in literature. Basic resonant topologies, such as Series-Series and Series-Parallel, have been deeply studied and compared. Parallel-Series and Parallel-Parallel are not of interest for battery charging applications since the voltage applied to the tank is imposed by the inverter. Series-Parallel combinations might be interesting solutions, but they require additional components, costs and complexity. Instead, for primary inverter there are mainly three categories of modulation strategies: frequency control, phase-shift or duty cycle control and hybrid phase-shift frequency control. These control techniques allow the inverter output voltage, which corresponds to the resonant tank input voltage, to be regulated even if it can lead to operations out of zero voltage switching (ZVS) or selecting frequency values that drop outside the SAE J2954 standard.

Therefore, the main purpose of this work has two main target objectives, necessary to overcome the actual limitations:

- Provide a general design procedure, including the coil design, based on maximizing the tank efficiency and minimizing the vehicle assembly self-inductance, considering and comparing design considerations and actual performance of Series-Series and Series-Parallel compensation network topology for automotive battery charging applications
- Propose an algorithm able to control both frequency and phase-shift of the primary inverter following a CC-CV charge cycle and avoiding using the on-board additional DC/DC converter. Main improvements are related to minimize the frequency range for achieving ZVS according to the converter operation and

to include effects produced by coils misalignment. In addition, an optimized relationship between phase-shift and frequency is proposed and the whole system efficiency is mapped for any load, allowing to select the best operation mode at any instant.

1.3 Thesis Outline

The remainder of thesis is to be structured as follows. In Chapter 2 a literature review is introduced, in order to get familiar with the basic concepts and background of the topic. Specifically, wireless power transfer battery chargers (WPTBCs) are covered. Thereafter, the introduced state-of-the-art resume is critically discussed in Chapter 3 and Chapter 4, with the aim to highlight the contribution of the thesis on the field and the consequent novelty of the work. With reference to WPTBCs, in Chapter 3 a general design procedure for the resonant tank with Series-Series and Series-Parallel compensation is introduced. Chapter 4 presents an innovative control technique for primary inverter, based on frequency modulation and phase-shift control of the inverter legs. Chapter 5 shows the obtained results, analyzes and compares them, with the aim to understand which architecture performs better than the others and under which conditions. The work is closed by Chapter 6, which contains both conclusions and considerations with some tips for suggested future works and improvements.

Chapter 2

Fundamentals of Battery Chargers

Two main topics are discussed in this section. First, a general overview of the challenges for reducing greenhouse gases emission and pollution of light duty vehicles through electrification is discussed. Then, Wireless Power Transfer Battery Chargers are introduced. The overview covers the state-of-the-art architecture, including the most common system topologies, power rating and some indications to comply with the international standards in order to commercialize the product. Then, proceeding through the Chapter, the third and fourth sections introduce two main open issues when designing a WPTBC: the resonant tank compensation network and system topologies of power electronic converters. The above-mentioned third and fourth items are the core of this thesis and therefore they are deeply investigated, including analysis and comparison of PROs and CONs in Chapter 3 and Chapter 4.

2.1 Problem Background

In the twenty-first century, one of the biggest challenges for preserving the health of the environment is certainly correlated to the fight against climate change. As a matter of fact, the average Earth temperature is increasing significantly faster than temperature swings registered in the past and the trend is not promising. Recent research highlights that a raise of 2°C would lead to a heavy and beyond repair climate impact [1]. Scientists working on the field have correlated the greenhouse gas emission with the Earth temperature increase, also affecting the quality of life,

especially for those who live in crowded cities [2]. Light duty vehicles, also called passenger cars, are emitting around 12% (data from 2014) of total EU emissions of carbon dioxide (CO_2), which can be addressed as the main greenhouse gas. If vans and heavy duty vehicles are included into the statistic, the number rises above 20% [3]. As shown in Fig. 2.1 the transportation sector's contribution to greenhouse gas emission over the years is not negligible, emitting up to one billion tons of CO_2 per year. A noticeable action against greenhouse gases emission must be taken. Assuming a more green energy production in the near future, a movement towards sustainable transportation is a clear need. A good signal can be seen in the annual growth of market of Electric Vehicles (EVs) market, which has risen above 40% year-on-year from 2010 [4].

As of today, the biggest technological challenges in the EV industry, are related to energy storage and charging infrastructure [6]. However, a much faster trajectory is essential if the 2030 sustainability target goals for CO_2 emissions are to be met. EU aims at reducing the net human-caused emissions of carbon dioxide (CO_2) by at least 55% from the 2010 levels by 2030, reaching 'net zero' around 2050 [3].

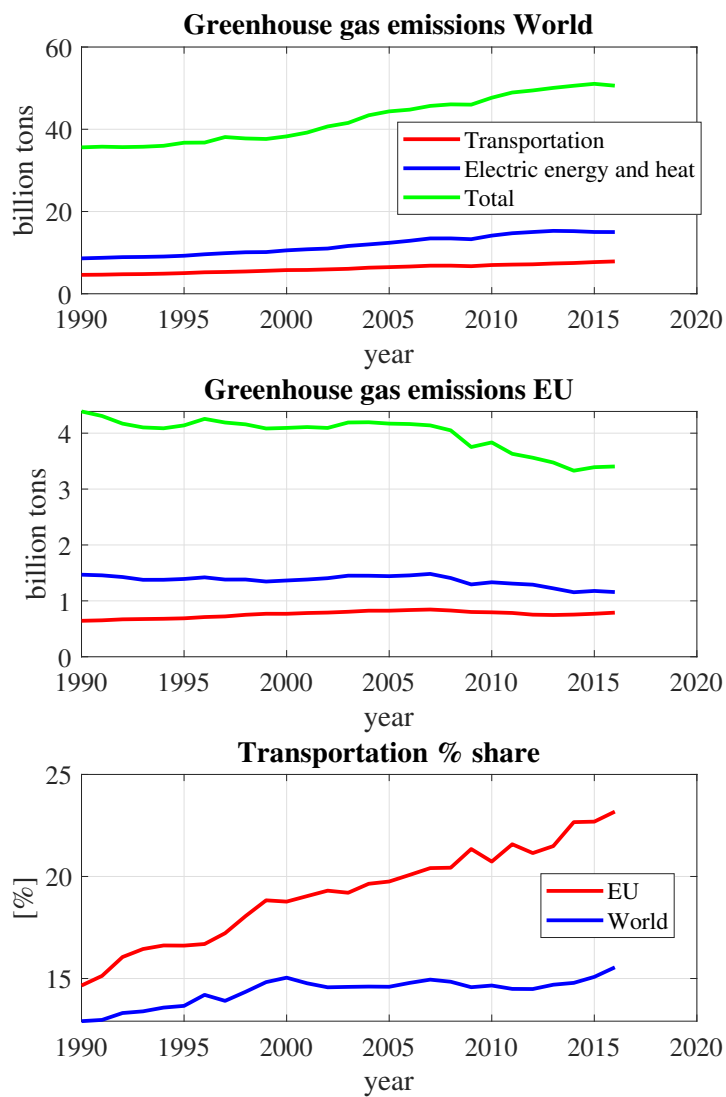


Figure 2.1: Greenhouse gas emissions in the World and in EU, with a focus on to the transportation sector. Greenhouse gas emissions are measured in tonnes of carbon dioxide-equivalents (CO_2e) [5].

2.2 Wireless Battery Chargers Overview

The transition from fuel-based cars to electric ones can be supported by an easier and safer charging method: wireless power transfer. WPT systems for automotive applications are based on inductive coupling coils, fed by a high frequency current at about 100 kHz, which in turns generates the magnetic field necessary to transfer the power. However, commutating at these frequencies while maintaining reasonable switching losses, is only possible when adopting SiC or GaN devices [7]. Fig. 2.2 illustrates the traditional state-of-the-art system architecture, from the grid to the battery, for Inductive Power Transfer (IPT) [8, 9]. The bottom side of the figure represents the off-board part, composed of a front-end AC/DC to correct the power factor (PF) and to regulate the AC supply from the electrical network together with the DC/AC inverter which fed the primary-compensated transmitter coil, also called ground assembly (GA). Then, the top side includes the secondary-compensated receiver coil, known as a vehicle assembly (VA), passing through the AC/DC converter, which might be either a double stage composed of active (or passive) rectifier plus a DC/DC converter or a single stage AC/DC. In both cases it is in charge of regulating the voltage and the current provided by the resonant tank to the ones requested by the battery to follow the constant-current constant-voltage (CC-CV) charging cycle.

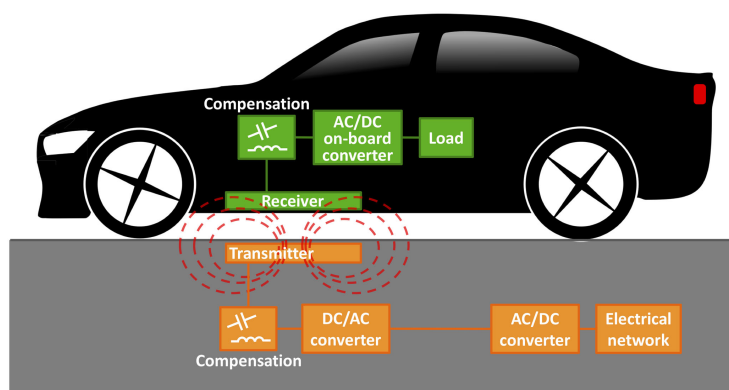


Figure 2.2: Functional block diagram of IPT systems for electric vehicles [8].

A significant advantage of WPT systems is the absence of signal and power electrical contacts. Thanks to this feature the GA and VA are independent and

the recharge process is automatically triggered by the vehicles as soon as it reaches the proximity detection point and the recharge process starts autonomously. This arrangement remarkably increases the safety levels operations and reduces the possibility of vandalism. In addition, when the system works in harsh environments the connection is automatically integrated into the protection against environmental conditions (e.g., water, dirt, chemicals, etc.) and the well known issues of erosion and dust deposition, reducing the maintenance costs and providing a more robust, stable and secure system with a longer life cycle [8, 9, 10].

2.2.1 International Standards

Although there is no unique international standard for WPT charging and there are many in existence, the most common one is the SAE J2954 [11]. It addresses most of the issues related to WPT such as alignment description, interoperability, frequency range of primary inverter operation and finally it classifies the WPT systems into three categories of power levels. Even though, for the sake of completeness, major standards are reported in Tab. 2.1, in the following SAE J2954 is taken as a reference.

Table 2.1: International standards for WPT for BEV and PHEV [9], [12, 13, 14, 15].

<i>Standard</i>	<i>Description</i>
SAE J2954	Wireless power transfer for light-duty plug-in/electric vehicles and alignment methodology
ICNIRP2010	Guidelines for limiting exposure to time-varying electric and magnetic fields (1 Hz to 100 kHz)
IEEE C95-123	IEEE standard for safety levels concerning human exposure to radio frequency electromagnetic fields, 3 kHz to 300 GHz
ISO 19363	Electrically propelled road vehicles - magnetic field wireless power transfer - safety and interoperability requirements
ISO 15118-1	Road vehicles - vehicle to grid communication interface - Part 1: general information and use-case definition
ISO 15118-2	Road vehicles - vehicle to grid communication interface - Part 2: network and application protocol requirements
ISO 15118-8	Road vehicles - vehicle to grid communication interface - Part 8: physical layer and data link layer requirements for wireless communication

2.2.2 SAE J2954 Reference Standard

System Requirements for WPTBCs

Only the system-level excerpts necessary to design, simulate, build and test the WPTBC prototype are discussed below. They all are based on SAE J2954 reference standard. Additional information can be found on [11].

According to SAE J2954 several WPT power classes have been defined [11, 16]. They are classified based on four power levels, from 3.7 kW to 22 kW and summarized in Tab. 2.2. WPT1 is mainly dedicated to household recharging, due to the fact that the maximum available power is 3.7 kW, which corresponds to the limit imposed by authorities. From WPT2 to WPT4 the power increases from 7.7 kW,

passing from 11.1 kW and ending to the highest power rate, 22 kW. However, to each of those levels it corresponds a minimum system efficiency that must be guaranteed during recharging process. In addition, switching devices must switch in a well defined frequency range, in between 81kHz and 90kHz. It leads the compensation network to resonate in the same frequency range. The resonant frequency design is in the middle of that range, at about 85kHz, and the frequency range allows the resonant tank to increase the efficiency according to the load at any time [11].

Table 2.2: WPT power and frequency levels according to SAE J2954 [9, 11], [16].

	<i>WPT1</i>	<i>WPT2</i>	<i>WPT3</i>	<i>WPT4</i>
Maximum input power	3.7kW	7.7kW	11.1kW	22kW
Maximum target efficiency	>85%	>85%	>85%	TBD
Minimum target efficiency at offset position	>80%	>80%	>80%	TBD
Frequency range	Resonance at 85kHz within the band (79-90)kHz			

In addition, as shown in Tab. 2.3 interoperability between GAs and VAs is required, associated to power classes from WPT1 to WPT3. For instance, when considering a GA rated for WPT2 it is required that it operates with GAs rated for WPT1 and WPT2 at the maximum power of the GA, while for WPT3 the GA must work as well but with a limited power according to the maximum value of GA WPT2 class. During power transfer between different WPT classes, the efficiency might be sub-optimal, but in any case it must not drop below 75% [11, 16].

Table 2.3: WPT interoperability classes according to power levels, as defined by SAE J2954 [9, 11].

(GA)	(VA)			
	WPT1	WPT2	WPT3	WPT4
WPT1	Required	Required	Required	TBD
WPT2	Required	Required	Required	TBD
WPT3	Required	Required	Required	TBD
WPT4	TBD	TBD	TBD	Required

Also the distance between the primary coil and secondary coil is classified by SAE. The magnetic gap drops into three Z-classes, depicted in Tab. 2.4. Along with the Z-classes, the standard cites the misalignment distance in the three directions X , Y and Z and sets their limits, Tab. 2.5.

Table 2.4: WPT ground clearance range according to SAE J2954 [9, 11].

<i>Z-Class</i>	<i>Ground clearance range (mm)</i>
Z1	100-150
Z2	140-210
Z3	170-250

Table 2.5: WPT misalignment distance according to SAE J2954 [9, 11].

<i>Z-Class</i>	<i>Misalignment distance (mm)</i>
ΔX	± 75
ΔY	± 100
ΔZ	$Z_{nom} - \Delta_{low} > Z_{nom} + \Delta_{high}$
Rotation, roll and Yaw	Testing at $\pm 2,4,6$ degrees

The definition of coil ground distance, between primary coil and secondary coil is shown in Fig. 2.3. For residential houses the GA might be mounted as shown in the picture, while for public parking or roads the GA must be incorporated into the asphalt.

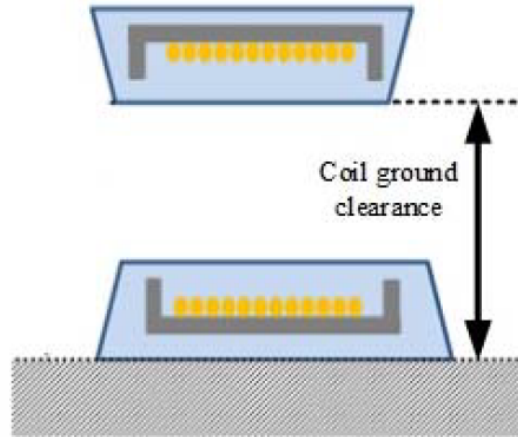


Figure 2.3: Definition of coil ground distance [9, 11].

With these premises, WPTBCs should be able to operate at the correct power rate at any relative position between GA and VA, within the above-mentioned range. In that range, the efficiency from the grid connection to the output of WPT charging system must be at least equal to target values. Fig. 2.4 illustrates the complete functional and physical system requirements to be compliant with requirements.

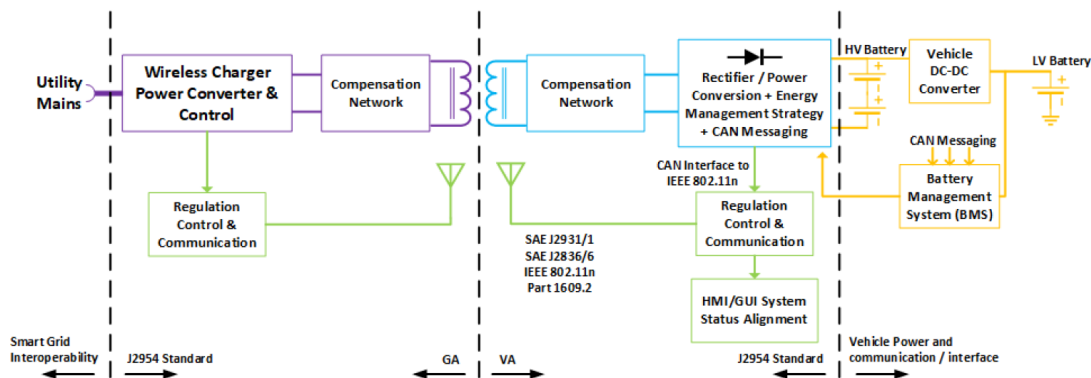


Figure 2.4: Typical functional elements of wireless charging system [11].

EMF Exposure

In order to preserve the human health, the Electro Magnetic Field (EMF) exposure must be defined and confined as close as possible to the transmitting and receiving pads. To do so, when the vehicle reaches the recharging point the standard SAE J2954 imposes two alignment methods [9, 11], [16]:

- The GA coil generates a small magnetic field, so that it can be detected by the VA coil. The main drawback is the operability range, which is limited to 1m.
- The magnetic field is not generated anymore by the GA coil, but in this case the magnetic signal is emitted from the VA through an auxiliary coil. As soon as the GA coil detects the signal, it responds to the VA via communication interface. The detection range is extended at about 5m.

Fig. 2.5 represents the above-mentioned alignment conditions.

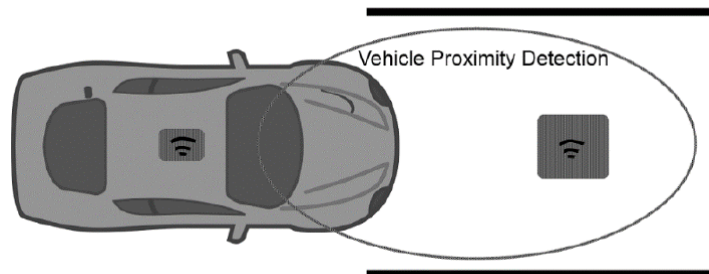


Figure 2.5: Vehicle proximity detection [9, 11].

In addition, to be compliant with ICNIRP2010 shown in Tab. 2.1 the standard imposes limited time-varying magnetic field, electric field and EMF [11, 12], [16]. On top of that, in the space regions 2a, 2b and 3 of Fig. 2.6 also contact currents must be compliant with ICNIRP2010. EMF exposure limits from CNIRP2010 are given in Tab. 2.6 [9].

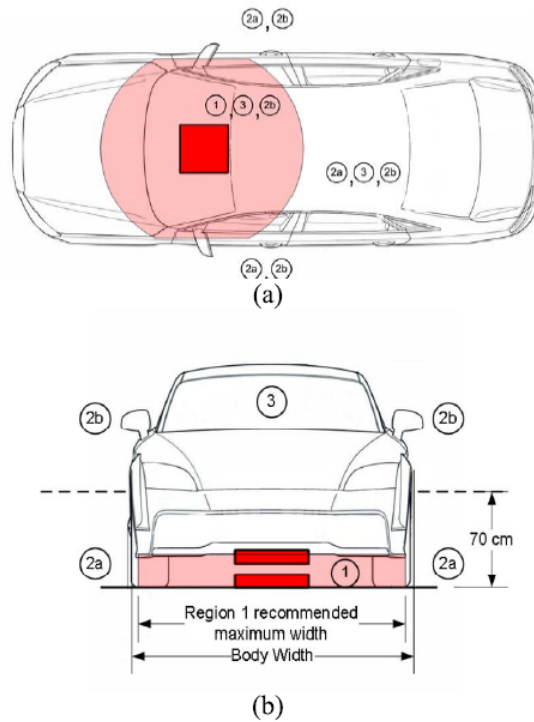


Figure 2.6: EMF and contact current limit region (a) top view and (b) front view [9, 11].

Table 2.6: Magnetic field, electric field and contact current exposure standard level [9, 11].

	<i>RMS</i>	<i>Peak</i>
Magnetic field	$27\mu\text{T}$ or 21.4A/m	$38.2\mu\text{T}$ or 30.4A/m
Electric field	83V/m	117V/m
Contact current	$0.2 \times f(\text{kHz}) = 17\text{mA}$ @85kHz	$0.283 \times f(\text{kHz}) = 24\text{mA}$ @85kHz

There might be additional aspects that deserve to be covered when designing WBT-BCs. Many of them are also discussed by SAE J2954 standard (i.e. coupling pad design, shielding, EMC compatibility, etc), but as mentioned at the beginning of the Chapter and based on this thesis focus, only the resonant tank compensation network and control techniques for primary inverter are analyzed in detail in the following.

Chapter 3

Resonant Tank Optimization

To increase system efficiency from a transmitting coil to a receiver coil through inductive power transfer, compensation capacitors must to be used. Starting from high level system requirements for WPTBCs, this Chapter allocates level requirements for optimal efficiency-based design of the resonant tank considering a single stage application, which avoids the DC/DC converter upstream the battery. The mathematical models of the most effective compensation networks, Series-Series (S-S) and Series-Parallel (S-P), are derived and fully analyzed for achieving CC-CV charging profile. Proceeding into the Chapter, a load definition along with a general resonant tank design procedure for providing compensation capacitor values along with primary self-inductance and secondary self-inductance is given. Finally, main characteristics of S-S and S-P networks are highlighted.

3.1 Resonant Tank System Requirements

In order to reduce system losses and to increase the system efficiency compensation capacitors, connected either in series, parallel or series-parallel combinations are adopted and connected both to primary side (GA) and secondary side (VA) of the resonant tank, as shown in Fig. 3.1.

Their need comes from low coupling between GA and VA, high leakage inductance and magnetizing inductance leading to high reactive current circulation [9], [17, 18]. Basically, compensation networks are in charge of providing the reactive

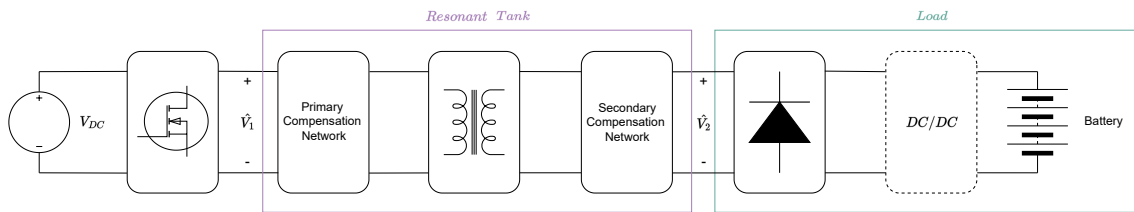


Figure 3.1: DC/DC power conversion stage for a WPT battery charger system. The dotted converter upstream the battery might be avoided if the system is properly designed.

power required to sustain the magnetic field [17, 19]. To design a compensation network properly there are system requirements to be met [9, 17]:

- **Maximize the power transfer:**
 primary compensation network is in charge of compensating the leakage inductance on the primary side, while secondary compensation network acts the same on the receiving coil [19, 20].
- **Minimize VA rating of power supply:**
 the VA coil is the first component, mounted on-board, which receives the power needed to recharge the battery. Lighter and smaller VAs benefit of weight and space reduction allowing to increase power density.
- **Constant voltage or constant current output, depending on the application:**
 compensation network may be not designed for battery charger application, but for general application. However, when working with lithium-ion batteries to preserve the health and extend the battery life they need to be charged according to a well defined current and voltage profile [17, 21].
- **High efficiency:**
 the higher the efficiency, the lower the Heat Ventilation and Air Conditioning (HVAC) system, and the faster is the recharging.
- **Bifurcation tolerant:**
 one of the biggest issue of WPT system is bifurcation. It consists of not having a monotonic behavior above and below resonance on current gain and voltage

gain, while for the compensation network impedance it results in multiple zero phase angle. The main cause is strongly dependent on the load seen at the output terminals of GA [9, 22].

- High misalignment tolerant:

analogous reasoning to the bifurcation can be carried out for misalignment, which leads to a coupling coefficient change resulting in different voltage gain and current gain shapes.

Several compensation networks have been studied and analyzed in literature over the years [17, 18, 19, 20, 21, 23, 24, 25, 26, 27, 28], but for industrial applications where complexity, size and costs matter the basic compensation networks such as Series-Series (S-S), Series-Parallel (S-P) and Series-Parallel combination (LCC-S, LCC-LCC), result to be the preferred ones. Therefore, they are widely discussed hereinafter.

Although the general trend when design WPT applications is to tune only primary and secondary compensation capacitors C_1 and C_2 since primary and secondary self-inductances L_1 and L_2 are usually supposed to be know. However, following this approach their value is not optimized for the specific application. This is the reason why in the following L_1 , L_2 , C_1 and C_2 are optimized all together according to a maximum efficiency approach.

3.2 Mathematical Description

3.2.1 Matching Coils

Before proofing the mathematical model of S-S and S-P compensation network, it is necessary to describe the equations of matching coils. In literature, several equivalent representations of matching coils are available. Therefore, to avoid any misunderstanding and to associate different nomenclatures to physical quantities, the main models are described below. Fig. 3.2a shows the transformer equivalent representations of matching coils based on system parameters, where L_1 is the primary

self-inductance and L_2 the secondary self-inductance. M is the mutual inductance between primary and secondary coil defined as:

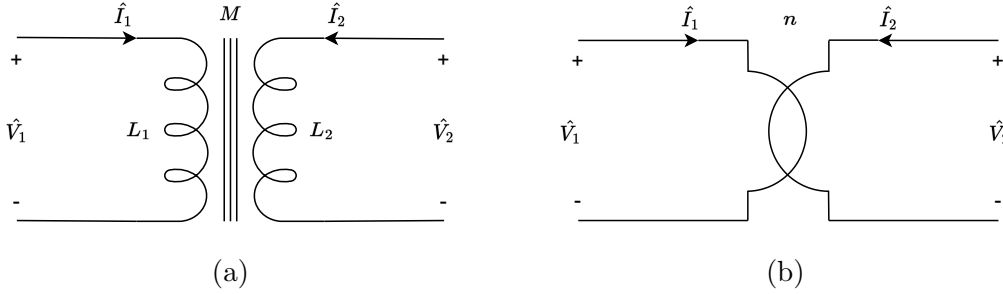


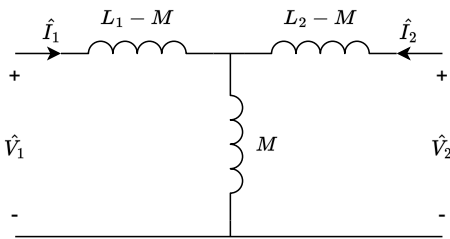
Figure 3.2: Transformer representation of WPT matching coils for (a) electrical circuitry based on self-inductances and mutual inductance, while (b) avoiding the use of system parameters and defining the voltage ration n .

$$M = \frac{k}{\sqrt{L_1 L_2}} \quad (3.1)$$

where $k \in [0,1]$ is the coupling coefficient between transmitting and receiving coils. The equivalent electric circuitry, drawn considering the turn ratio n is illustrated in Fig. 3.2b. In both figures, \hat{V}_1 is the phasor of the primary voltage applied to the tank, which corresponds to the middle point outputs of the inverter legs, while \hat{V}_2 is the phasor of the secondary voltage applied to the full-bridge rectifier.

$$\begin{cases} \hat{V}_1 = n\hat{V}_2 \\ n = \frac{N_1}{N_2} \end{cases} \quad (3.2)$$

Replacing the transformer with the T equivalent circuit model of Fig. 3.3, the system parameters of Tab. 3.1 are the same of Fig. 3.2a.



Parameter	Unit of measure
L_1	H
L_2	H
M	H

Figure 3.3: T model representation of WPT matching coils.

Table 3.1: T model matching coils system parameters.

Introducing the primary leakage inductance L_{lk1} , the secondary leakage inductance L_{lk2} and the magnetizing inductance L'_μ to the transformer representation, the equivalent circuit of Fig. 3.4, with its parameters depicted in Tab. 3.2, is obtained.

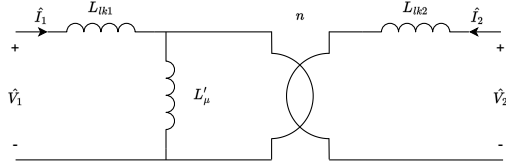


Figure 3.4: T model representation with leakage inductances.

Parameter	Unit of measure
L_{lk1}	H
L_{lk2}	H
L'_μ	H
n	-

Table 3.2: System parameters of Fig. 3.4.

The secondary leakage inductance L_{lk2} can be transferred to the primary side considering the turn ratio n . According to parameters L'_{lk1} and L'_{lk2} referred to primary side, both the transformer model and the T model can be updated, as shown in Fig. 3.5a and Fig. 3.5b, respectively. The corresponding values are listed in Eq. 3.3.

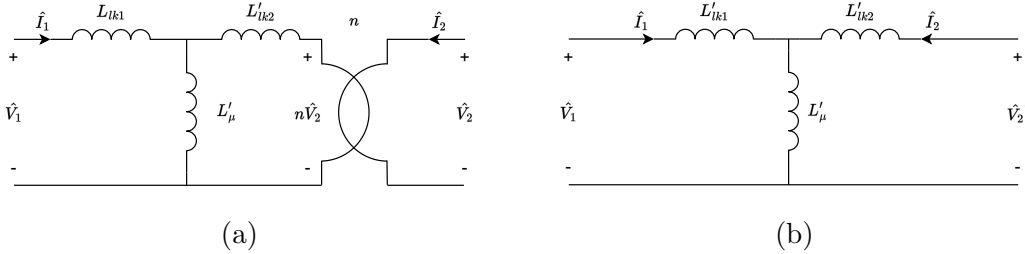


Figure 3.5: Updating of (a) transformer model and (b) T model according to leakage inductances for WPT resonant tank.

$$\begin{cases} L'_{lk1} = L_{lk1} \\ L'_{lk2} = n^2 L_{lk2} \\ L'_\mu = L'_\mu \\ \hat{V}'_2 = n \hat{V}_2 \end{cases} \quad (3.3)$$

With reference to Fig. 3.5b and Fig. 3.3, the system of Eq. 3.4 links the leakage in-

ductances to the self-inductance of primary and secondary side and the magnetizing inductance with the mutual inductance, by means of a turn ration.

$$\begin{cases} L_{lk1} = L_1 - nM \\ L_{lk2} = L_2 - \frac{M}{n} \\ L'_\mu = nM \end{cases} \Leftrightarrow \begin{cases} L_1 = L_{lk1} + nM \\ L_2 = L_{lk2} + \frac{M}{n} \\ L'_\mu = nM \end{cases} \Leftrightarrow \begin{cases} L_1 = L_{lk1} + \frac{L'_\mu}{n} \\ L_2 = L_{lk2} + \frac{L'_\mu}{n^2} \\ L'_\mu = nM \end{cases} \quad (3.4)$$

Considering the circuit as shown in Fig. 3.3, the Kirchoff's Voltage Law of primary and secondary side are:

$$\begin{cases} \hat{V}_1 = j\omega L_1 \hat{I}_1 + j\omega M \hat{I}_2 \\ \hat{V}_2 = j\omega L_2 \hat{I}_2 + j\omega M \hat{I}_1 \end{cases} \quad (3.5)$$

where $\omega = 2\pi f$ is the angular frequency, f is the frequency and \hat{I}_1 , \hat{I}_2 are the phasors of primary and secondary current, respectively. From Eq. 3.5 the phasor of the primary current can be calculated as:

$$\begin{aligned} \hat{I}_1 &= \frac{\hat{V}_1}{j\omega L_1} - \frac{j\omega M}{j\omega L_1} \hat{I}_2 \\ &= \frac{\hat{V}_1}{j\omega L_1} - \frac{M}{L_1} \hat{I}_2. \end{aligned} \quad (3.6)$$

Substituting Eq. 3.6 into Eq. 3.5b the phasor of the secondary voltage results:

$$\begin{aligned} \hat{V}_2 &= j\omega L_2 \hat{I}_2 + \frac{j\omega M}{j\omega L_1} \hat{V}_1 - \frac{j\omega M^2}{L_1} \hat{I}_2 \\ &= j\omega L_2 \left(1 - \frac{M^2}{L_1 L_2}\right) \hat{I}_2 + \frac{j\omega M}{j\omega L_1} \hat{V}_1 \\ &= j\omega L_2 \left(1 - \frac{M^2}{L_1 L_2}\right) \hat{I}_2 + \frac{M}{L_1} \hat{V}_1 \end{aligned} \quad (3.7)$$

introducing the equation of a generic load impedance \hat{Z}_{ac} , the phasor of the secondary current can be expressed as:

$$\hat{I}_2 = -\frac{\hat{V}_2}{\hat{Z}_{ac}}. \quad (3.8)$$

Finally, substituting Eq. 3.8 into Eq. 3.7 the compensation network voltage gain, defined as the ratio between the phasor of secondary voltage and the phasor of primary voltage becomes:

$$\begin{aligned}
 \hat{V}_2 &= -j\omega L_2 \left(1 - \frac{M^2}{L_1 L_2}\right) \frac{\hat{V}_2}{\hat{Z}_{ac}} + \frac{M}{L_1} \hat{V}_1 \\
 \Rightarrow \hat{V}_2 \left[1 + \frac{j\omega L_2}{\hat{Z}_{ac}} \left(1 - \frac{M^2}{L_1 L_2}\right)\right] &= \frac{M}{L_1} \hat{V}_1 \\
 \Rightarrow \hat{G}_v = \frac{\hat{V}_2}{\hat{V}_1} &= \frac{M}{L_1} \frac{1}{\left[1 + \frac{j\omega L_2}{\hat{Z}_{ac}} \left(1 - \frac{M^2}{L_1 L_2}\right)\right]}.
 \end{aligned} \tag{3.9}$$

The second significant parameter for achieving CC-CV profiles during charging cycles is obtained comparing the secondary current with the primary voltage. The transconductance for matching coils is obtained explicating the primary current from Eq. 3.5b as:

$$\begin{aligned}
 \hat{I}_1 &= \frac{\hat{V}_2}{j\omega M} - \frac{j\omega L_2}{j\omega M} \hat{I}_2 \\
 &= \frac{\hat{V}_1}{j\omega L_1} - \frac{M}{L_1} \hat{I}_2
 \end{aligned} \tag{3.10}$$

and inserting it inside Eq. 3.5a, resulting:

$$\begin{aligned}
 \hat{V}_1 &= j\omega L_1 \left(\frac{\hat{V}_2}{j\omega M} - \frac{L_2}{M} \hat{I}_2\right) + j\omega M \hat{I}_2 \\
 &= \frac{L_1}{M} \hat{V}_2 - \frac{j\omega L_1 L_2}{M} \hat{I}_2 + j\omega M \hat{I}_2 \\
 &= \frac{L_1}{M} \hat{V}_2 + \frac{j\omega M^2 - j\omega L_1 L_2}{M} \hat{I}_2
 \end{aligned} \tag{3.11}$$

The phasor of secondary voltage can be deduced from Eq. 3.8 as $\hat{V}_2 = -\hat{Z}_{ac} \hat{I}_2$. Inserting it into Eq. 3.11 the phasor of the transconductance results to be:

$$\begin{aligned}
 \hat{V}_1 &= -\frac{L_1}{M} \hat{Z}_{ac} \hat{I}_2 + \frac{j\omega M^2 - j\omega L_1 L_2}{M} \hat{I}_2 \\
 &= \frac{-L_1 \hat{Z}_{ac} + j\omega(M^2 - L_1 L_2)}{M} \hat{I}_2 \\
 \Rightarrow \hat{G}_{tr} = \frac{\hat{I}_2}{\hat{V}_1} &= \frac{M}{-L_1 \hat{Z}_{ac} + j\omega(M^2 - L_1 L_2)}.
 \end{aligned} \tag{3.12}$$

3.2.2 Resonant Tank

The same calculation procedure carried out for matching coils in Subsection 3.2.1 can be performed when integrating the primary compensation capacitor C_1 along with

lumped equivalent series resistances R_1 and R_2 , which model the coil losses. The secondary compensation topology, with the compensation capacitor C_2 , is included into the load description represented by generic impedance load \hat{Z}_{ac} .

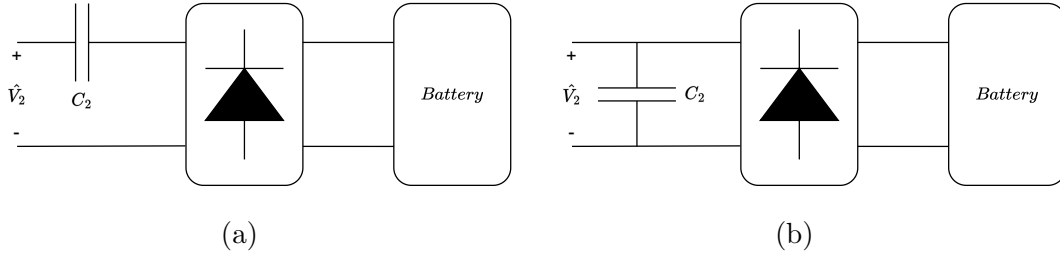


Figure 3.6: Equivalent load impedance seen at the output terminals of the resonant tank for a) series compensation and b) parallel compensation.

In case of secondary series compensation as for Fig. 3.6a, the phasor of the secondary current \hat{I}_2 can be supposed sinusoidal, whereas even if the phasor of the secondary voltage \hat{V}_2 might be slightly distorted it can be approximated as a square wave. In first harmonic approximation, these assumptions return the equivalent load impedance as [29]:

$$\hat{Z}_{ac} = \frac{8}{\pi^2} R_{load} \quad (3.13)$$

Indeed, in case of secondary parallel compensation, as for Fig. 3.6b, the secondary voltage is supposed to be sinusoidal and the situation is reversed, leading to an equivalent load resistance defined as [29]:

$$\hat{Z}_{ac} = \frac{\pi^2}{8} R_{load} \quad (3.14)$$

In both cases, the load resistance is calculated from the voltage imposed by the battery V_{batt} and the power generated or absorbed by the battery P_{batt} and it is equal to:

$$R_{load} = \frac{V_{batt}^2}{P_{batt}}. \quad (3.15)$$

The resulting system is shown in Fig. 3.7.

With reference to Fig. 3.7, the Kirchhoff's Voltage Law of primary and secondary side can be written as:

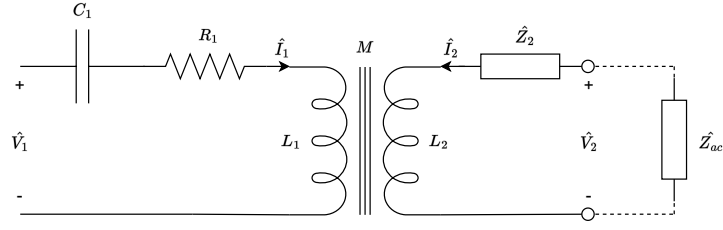


Figure 3.7: Integration of both primary compensation capacitor and equivalent impedance load into a matching coils network.

$$\begin{cases} \hat{V}_1 = \left[R_1 + j \left(\omega L_1 - \frac{1}{\omega C_1} \right) \right] \hat{I}_1 + j\omega M \hat{I}_2 \\ \hat{V}_2 = \hat{Z}_2 \hat{I}_2 + j\omega M \hat{I}_1. \end{cases} \quad (3.16)$$

where for S-S compensation

$$\begin{aligned} \hat{Z}_2 &= R_2 + j \left(\omega L_2 - \frac{1}{\omega C_2} \right) \\ \hat{Z}_{ac} &= \frac{8}{\pi^2} R_{load} \end{aligned} \quad (3.17)$$

and for S-P compensation

$$\begin{aligned} \hat{Z}_2 &= R_2 + j\omega L_2, \\ \hat{Z}_{ac} &= \frac{\pi^2}{8} R_{load} // \frac{1}{j\omega C_2} \end{aligned} \quad (3.18)$$

Defining the phasor of the primary impedance as:

$$\hat{Z}_1 = R_1 + j \left(\omega L_1 - \frac{1}{\omega C_1} \right) \quad (3.19)$$

the phasor of the primary current can be calculated from Eq. 3.16a as:

$$\hat{I}_1 = \frac{\hat{V}_1}{\hat{Z}_1} - \frac{j\omega M}{\hat{Z}_1} \hat{I}_2 \quad (3.20)$$

substituting Eq. 3.20 into Eq. 3.16b the phasor of the secondary voltage can be rewritten as:

$$\begin{aligned} \hat{V}_2 &= \hat{Z}_2 \hat{I}_2 + \frac{j\omega M}{\hat{Z}_1} \hat{V}_1 + \frac{(\omega M)^2}{\hat{Z}_1} \hat{I}_2 \\ &= \left(\hat{Z}_2 + \frac{(\omega M)^2}{\hat{Z}_1} \right) \hat{I}_2 + \frac{j\omega M}{\hat{Z}_1} \hat{V}_1. \end{aligned} \quad (3.21)$$

Integrating the phasor of a generic load impedance as Eq. 3.8, the voltage gain of the resonant tank becomes:

$$\begin{aligned}
 \hat{V}_2 &= -\left(\hat{Z}_2 + \frac{(\omega M)^2}{\hat{Z}_1}\right) \frac{\hat{V}_2}{\hat{Z}_{ac}} + \frac{j\omega M}{\hat{Z}_1} \hat{V}_1 \\
 \Rightarrow \hat{G}_v &= \frac{\hat{V}_2}{\hat{V}_1} = \frac{j\omega M}{\hat{Z}_1} \frac{1}{\left[1 + \frac{\hat{Z}_1 \hat{Z}_2 + (\omega M)^2}{\hat{Z}_1 \hat{Z}_{ac}}\right]}.
 \end{aligned} \tag{3.22}$$

Similarly to the matching coils, for primary series compensation, the transconductance gain can be calculated substituting the secondary voltage obtained from the load equation in Eq. 3.8. Inserting the secondary voltage into Eq. 3.16b, the primary current results:

$$\hat{I}_1 = -\frac{(\hat{Z}_2 + \hat{Z}_{ac})}{j\omega M} \hat{I}_2. \tag{3.23}$$

Inserting Eq. 3.23 into Eq. 3.16a the primary voltage results:

$$\begin{aligned}
 \hat{V}_1 &= \hat{Z}_1 \hat{I}_1 + j\omega M \hat{I}_2 \\
 &= -\frac{\hat{Z}_1(\hat{Z}_2 + \hat{Z}_{ac})}{j\omega M} \hat{I}_2 + j\omega M \hat{I}_2 \\
 &= -\left[\frac{\hat{Z}_1(\hat{Z}_2 + \hat{Z}_{ac}) + (\omega M)^2}{j\omega M}\right] \hat{I}_2
 \end{aligned} \tag{3.24}$$

the transconductance gain is simply obtained:

$$\hat{G}_{tr} = \frac{\hat{I}_2}{\hat{V}_1} = -\left[\frac{j\omega M}{\hat{Z}_1(\hat{Z}_2 + \hat{Z}_{ac}) + (\omega M)^2}\right]. \tag{3.25}$$

3.2.3 Generalized Approach for Efficiency Calculation

Reference [30] reports an efficiency calculation based on a generalized approach, valid for all the compensation topologies, including both S-S and S-P compensation. In a general form, specific for a resonant tank WPT system, Fig. 3.8 includes all the stages starting from the middle point outputs of the inverter legs up to the load. The primary voltage, at resonance, is supposed to be sinusoidal.

In the most general way, independently from primary and secondary compensation networks, the total efficiency η_{tot} can be obtained as the product of the efficiency of each stage:

$$\eta_{tot} = \eta_{pc} \eta_p \eta_s \eta_{sc} \tag{3.26}$$

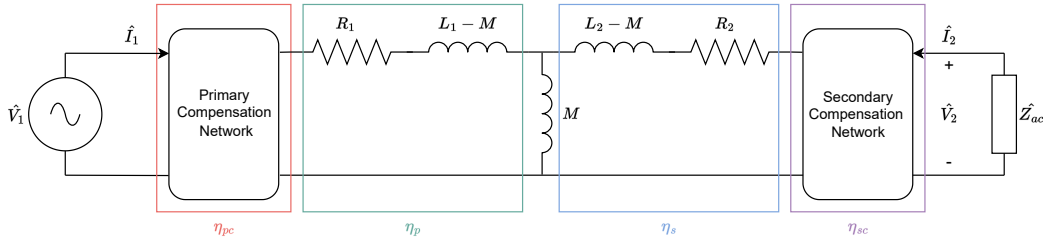


Figure 3.8: Resonant tank efficiency stages. Matching coils are represented by a transformer T model.

where η_{pc} is the primary compensation network efficiency, η_p and η_s are the primary side and secondary side efficiency and η_{sc} the secondary compensation network efficiency. The whole resonant tank efficiency, which includes all the stages of Fig. 3.8, can be expressed as [31]:

$$\begin{aligned}
 \eta_{tot} &= \frac{P_2}{P_1} \\
 &= \frac{\hat{Z}_{ac} |\hat{I}_2|^2}{\hat{V}_1 \text{Re}[\hat{I}_1]} \\
 &= \frac{\hat{Z}_{ac} (\omega M)^2}{|(\hat{Z}_{ac} + \hat{Z}_2) \hat{Z}_1 + (\omega M)^2|^2} \\
 &= \text{Re} \left[\frac{\hat{Z}_2 + \hat{Z}_{ac}}{(\hat{Z}_{ac} + \hat{Z}_2) \hat{Z}_1 + (\omega M)^2} \right]
 \end{aligned} \tag{3.27}$$

where the real powers P_1 and P_2 are the input power and output power of the resonant tank. Primary impedance \hat{Z}_1 , secondary impedance \hat{Z}_2 and the equivalent load impedance depend on the configuration topology, as illustrated in Fig. 3.9, that shows the equivalent circuit including impedances.

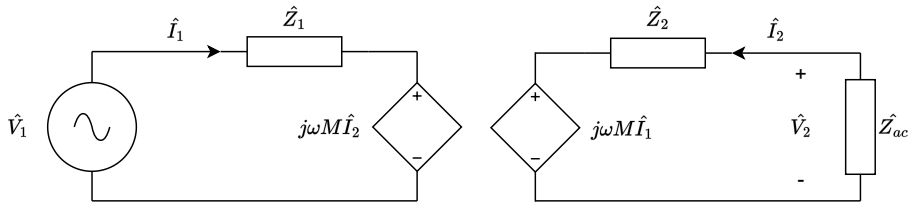


Figure 3.9: Simplified high frequency WPT circuit for generalized efficiency calculation.

3.2.4 Load Modelling

The modern trend in electric mobility, for both BEV and PHEV, clearly shows a transition in the traction battery rated voltage, passing from low voltage to high voltage battery packs, up to 400V or 800V, especially for those powertrain architectures applicable to high performance cars. In this frame, battery packs are equipped with either high power or high density cylindrical cells. When the target performance is related to the maximum available power, the cell chemistry usually mounted is Nickel Manganese and Cobalt (NMC), while for maximizing energy density, and consequently to reduce range anxiety, Lithium Iron Phosphate (LiFePo₄) cells are usually adopted. In both cases the cell range is usually fully managed.

For PHEVs, the trend behaves according to BEV, reaching the same voltage levels of BEVs. PHEV battery packs differ from BEVs for the capacity of the battery pack, which is drastically reduced since it works coordinated with a fuel-based engine to power the car. Considering the widely spread 21700 cylindrical cell format with nominal voltage equal to 3.6V, the cell is exploited from a minimum voltage equal to 2.9V up to a maximum voltage equal to 4.2V. Then, considering a 100S or 200S series connected cells for 400V and 800V architectures, the battery pack voltage ranges from 290V to 420V and from 580V to 840V, respectively. Tab. 3.3 illustrates the configuration of both BEV and PHEV battery pack topologies, for 400V rated voltage and considering the Lithium-ion cell "Molicel INR-21700-P42B" [32].

Table 3.3: Battery pack parameters for BEVs and PHEVs, considering the cell "Molicel INR-21700-P42B".

<i>Quantity</i>	<i>Symbol</i>	<i>Value</i>		<i>Unit of Measure</i>
		<i>BEV</i>	<i>PHEV</i>	
Series cells	N_s	100	100	-
Parallel cells	N_p	48	5	-
Cell rated voltage	$V_{c,rated}$	3.6	3.6	V
Cell minimum voltage	$V_{c,min}$	2.9	2.9	V
Cell maximum voltage	$V_{c,max}$	4.2	4.2	V
Cell rated capacity	$C_{c,rated}$	4.2	4.2	Ah
Battery minimum voltage	$V_{batt,min}$	290	290	V
Battery maximum voltage	$V_{batt,max}$	420	420	V

Although a lithium-ion cell can be represented by several chemical [33, 34], electrical [35] or electro-chemical [36] models, in order to recharge correctly lithium-ion cells, a well defined CC-CV charging cycle must be ensured. Considering a maximum charging power according to SAE J2954 WPT1, equal to 3.7 kW and a battery pack rated voltage equal to 400V, the resulting CC-CV obtained from experimental tests of "Molicel INR-21700-P42B cell" is reported in Fig. 3.10. The CC constant current I_{cc} is obtained as:

$$I_{cc} = \frac{P_{max}}{V_{batt,max}} \quad (3.28)$$

and the time is normalized with respect to the end-of-charge time.

As previously mentioned in Subsection 3.2.3, in order to find the equivalent load resistance at the output terminals of the secondary resonant tank, in the hypothesis of ideal components, a lithium-ion cell can be modelled under the assumption of first harmonic approximation [29], returning the equivalent load resistance value as:

$$R_{ac} = \frac{\pi^2}{8} R_{batt} \quad \text{for SP Compensation} \quad (3.29)$$

$$R_{ac} = \frac{8}{\pi^2} R_{batt} \quad \text{for SS Compensation} \quad (3.30)$$

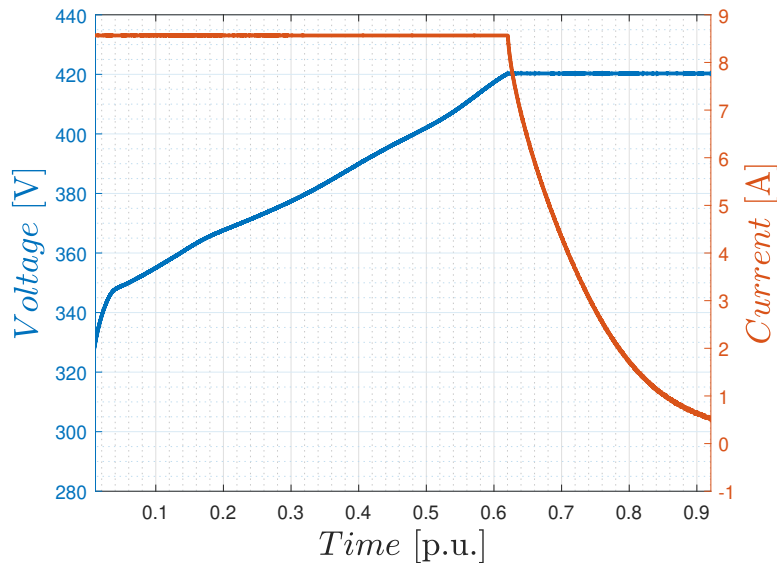


Figure 3.10: Experimental data from CC-CV charging cycle of Molicec INR-21700-P42B cell for a 100S battery pack configuration and SAE J2954 WPT1. The time is normalized with respect to the end-of-charge time.

where the equivalent resistance of the battery is calculated as

$$R_{batt} = \frac{V_{batt}^2}{P_{batt}} \quad (3.31)$$

where V_{batt} is the actual voltage at the battery terminals and P_{batt} is the power delivered or absorbed by the battery.

The equivalent battery load resistance R_{ac} consists of a full-bridge diode rectifier, which might be followed by a first or second order filter, which feeds, in a single stage configuration that avoids the use of the DC/DC converter, the battery.

For a full battery voltage range, the equivalent battery resistance behaves linearly in the CC region, while in the CV region it takes the shape of the decreasing current, which might be approximated by an exponential behavior. Fig. 3.11a represents, in the whole CC-CV charging cycle, the battery resistance and, according to Eq. 3.29 and Eq. 3.30 the equivalent R_{ac} resistance for S-P compensation and S-S compensation. The resistance trend is given along with the power, to clearly associate the plot with data obtained with the experimental CC-CV charging cycle. Indeed, Fig. 3.11b zooms the right axis to provide a visible scale of the resistance in the CC region.

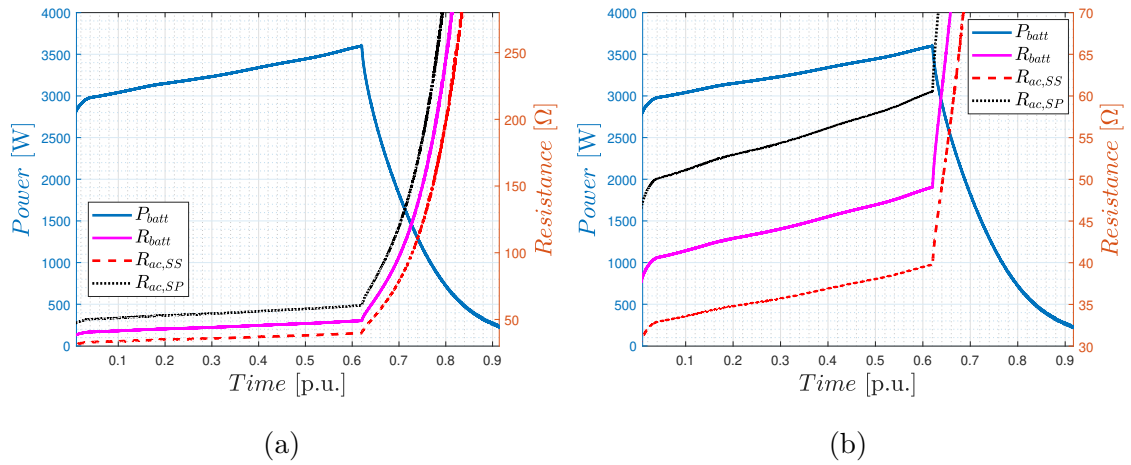


Figure 3.11: Battery power and load resistance variation for (a) complete CC-CV charging cycle and (b) with zoomed scale for the CC region. The time is normalized with respect to the end-of-charge time.

Tab. 3.4 summarizes the most significant resistance values, for both BEVs and PHEVs in a complete charging cycle for WPT1 class.

Table 3.4: Representative resistance values in a complete CC-CV charging cycle for WPT1 class, adopting a 100S battery pack configuration for BEVs and PHEVs.

	<i>Quantity</i>	$R_{batt}[\Omega]$	$R_{ac,SS}[\Omega]$	$R_{ac,SP}[\Omega]$
<i>CC</i>	Minimum resistance	35	28	44
	Maximum resistance	49	40	60
	Load variation	14	12	16
<i>CV</i>	Minimum resistance	49	40	60
	Maximum resistance	247*	200*	293*
	Load variation	98	160	233
<i>CC-CV</i>	Minimum resistance	35	28	44
	Maximum resistance	247*	200*	293*
	Load variation	212	172	249

*Values referred to Time = 0.8 [p.u.]

What is noticeable from Tab. 3.4 are the load variations. In fact, taking as a benchmark the battery load variation, the S-S compensation exhibit a 19% less, while the S-P compensation 18% more.

3.3 Design Methodology

The main target of this subsection is to define a design procedure in order to find the optimal value of the primary and secondary self-inductances L_1 and L_2 , along with their respectively primary and secondary compensation capacitors C_1 and C_2 . A contactless EV battery charging system is designed to deliver 3.7 kW peak power at a nominal frequency of 85 kHz, according to SAE J2954 WPT1 class. Here, the difference with respect to many design procedures presented in literature is based on the fact that primary and secondary coils are not supposed to be identical, by they are optimized depending on the desired system characteristics. Once an EV has stopped over the charging system, power is transferred across the air gap via magnetic coupling between the primary coil, which might be under the ground or above the ground and the secondary coil beneath the EV. Depending on the Z axes distance and on the misalignment the coupling coefficient k might vary [37]. For this analysis, it is supposed to vary in between 0.1 and 0.25. Hereinafter, a design procedure for both S-S compensation and S-P compensation is given, since the current-source characteristic of S-S compensation is suitable for constant current charging and the voltage source characteristic of S-P compensation is suitable for constant voltage charging.

Even if basic resonant topologies have been deeply studied and compared in [38], parallel-series (PS) and parallel-parallel (PP) are not of interest for battery charging applications, since the voltage applied to the tank is imposed by the inverter and an additional inductor must be connected in series between the inverter output port and the resonant tank [39], whose value may not be negligible. When it comes to S-S topology, references [40, 41] present a relatively simple design, but with some difficulties in following the CC-CV charging cycle together with achieving zero-phase angle (ZPA). S-S and S-P compensations are only capable to operate either in CC

mode with ZPA or CV mode with ZPA, but they are not allowed to achieve both requirements at the same time [39]. Although [42] proposes a frequency control, which complies with SAE J2954, for battery charging applications S-P compensated, it does not guarantee ZPA. However, it can be therefore achieved by means of hybrid compensations, as demonstrated by [43]. By increasing the number of components, with a double side inductor-capacitor-capacitor (LCC-LCC) it is possible to fulfill both the CC-CV reference profiles and the ZPA condition. On the other hand, it requires many components, leading to an increase in size, power losses and control system complexity. In addition, the latter mentioned method becomes meaningless when the self-inductance of the primary side differs from the secondary one [39], which is a significant drawback when optimizing electrical components mounted on-board. Also, multiple-input-multiple-output (MIMO) configuration can be adopted in automotive applications. Reference [44] proposes a general design procedure, valid for any strictly-passive multi-port network, based on optimal impedance terminations for efficiency maximization. The efficiency can also be maximized for resonance frequency mismatch [45] or estimated using numerical and circuit models [46]. Multi-coil systems have been also proposed in [47, 48] to extend the transmission region and thus overcome the problem of the misalignment between the GA and VA coils, which can lead to severe components stress and disturbances [49, 50], besides hazard magnetic fields [51, 52]. However, when referring to automotive apparatuses, size and weight of the components are fundamental parameters that have to be minimized. This part aims to provide a general design procedure, including the coil design, based on maximizing the tank efficiency and minimizing the VA self-inductance, considering and comparing both the S-S and S-P compensation network topology for automotive battery charging applications. Starting from the design specification detailed in Tab. 3.5, the proposed design procedure for the EV battery charging application can be outlined in eight main steps as follows [22]. The first three steps are conceptually equal for both topologies, valid for both compensation topologies, whereas from step four to step eight, they are specific.

Table 3.5: System specifications for the resonant tank design.

<i>Quantity</i>	<i>Symbol</i>	<i>Value</i>	<i>Unit of Measure</i>
DC bus rated voltage	V_{dc}	400	V
Primary voltage	V_1	$\frac{4}{\pi}400$	V
Battery voltage range	V_{batt}	290-420	V
Battery power range*	P_{batt}	1-3.7	kW
Resonant frequency*	f_0	85	kHz
Frequency range*	Δf	79-90	kHz
Magnetic coupling range	k	0.1-0.25	-
Battery voltage range	V_{batt}	290-420	V
Primary inductor quality factor	Q_1	$\gg 100$	-
Secondary inductor quality factor	Q_2	$\gg 100$	-

*According to SAE J2954

From system requirements cited in Subsection 3.1, it is possible to derive the target performance of the resonant tank, which are classified according to level requirements:

- Maximize the resonant efficiency
- Lightweight VA
- Fulfil the battery voltage range
- Follow the CC-CV charging cycle
- ZVS in primary inverter by design

3.3.1 Series-Parallel (S-P)

Starting from the efficiency maximization and according to Eq. 3.27, and defining $P_{batt} = \frac{|\hat{V}_2|^2}{R_{ac}}$, the resonant tank efficiency can be expressed as:

$$\eta_{T_{link}} = \frac{P_2}{P_1} = \frac{\frac{|\hat{V}_2|^2}{R_{ac}}}{\operatorname{Re} \left[\hat{V}_{L1} \hat{I}_{L1}^* \right]} \quad (3.32)$$

where \hat{V}_{L1} and \hat{I}_{L1}^* are the voltage and the current conjugated on the primary coil L_1 . It must be pointed out that the efficiency expressed in this way does not consider the primary capacitor, since the input power is calculated directly on the primary coil, which is downstream the primary compensation network. It is therefore independent from primary compensation. Manipulating the equation as stated in [22, 53], the resonant tank efficiency can be rearranged as:

$$\eta_{T_{link}} = \frac{k^2 Q_1 Q_2^2}{(\alpha + Q_2) \left(1 + k^2 Q_1 Q_2 + \frac{Q_2}{\alpha} \right)} \quad (3.33)$$

where $\alpha = \omega C_2 R_{ac}$ and $\omega = 2\pi f$ is the operating angular frequency associated to the operating frequency f , while the primary inductor quality factor is defined as $Q_1 = \frac{\omega L_1}{R_1}$. For a given coupling coefficient k and operating frequency f this formula has been rearranged in order so as not to depend on the primary compensation topology. However, the information related to the secondary compensation is contained into α . In addition to the equivalent resistance information, α also contains the optimum value of the secondary capacitance, which can be extrapolated enforcing:

$$\frac{\partial \eta_{T_{link}}}{\partial \alpha} = 0 \quad (3.34)$$

which returns the optimum α value at the reference coupling coefficient k_0 :

$$\alpha_{opt} = \frac{Q_2}{\sqrt{1 + k_0^2 Q_1 Q_2}}. \quad (3.35)$$

Then, considering the reference operating frequency f_0 and the reference equivalent load $R_{ac,0}$, the optimized value of the secondary compensation capacitor results:

$$C_{2_{opt}} = \frac{\alpha_{opt}}{\omega_0 R_{ac,0}}. \quad (3.36)$$

At this point, the algorithm presents two choices when working at reference ω_0 and k_0 : constant voltage output or constant ZPA. Since to achieve ZVS in the primary inverter the input impedance of the resonant tank must be inductive, which

means the the phase angle must be greater than zero, the constant voltage output is chosen. Imposing the resonant frequency of primary compensation and secondary compensation equal to the reference design frequency, it leads:

$$\omega_1 = \omega_2 = \omega_0 \quad (3.37)$$

where:

$$\omega_1 = \frac{1}{\sqrt{L_1 C_1 (1 - k_0^2)}} \quad \text{and} \quad \omega_2 = \frac{1}{\sqrt{L_2 C_2}}. \quad (3.38)$$

From Eq. 3.37 and Eq. 3.38, inserting the optimum value of C_{2opt} into those equations the optimum value of L_2 can be obtained:

$$\begin{aligned} L_{2opt} &= \frac{1}{\omega_0^2 C_{2opt}} \\ &= \frac{R_{ac,0}}{\alpha_{opt} \omega_0}. \end{aligned} \quad (3.39)$$

At this point, the value of the optimum secondary compensation capacitor and secondary self-inductance are found. As it is well known in literature [54] the S-P compensation presents constant voltage at resonant frequency and coupling coefficient. Therefore, knowing the battery voltage range and the DC bus rated voltage, passing from the voltage gain it is possible to obtain the optimum primary self-inductance value. Rewriting the voltage gain of Eq. 3.22 as:

$$|\hat{G}_v| = \sqrt{\frac{L_2}{L_1}} \left(\frac{k_0 Q_1 Q_2 \sqrt{\alpha^2 + 1}}{\alpha k_0^2 Q_1 Q_2 + \alpha + Q_2} \right). \quad (3.40)$$

The primary self-inductance optimum value can be obtained:

$$L_{1opt} = L_{2opt} \left(\frac{1}{|\hat{G}_v|} \frac{k_0 Q_1 Q_2 \sqrt{\alpha^2 + 1}}{\alpha k_0^2 Q_1 Q_2 + \alpha + Q_2} \right)^2 \quad (3.41)$$

imposing $\alpha = \alpha_{opt}$ it holds:

$$L_{1opt} = L_{2opt} \left(\frac{1}{|\hat{G}_v|} \frac{k_0 Q_1 Q_2 \sqrt{\alpha_{opt}^2 + 1}}{\alpha_{opt} k_0^2 Q_1 Q_2 + \alpha_{opt} + Q_2} \right)^2. \quad (3.42)$$

From Eq. 3.38 the optimized primary compensation capacitor results:

$$C_{1opt} = \frac{1}{\omega_0^2 L_{1opt} (1 - k_0^2)}. \quad (3.43)$$

The design procedure above-described is summarized in the flowchart of Fig. 3.12 and the resulting system parameters, for S-P compensation, are summarized in Tab. 3.6.

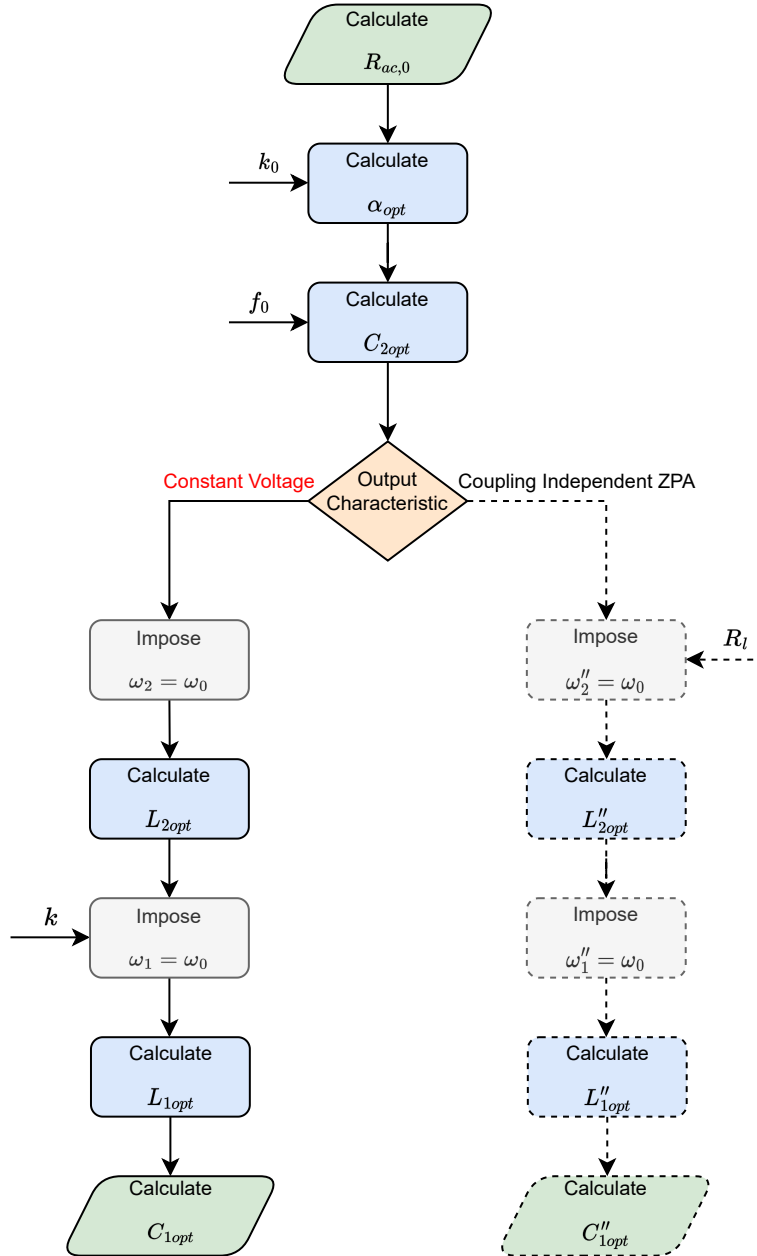


Figure 3.12: Flowchart for S-P compensation illustrating the design procedure for constant output voltage. The load resistance R_l and the coupling coefficient k refer to actual parameters during variable operating conditions.

Table 3.6: System parameters, for S-P compensation, obtained from the optimum design procedure.

<i>Quantity</i>	<i>Symbol</i>	<i>Value</i>	<i>Unit of Measure</i>
Primary self-inductance	L_1	3.4	mH
Secondary self-inductance	L_2	73.5	μ H
Primary compensation capacitor	C_1	1.12	nF
Secondary self-inductance	C_2	50.5	nF
Reference maximum voltage gain	$G_{v,max,0}$	1.2	-
Reference resonant frequency	f_0	82	kHz
Reference coupling coefficient	k_0	0.12	-
Reference equivalent load	$R_{ac,0}$	320	Ω
Load variation range	$\Delta R_{ac,SP}$	44-320	Ω
Coupling coefficient variation range	Δk	0.1-0.25	-

Considering the reference parameters f_0 , k_0 , $R_{ac,0}$, $G_{v,max,0}$ of Tab. 3.6 and applying the design procedure of Fig. 3.12, the voltage behavior of the resonant tank as a function of the frequency is shown in Fig. 3.13a for different loads and in Fig. 3.13b for different coupling coefficients. The voltage gain is plotted considering the whole load variation of S-P compensation, which is given in Tab. 3.4. What it is worth noticing is the fact that to avoid bifurcation phenomena the system must be designed according to the maximum equivalent load resistance, which is in this case $R_{ac,max} = 320\Omega$. In addition, to ensure to have enough voltage gain to withstand the battery voltage variation, the maximum voltage gain must be chosen with a safety margin. Besides, for dropping inside the SAE J2954 frequency range and allowing the primary inverter to commute in ZVS, which is above resonance, the resonant frequency is chosen to be 82 KHz. Fig. 3.13a clearly shows that, at resonance, S-P compensation is not load-independent due to wide load variation and, as it can be noticed from Fig. 3.13b, it is not coupling-independent as the distance between transmitting and receiving coils increases the transmitted power decreases.

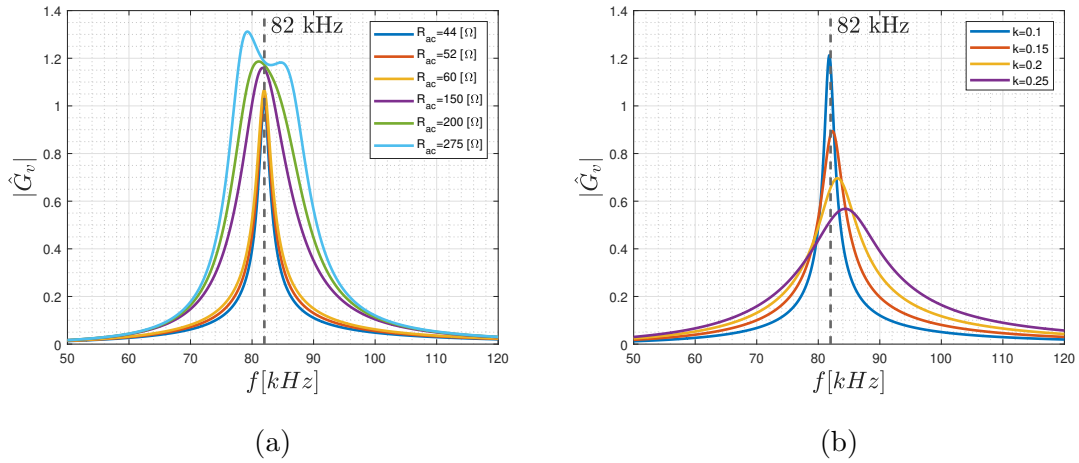


Figure 3.13: Voltage gain behavior for S-P compensation at (a) different equivalent loads (b) different coupling coefficients, for a load of $R_{ac} = 60[\Omega]$.

Although the transconductance presents similar shape with respect to the voltage gain, due to wide load range variation it does not show any parameter-independent characteristic for the transconductance gain, for both load and coupling coefficient variations, as confirmed by Fig. 3.14. The module of the resonant tank input

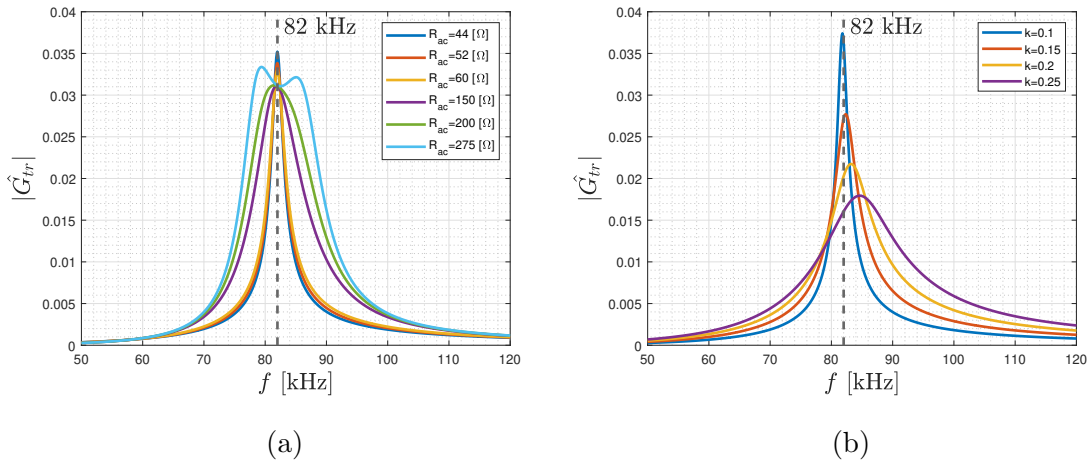


Figure 3.14: Transconductance gain behavior for S-P compensation at (a) different equivalent loads (b) different coupling coefficients, for a load of $R_{ac} = 60[\Omega]$.

impedance seen at the resonant tank terminals of primary side or, equivalently, at the middle point outputs of inverter legs is shown in Fig. 3.15a. As for definition of resonance, the impedance is minimized at resonance. However, as it is also

confirmed by Fig. 3.15b, the proposed design procedure does not compensate the whole imaginary part of the impedance and, in fact, there is no zero phase angle at resonance for the reference load. In addition, since the design procedure is based on a reference load, the input impedance could present a minimum only under this load. These are the reasons why, for some loads, the module of the impedance does not present a minimum in correspondence of resonance and does not present ZPA.

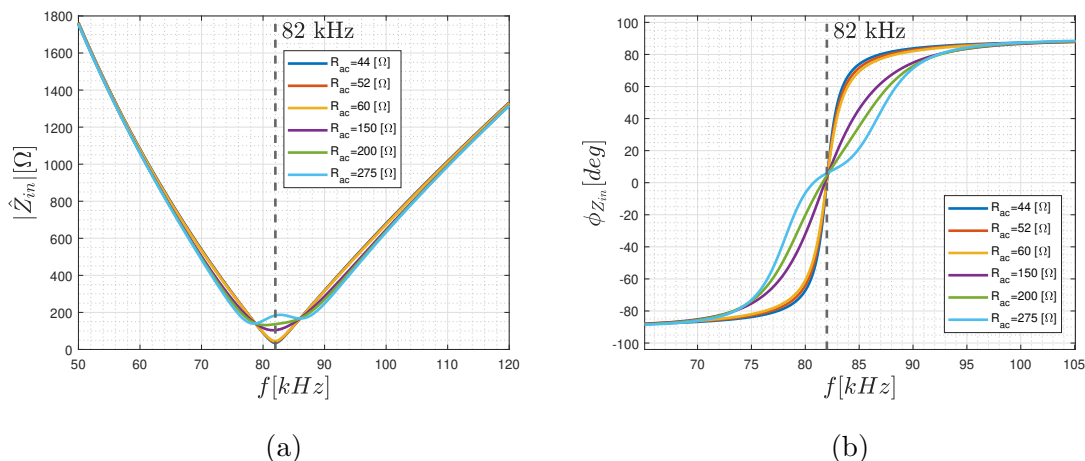


Figure 3.15: Equivalent input impedance seen at the terminals of the primary side, which corresponds to the middle point outputs of the inverter legs. (a) Input impedance module and (b) input impedance phase angle.

It is also interesting to illustrate how the design procedure is affected by the choice of reference parameters. A sensitivity analysis produces a variation of:

1) *Resonance frequency*

The resonance frequency variation produces a shift, in the frequency axis, of the voltage gain and input impedance characteristic. In fact, by frequency controlling the system, with a resonance frequency of 86 kHz, the frequency range requested for fully recharging the battery drops outside the SAE J2954 range, as shown in Fig. 3.16. Aside from a shift, no different shapes in the parameters are detected.

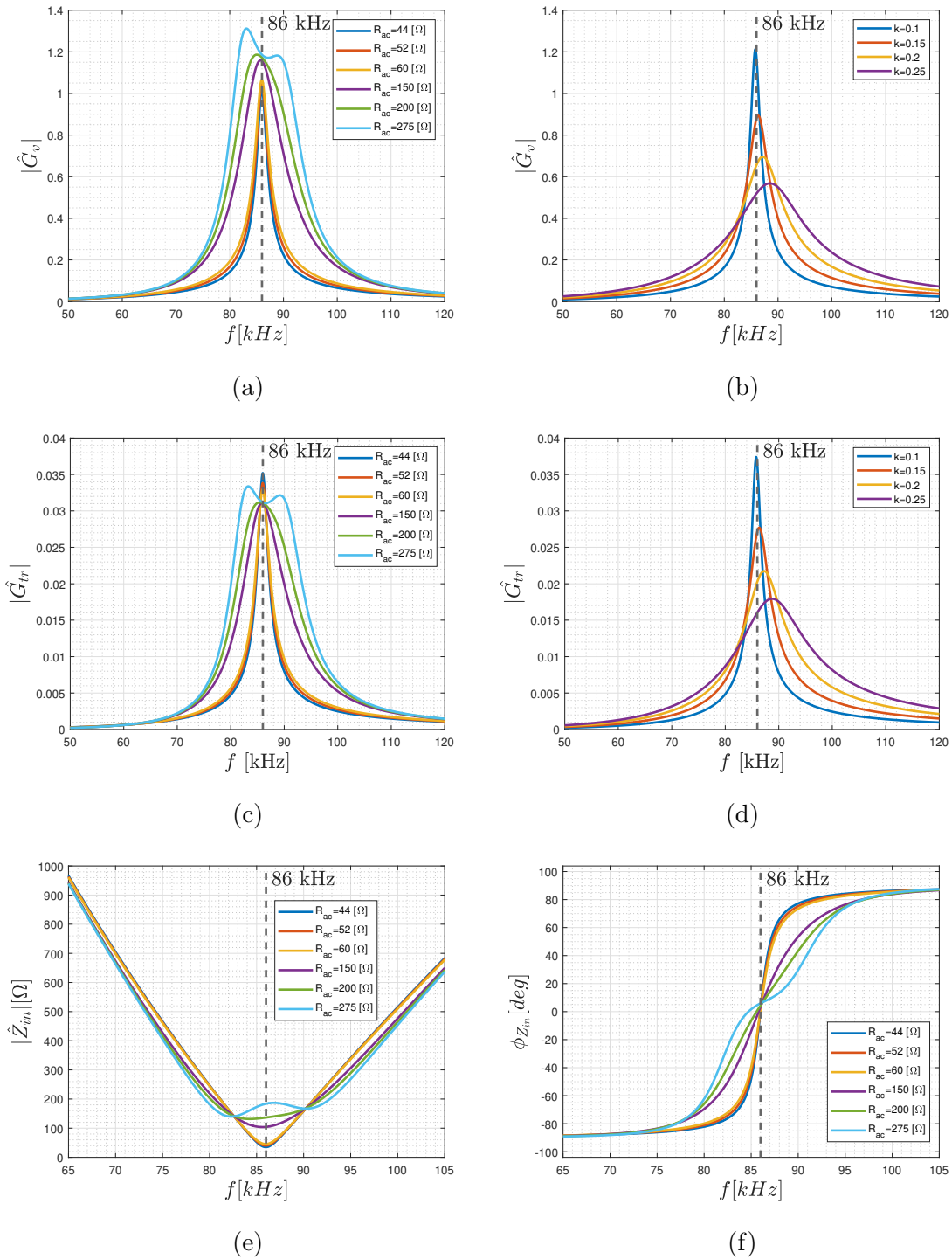


Figure 3.16: Effects of sensitivity analysis when changing the reference resonant frequency for (a) voltage gain for different loads (b) voltage gain for different coupling coefficients (c) transconductance gain for different loads (d) transconductance gain for different coupling coefficients (e) input impedance module and (f) input impedance phase angle. The reference resonant frequency is set to 86 kHz.

2) *Reference maximum voltage gain*

Reducing the maximum voltage gain might be crucial to ensure to have enough voltage to fully recharge the battery in the whole coupling coefficient range. In fact, from Fig. 3.17b it is noticeable that from $G_{v,max,0} = 0.9$ and $k = 0.15$ is not enough voltage to fully recharge the battery since the DC bus is 400V, the primary voltage 509V and the maximum battery voltage is 420V. No significant variations are detected in the input impedance, as shown in Fig. 3.17e and Fig. 3.17f.

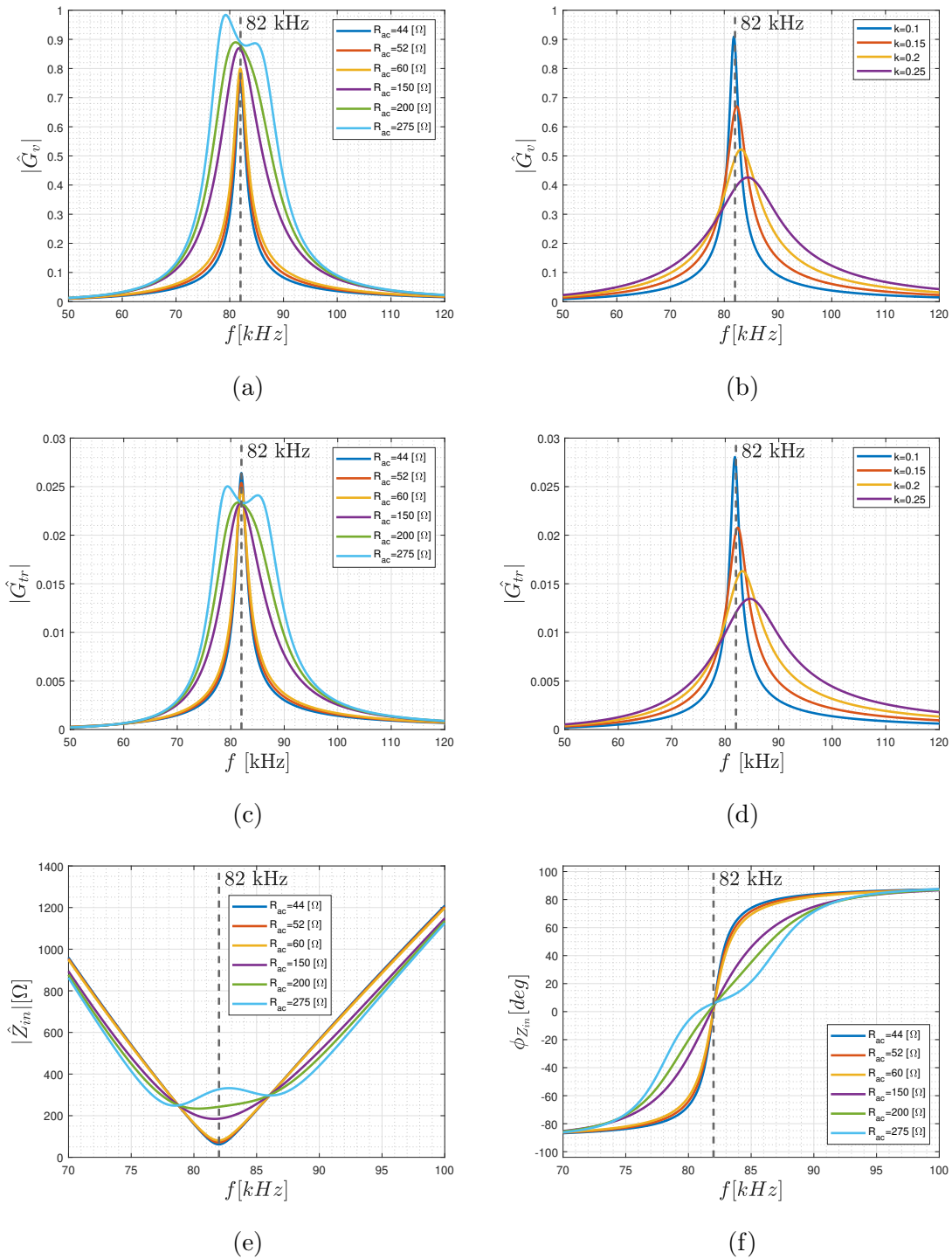


Figure 3.17: Effects of sensitivity analysis when changing the reference maximum voltage gain for (a) voltage gain for different loads (b) voltage gain for different coupling coefficients (c) transconductance gain for different loads (d) transconductance gain for different coupling coefficients (e) input impedance module and (f) input impedance phase angle. The reference maximum voltage gain is set to 0.9.

3) Reference coupling coefficient

For this test, the reference coupling coefficient is set to 0.22. For what concerns Fig. 3.18a, the voltage gain does not change depending on the load. Indeed, what changes is the voltage gain depending on the coupling coefficient. In fact, k_0 is now centered at resonance, leading to have all the values lower than $k_0 = 0.22$ on the right-hand side of resonance and therefore it might become even harder to fulfil the battery voltage range as the reference maximum voltage gain is not properly set, as testified by Fig. 3.18b. This effect is also reflected on the primary impedance phase angle, leading to have some curves, especially for small loads, which exhibit zero crossing before resonance, Fig. 3.18f.

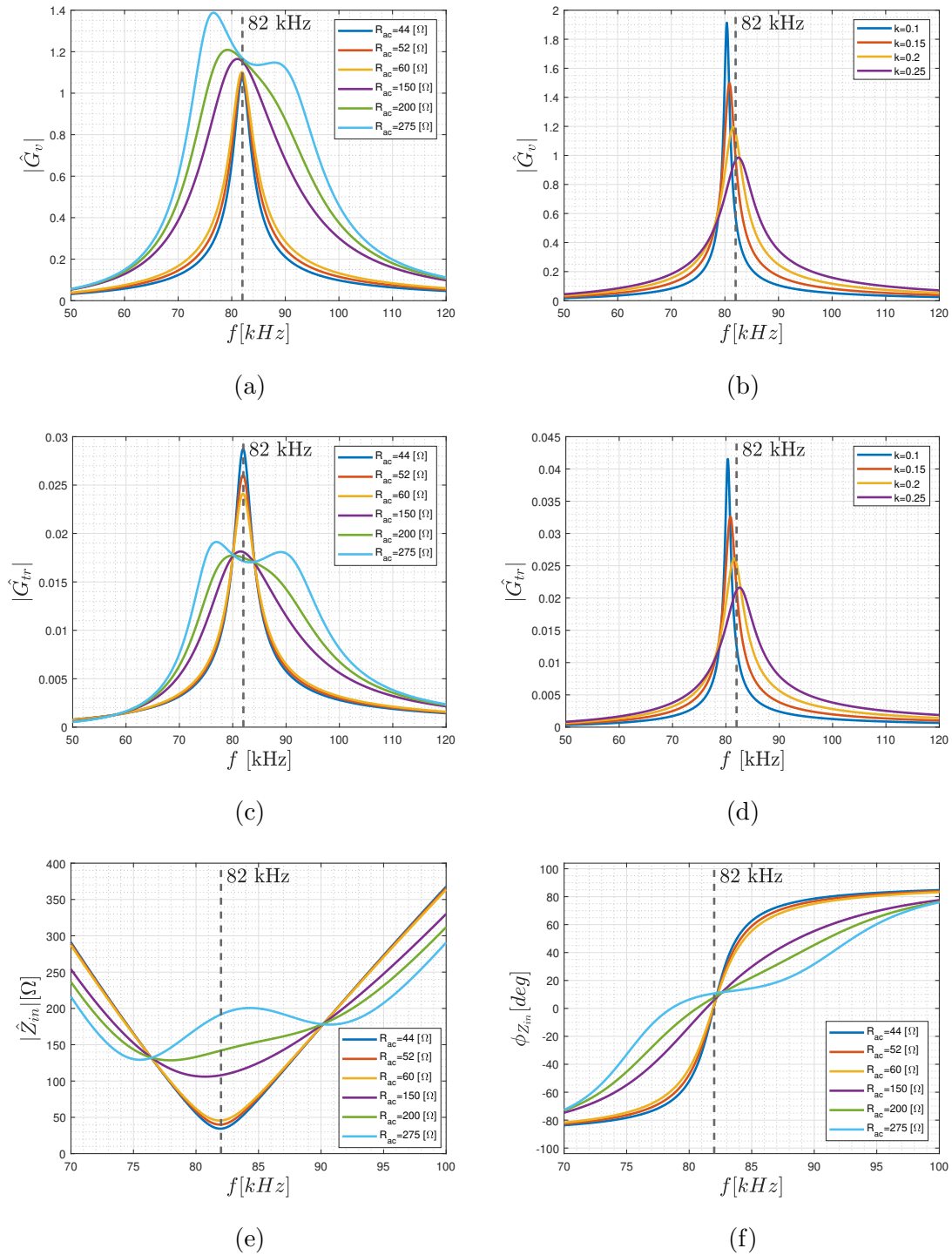


Figure 3.18: Effects of sensitivity analysis when changing the reference coupling coefficient for (a) voltage gain for different loads (b) voltage gain for different coupling coefficients (c) transconductance gain for different loads (d) transconductance gain for different coupling coefficients (e) input impedance module and (f) input impedance phase angle. The reference coupling coefficient is set to 0.22.

4) *Reference equivalent load*

The most impacting parameter is the reference equivalent load, which is set to the transition point from CC mode to CV mode. It corresponds to the maximum power point, and assumes a value of 60Ω . As it is noticeable from Fig. 3.19a and Fig. 3.19b, the voltage gain presents bifurcation, also violating a system requirement. In addition, bifurcation phenomena also exceeds the maximum voltage gain imposed by design and the input impedance is strongly distorted, leading to instability, as testified by Fig. 3.19e and Fig. 3.19f.

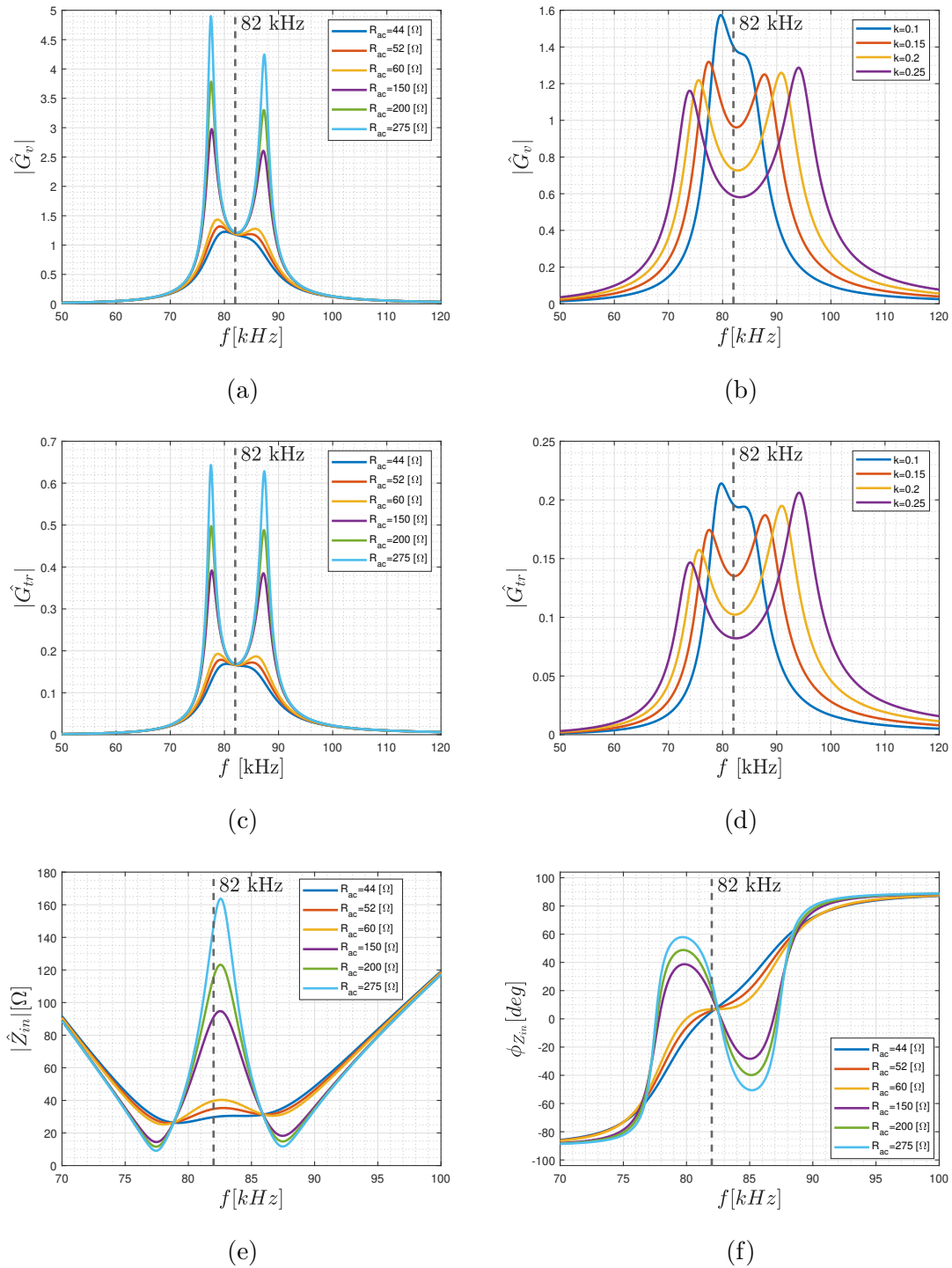


Figure 3.19: Effects of sensitivity analysis when changing the reference equivalent for (a) voltage gain for different loads (b) voltage gain for different coupling coefficients (c) transconductance gain for different loads (d) transconductance gain for different coupling coefficients (e) input impedance module and (f) input impedance phase angle. The reference equivalent load is set to 60Ω .

3.3.2 Series-Series (S-S)

A similar design procedure can be also carried out for S-S compensation. Although the concept behind the algorithm is the same, there are mainly two differences: the first one is related to the equation of the circuit, which is obviously different, and the second concerns the load and coupling independent behavior at resonance frequency. For S-S compensation, it cannot be achieved with constant output voltage through the voltage gain, but it is achieved through the transconductance gain, which means constant output current, considering the primary voltage a parameter.

Similarly to Subsection 3.3.1, the total link efficiency can be expressed as [22, 53]:

$$\begin{aligned}\eta_{link} &= \frac{P_2}{P_1} = \frac{|\hat{V}_2|^2}{\operatorname{Re}\left[\hat{V}_{L1}\hat{I}_{L1}^*\right]} \\ &= \frac{k^2 Q_1 \alpha}{\left(\alpha + k^2 Q_1 + \frac{1}{Q_2}\right)\left(\alpha + \frac{1}{Q_2}\right)}.\end{aligned}\quad (3.44)$$

This expression is also independent of primary coil tuning. The secondary capacity value that maximizes the efficiency is found enforcing:

$$\frac{\partial \eta_{link}}{\partial \alpha} = 0 \quad (3.45)$$

from which is possible to get the optimum α for the S-S compensation:

$$\alpha_{opt} = \frac{\sqrt{1 + k_0^2 Q_1 Q_2}}{Q_2} \quad (3.46)$$

The optimum value of secondary compensation capacitor follows directly from the definition of α_{opt} :

$$C_{2_{opt}} = \frac{\alpha_{opt}}{\omega_0 R_{ac,0}} \quad (3.47)$$

which corresponds to the same formula of $C_{2_{opt}}$ for S-P compensation, but it must be noticed that α_{opt} is different. Keeping the hypothesis of not designing the ZPA, but to ensure constant output current in S-P compensation and constant output voltage in S-P compensation. Indeed, the secondary self-inductance results substituting Eq. 3.47 into Eq. 3.46 and results:

$$L_{2_{opt}} = \frac{R_{ac,0}}{\alpha_{opt} \omega_0}. \quad (3.48)$$

For this configuration, the voltage gain can be rewritten in terms of α , Q_1 and Q_2 :

$$|\hat{G}_v| = \sqrt{\frac{L_2}{L_1}} \left(\frac{k_0 Q_1 Q_2 \alpha}{k_0^2 Q_1 Q_2 + \alpha Q_2 + 1} \right). \quad (3.49)$$

From Eq. 3.49 the optimum primary self-inductance optimum value can be obtained:

$$L_{1_{opt}} = L_{2_{opt}} \left(\frac{1}{|\hat{G}_v|} \frac{k_0 Q_1 Q_2 \alpha}{k_0^2 Q_1 Q_2 + \alpha Q_2 + 1} \right)^2 \quad (3.50)$$

substituting α with α_{opt} it holds:

$$L_{1_{opt}} = L_{2_{opt}} \left(\frac{1}{|\hat{G}_v|} \frac{k_0 Q_1 Q_2 \alpha_{opt}}{k_0^2 Q_1 Q_2 + \alpha_{opt} Q_2 + 1} \right)^2. \quad (3.51)$$

To conclude the design procedure, the optimum primary compensation capacitor comes from Eq. 3.50:

$$C_{1_{opt}} = \frac{1}{\omega_0^2 L_{1_{opt}}}. \quad (3.52)$$

For the sake of completeness, the flowchart summarizing the design procedure for S-S compensation is also given in Fig. 3.20.

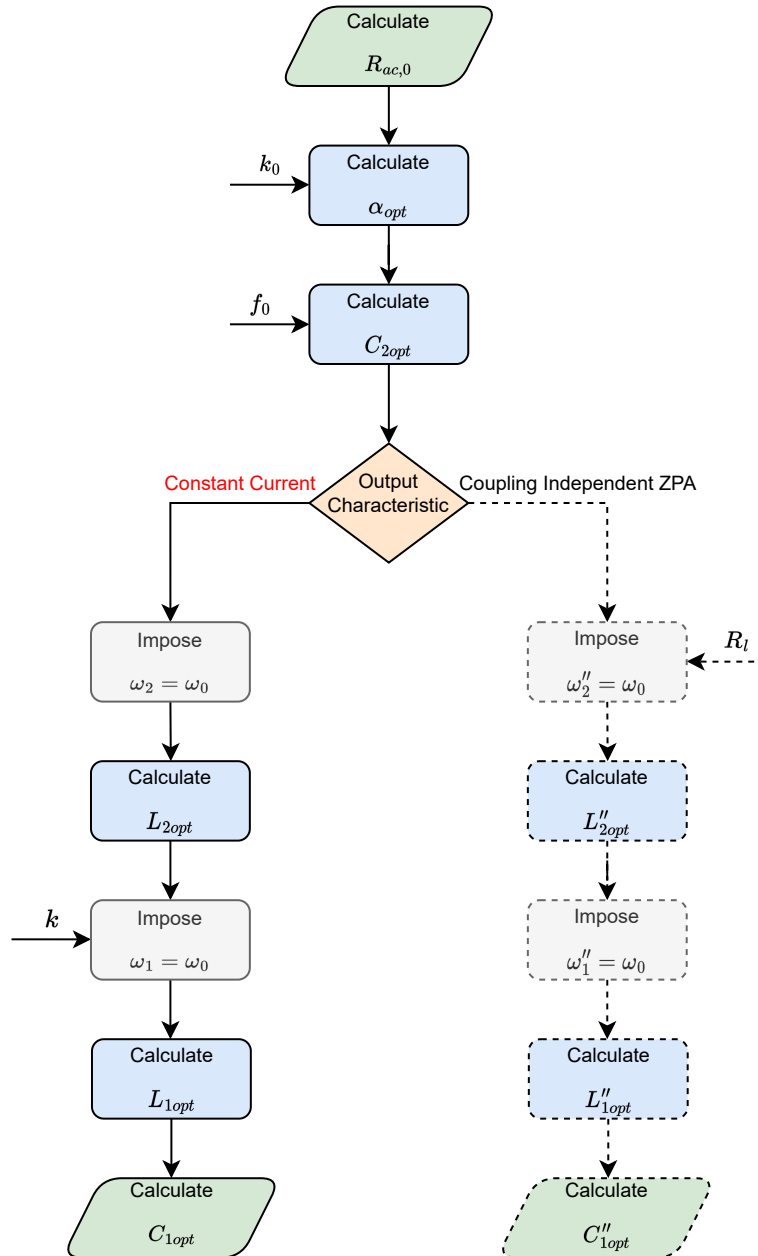


Figure 3.20: Flowchart for S-S compensation illustrating the design procedure for constant output current. The load resistance R_l and the coupling coefficient k refer to actual parameters during variable operating conditions.

As it is noticeable from Tab. 3.7, which collects the algorithm outputs for S-S compensation, the same reference parameters f_0 , k_0 , $G_{tr,max,0}$ are selected for the S-S compensation. The first difference during design refers to the choice of reference equivalent load $R_{ac,0}$. As depicted in Tab. 3.4, the equivalent load seen at the secondary side output terminal varies depending on the compensation topology.

Table 3.7: System parameters, for S-S compensation, obtained from the optimum design procedure.

<i>Quantity</i>	<i>Symbol</i>	<i>Value</i>	<i>Unit of Measure</i>
Primary self-inductance	L_1	0.336	mH
Secondary self-inductance	L_2	0.503	mH
Primary compensation capacitor	C_1	12.06	nF
Secondary self-inductance	C_2	8.06	nF
Reference max transconductance gain	$G_{tr,max,0}$	1.2	-
Reference resonant frequency	f_0	79	kHz
Reference coupling coefficient	k_0	0.12	-
Reference equivalent load	$R_{ac,0}$	30	Ω
Load variation range	$\Delta R_{ac,SS}$	28-240	Ω
Coupling coefficient variation range	Δk	0.1-0.25	-

Considering the reference parameters f_0 , k_0 , $R_{ac,0}$, $G_{tr,max,0}$ of Tab. 3.7 and applying the design procedure of Fig. 3.20, the voltage behavior of the resonant tank as a function of the frequency is shown in Fig. 3.21a for different loads and in Fig. 3.21b for different coupling coefficients. The voltage gain is plotted considering the whole load variation of S-S compensation, which is given in Tab. 3.4. What it is worth noticing is the fact that, unlike S-P compensation must be designed according to the maximum equivalent load resistance to avoid bifurcation phenomena, in S-S compensation the reference equivalent load has to be set really close to the minimum equivalent load resistance, which is $R_{ac,min} = 30\Omega$. According to S-S compensation, to ensure to have enough gain to withstand the battery voltage and current varia-

tion, the maximum transconductance gain must be chosen with a safety margin and, for dropping inside the SAE J2954 frequency range the resonant frequency is chosen to be 79 KHz. As it happened for S-P compensation, Fig. 3.21a confirms that, at resonance, S-S compensation is not load-independent. In fact, S-S compensation should present a load-independent point in the transconductance gain. However, this does not happen. The cause can be imputed to wide load variation and, as it is noticeable from Fig. 3.21b, it is not coupling-independent as the distance between transmitting and receiving coils increases the transmitted power decreases. Differently from S-P compensation in which the voltage gain presents some bifurcation phenomena as the load variation and not when the coupling coefficient changes, here the situation is reversed. In fact, S-S compensation does not present any bifurcation in almost all the load variations, except for the equivalent load at very beginning of the CC-CV charging cycle. Whereas this compensation topology presents significant bifurcation as the coupling coefficient changes. Same considerations related to bifurcation, for load and coupling coefficient variations, can be extended for the transconductance gain.

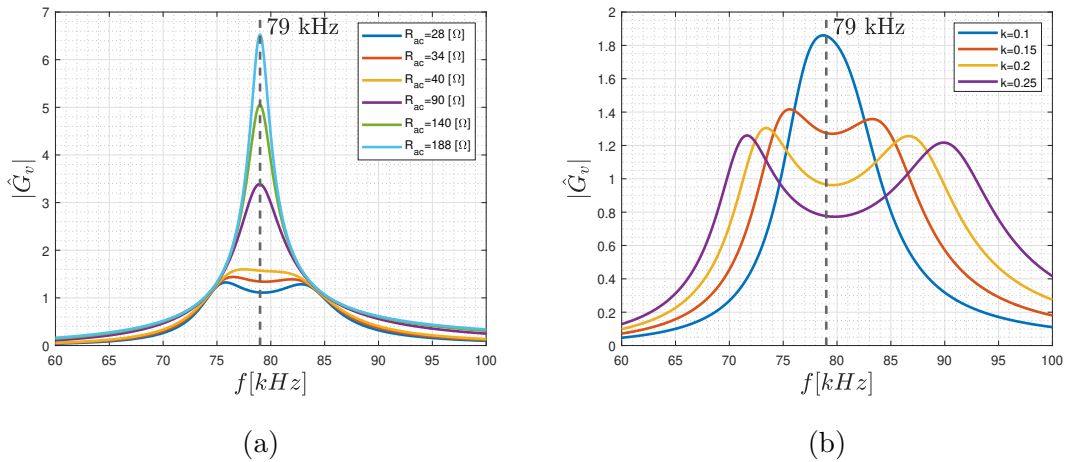


Figure 3.21: Voltage gain behavior for S-S compensation at (a) different equivalent loads (b) different coupling coefficients, for a load of $R_{ac} = 40[\Omega]$.

In addition, although the transconductance presents similar shape with respect to the voltage gain, due to wide load range variation it does not show any parameter-independent characteristic for both load and coupling coefficient variations, as con-

firmed by Fig. 3.22. The module of the resonant tank input impedance seen at the

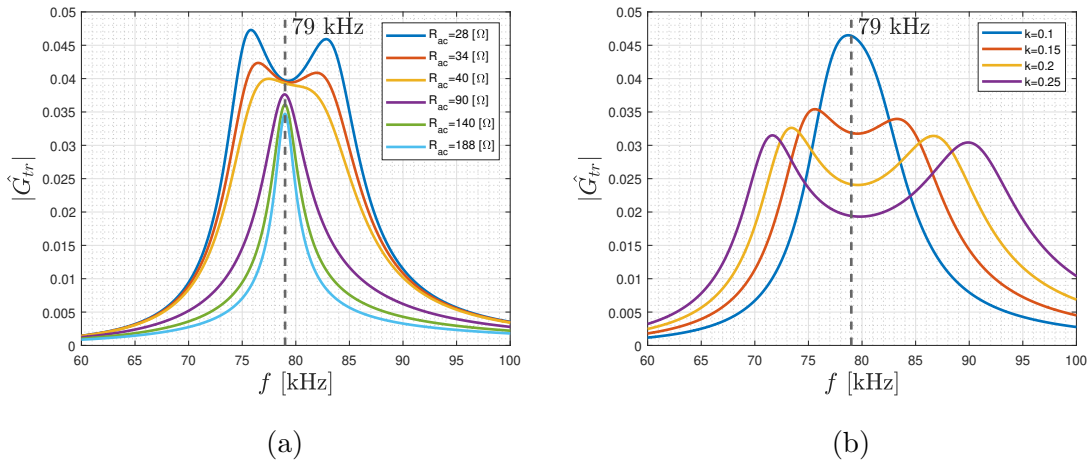


Figure 3.22: Transconductance gain behavior for S-S compensation at (a) different equivalent loads (b) different coupling coefficients, for a load of $R_{ac} = 40[\Omega]$.

resonant tank terminals of primary side or, equivalently, at the middle point outputs of inverter legs is shown in Fig. 3.23a. As for S-P compensation, Fig. 3.23b shows that the proposed design procedure does not compensate the whole imaginary part of the impedance and, in fact, there is no zero phase angle at resonance for the reference load.

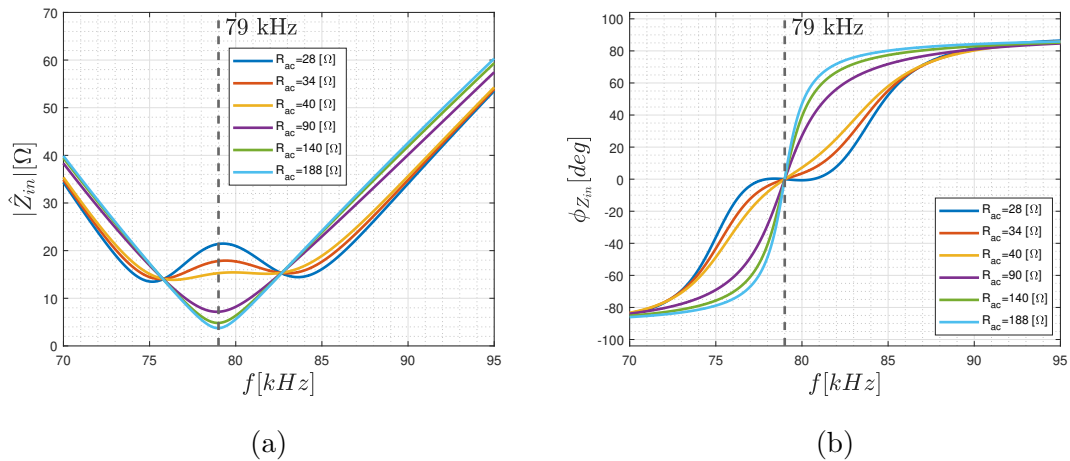


Figure 3.23: Equivalent input impedance seen at the terminals of primary side, which corresponds to the middle point outputs of the inverter legs. (a) Input impedance module and (b) input impedance phase angle.

In this Subsection, the sensitivity is omitted since it produces the same effects of S-P compensation.

Chapter 4

Power Electronics Control Optimization

Based on the results of the state-of-the-art, in this Chapter an innovative control logic for primary inverter is proposed. It takes advantage of benefits of the variable frequency and variable phase-shift, between leading and lagging legs of primary inverter, control techniques being able to combine and achieve simultaneously three main targets:

- Maximize the efficiency throughout the charging cycle
- Guarantee a wide output voltage range, which corresponds to a wide load variation, suitable for different battery pack configurations
- Minimize the frequency variation

Due to the generality of the proposed control logic, even though it is specific for WPT battery chargers, it can be applied to any resonant application.

4.1 Power Electronics Circuit Topology

Power electronics is a key factor for WPTBCs. The overall efficiency from the AC grid up to the battery strongly depends on the performance of the converters. As a consequence, their topological configuration and control have been object of study

from researchers for since a long time. As shown in Fig. 4.1, a typical WPT system includes, in the primary side of the resonant tank, a front-end AC/DC converter to correct the PF at the AC grid connection to meet low Total Harmonic Distortion (THD) [11]. The following stage is a primary DC/AC inverter to convert the DC voltage provided by the PF to a high frequency bipolar voltage pulses with variable frequency, duty cycle and phase-shift between its leading and lagging leg. The secondary side of the resonant tank consists of a rectification stage, which may be passive using diodes or active adopting power switches. Then, an optional DC/DC converter might be included in the architecture for additional voltage regulation. As already mentioned, the DC/DC converter performs two main functions: charging the battery following the CC-CV charging cycle and matching the load impedance with the source impedance for optimum power transfer [55, 56]. It must be pointed out that optimum power transfer might not correspond to maximum efficiency. In the following, only the configuration topologies are treated. For what concerns the power electronics control techniques, an exhaustive discussion is given in the next sections.

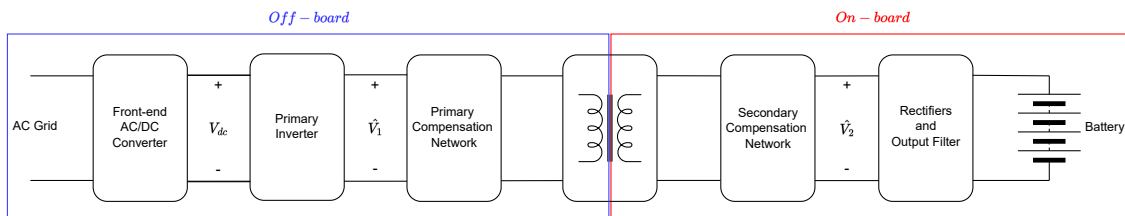


Figure 4.1: Power electronics stages for WPTBCs.

The front-end AC/DC converter might be fed by the primary inverter either as a voltage source or as a current source. Generally, when feeding the primary inverter through a current source the primary compensation network adopts a parallel compensation. Although lowering the circulating current in the power electronics circuit since a parallel capacitor creates a low impedance path for the circulating currents, the voltage stress on the switches increases [57, 58, 59, 60]. A sketch of current-fed converters are shown in Fig. 4.2. It employs a CCL-LC compensation. An additional drawback of current-fed inverters is the size of primary inductor L_{dc} , which is much bigger than traditional voltage-fed inverters.

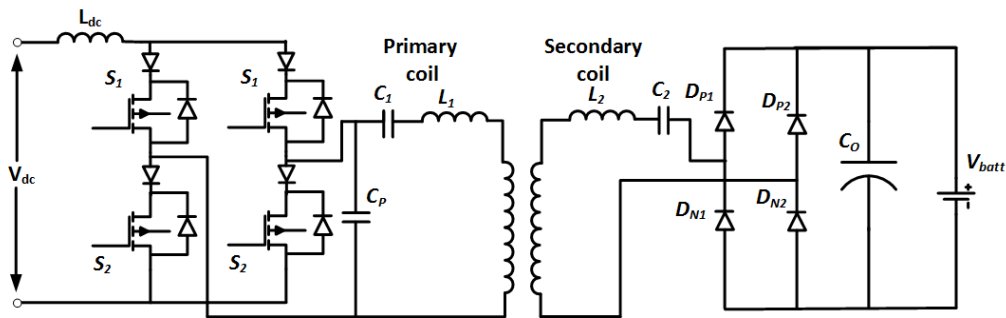


Figure 4.2: Current-fed converter [57].

A further distinction in power electronics converter might be based on the power flow direction. Unidirectional chargers are only able to transfer the energy from the AC grid to the battery vehicle (G2V), while bidirectional chargers can exchange energy in both directions (V2G). The main difference between G2V and V2G converters relies on the rectifiers on the secondary stage. G2V can use both diodes or active switches, while V2G must use the latter ones. Due to the fact that bidirectional converters are not widely adopted in industrial applications yet, in the following, only unidirectional converters with diodes rectifiers on the secondary side will be investigated. The most common configuration for primary inverter remains the full bridge, while other possible configurations are listed below:

1) Matrix converter:

It brings the advantage of reducing the number of conversion stages, leading to a consequent reduction of semiconductor devices, avoiding the DC link [61, 62]. Due to the fact that less active components are involved, the efficiency is high. However, higher stress is applied to semiconductors leading to a low power rating, Fig. 4.3

PROs: Less number of conversion stages, no DC link, high efficiency.

CONs: High stress on semiconductors, low power rating.

2) Multiphase converter:

To overcome the power rating limitation of Matrix converter, reference [63] and [64] proposes a multiphase inverter. It consists of a 3-phase converter where each phase is connected to a two interphase transformers to share the current between parallel

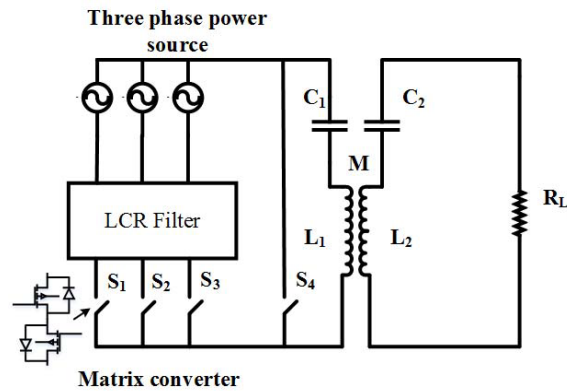


Figure 4.3: Matrix converter for G2V applications [61].

inverter legs. Fig. 4.4 presents a multiphase converter S-S compensated. However, as the power rating increases the cost increases.

PROs: High power applications.

CONs: High number of components and high costs.

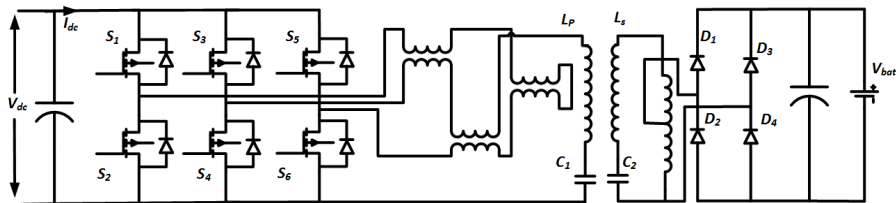


Figure 4.4: Multiphase converter for G2V applications [63].

3) Modular high power converter:

The step forward introduces modular high-power systems such as the one shown in Fig. 4.5. It integrates multiple low-power systems to increase power levels [65]. However, several primary and secondary coils are required.

PROs: Modular architecture and low switch losses.

CONs: Multiple primary and secondary coils.

4) Parallel LCL-T converter:

As illustrated in Fig. 4.6 on the primary side multiple primary coils are connected in series with an LCL resonant circuit, while in secondary side multiple coils are connected in parallel with a parallel compensation [67]. The advantages brought

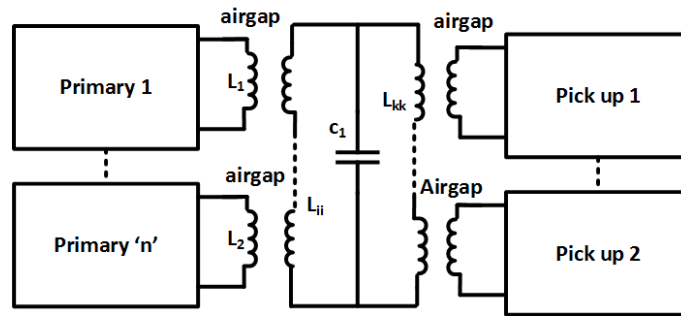


Figure 4.5: Modular high power converter for G2V applications [66].

are related to low costs, minimization of uneven power sharing and fault-tolerant.

PROs: Low costs, fault-tolerant and modular structure.

CONs: Multiple primary and secondary coils.

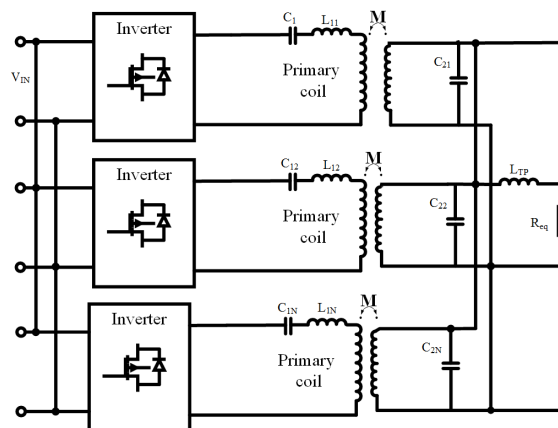


Figure 4.6: Parallel LCL-T topology for high-power G2V applications [67].

5) Cascade multilevel converter:

The phase-shift control is adopted to control the output voltage and to eliminate selected harmonics. Even if this converter topology, shown in Fig. 4.7, is suitable for high power applications it requires multiple power supplies to increase voltage levels, resulting in additional components, losses and costs [68].

PROs: High power applications, harmonics cancellation.

CONs: Multiple power supplies, low efficiency and high costs.

Although several circuit topology for controlling the power exchange between

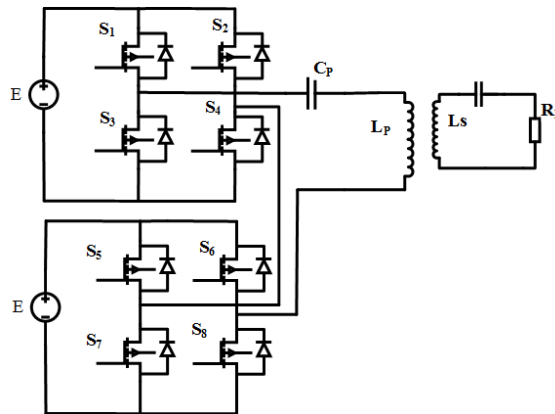


Figure 4.7: Cascade multilevel converter for G2V applications [68].

transmitting coil and receiving coil are present, the full bridge inverter, at the primary side, coupled with H-bridge diode rectifiers, at the secondary side, is the best trade off for complexity, number of components, costs and size especially for those applications who do not drop inside the research field, such as industrial or commercial applications [9]. Fig. 4.1 depicts the circuit topology that is object of study hereinafter.

4.2 Power Electronics Control Techniques

The upstream battery DC/DC converter of Fig. 4.1 is avoided and the rectifying stage is formed by a passive diode bridge only, providing the architecture illustrated in Fig. 4.8a for S-P compensation and Fig. 4.8b for S-S compensation. This solution allows the overall losses, complexity and cost of the WPT battery charger to be dramatically reduced, but it requires the secondary output DC voltage to be controlled by acting on the primary inverter output voltage.

Despite the compensation topology of WPT systems may vary depending on the considered case study, the circuit topology of WPT battery chargers is similar to one of wired LLC resonant converters, for which several control strategies are presented and discussed in literature [69]. In addition, it must be noticed that thousands of different DC/DC isolated converters have been proposed in literature and the related control strategies must be developed according to the particular topology. Thus, for a meaningful discussion, only the control strategies applied to unidirectional and

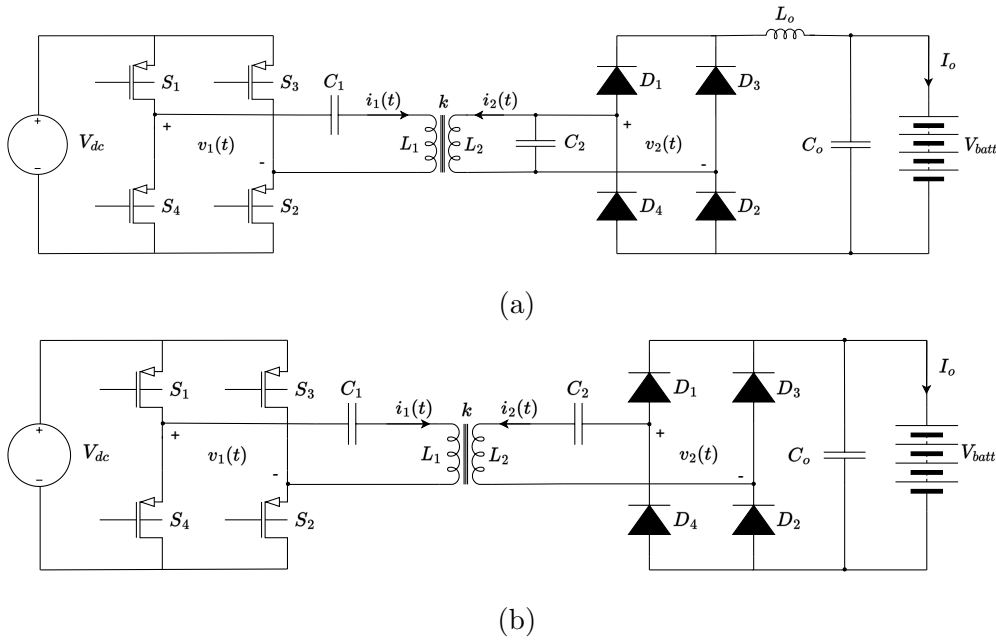


Figure 4.8: Single stage system architecture for power electronic control of (a) S-P compensation and (b) S-S compensation.

single stage WPT battery chargers are considered hereinafter. For these converters, what is known from the state-of-the-art is that there are mainly three categories of modulation control strategies for the primary inverter:

- Frequency control (FC)
- Phase-shift control or duty-cycle control (PSC)
- Hybrid phase-shift and frequency control (HPSFC)

FC algorithms keep the duty cycle of the input inverter constant and act on the switching frequency, which is chosen according to the desired battery pack voltage, through the resonant tank voltage gain or current, through the resonant tank transconductance gain. The former strategy might allow the primary switches to always commute in ZVS whether the operating point ensures an inductive behaviour of the equivalent impedance seen by the inverter at its output terminals [70, 71, 72]. However, this condition strongly depends on the resonant tank design and the output voltage range must be limited to avoid dramatic drops of the system efficiency. The other strategy for the inverter FC control is based on Maximum Power Point

Tracking (MPPT) algorithms [73, 74] where the optimal frequency is obtained from the maximization of the resonant tank link efficiency. However, using this method ZVS does not always guarantee since the operating point is not based on the voltage gain and therefore on the inductive behaviour of the input impedance.

PSC or duty cycle control algorithms control the inverter output voltage acting on the dead times or on the duty cycle of the gate signals of the switches S_{1-4} . In particular, PSC regulates the displacement (which can be indicated as an angle or a time interval) between the two inverter legs. The phase-shift can be directly related to the duty cycle of the converter [75] and thus these two parameters can be considered equivalent. These control techniques allow the inverter output voltage, which correspond to the resonant tank input one, to be regulated even if it can lead to operations out of ZVS condition and it might increase conduction losses in the coils when a relatively low voltage is applied to the primary side circuitry [69].

Combining PSC and FC methods the hybrid strategy called HPSFC can be obtained. Similarly to PSC and FC, this control technique has been developed for traditional resonant converters [69, 76, 73, 77] allowing wide output voltage range and low reactive power circulation. However, the converter generally requires additional switches and components with respect to the simplest single stage topology. In addition, higher efficiency with respect to FC is not guaranteed [78].

In the frame of WPT systems, these techniques have been applied to a single stage WPT converter in [70], always ensuring the desired voltage level and ZVS. HPSFC has been also implemented in [79], even if the system was designed to achieve a constant current behaviour only and the misalignment between the transmitting and receiver coils was not considered. In [80] the problem of misalignment is addressed, but an DC/DC conversion stage is considered in the receiving side to follow battery charging profile. A more extensive HPSFC implementation is proposed in [81] with a three-loop control strategy. The first two loops are intended for follow the reference current and reference voltage needed for the CC-CV charging cycle profile, while the latter loop is used to detect the phase angle of the input impedance to minimize the circulation of reactive power and to achieve ZVS. However, really accurate current and voltage sensors are needed and different PID controllers are

required to be tuned and synchronized. Moreover, during the CV stage only the battery voltage feedback is provided and the information about the battery current is missing leading to uncontrolled current behaviour. In addition, controlling the RMS values of the primary tank current is not an actual measure and might lead to damage the primary inverter if unwanted current behavior or peaks occur.

4.3 Primary Inverter Control

The aim of this Section is to propose an algorithm that is able to control both the frequency and the phase-shift of the primary inverter following the CC-CV charge cycle illustrated in Fig. 3.10. Main improvements are related to minimize the phase-shift angle for achieving ZVS according to the converter operation, minimize the frequency range to stay as close as possible to resonance and to include effects produced by the coils misalignment. In addition, an optimized relationship between phase-shift and frequency is proposed and the whole system efficiency is mapped for any type of control, allowing to select the best operation mode at any instant.

4.3.1 S-P Compensation

Higher efficiency than FC and PSC along with wide output voltage range operations and narrow frequency range close to resonance, are considered the target requirements for the control algorithm. Hybrid control combines the benefits of FC and PSC strategies and acts on both switching frequency and phase-shift of the inverter legs, requiring a precise relation between the two control variables. Generally speaking, under FC the frequency is chosen according to the desired gain characteristic. For a given operating load and coupling coefficient, when the control variable is the battery current, the frequency is set according to the transconductance gain \hat{G}_{tr} . In fact, \hat{G}_{tr} represents the link between the fundamental component of primary voltage \hat{V}_1 , which is a sinusoidal quantity with constant RMS and peak value. It is provided by the primary inverter, and the reference current I_{batt} . On the other hand, when the control variable is the battery voltage, similar considerations are carried out substituting the transconductance gain with the voltage gain. The optimal operat-

ing condition can be found ensuring that the operating frequency falls into the SAE J2954 range, 79-90 kHz along with ZVS operation of primary inverter. The latter requirements are found by imposing to the design that the input impedance angle ϕ_{in} must be greater than zero. In particular, the input impedance of the resonant tank can be expressed as:

$$\hat{Z}_{in} = \hat{Z}_1 + \frac{(\omega k)^2 L_1 L_2}{\hat{Z}_2 + \frac{R_{ac}}{1 + j\omega C_2 R_{ac}}} \quad (4.1)$$

and the input impedance angle of the tank ϕ_{in} is found as:

$$\phi_{in} = \arctan \frac{\text{Im}[\hat{Z}_{in}]}{\text{Re}[\hat{Z}_{in}]} \quad (4.2)$$

As shown by the control scheme required to operate in FC of Fig. 4.9, the direct control variable for FC is the battery current. Therefore, for a given coupling coefficient the transconductance gain of Fig. 3.14a is required to select the optimum operating frequency. f_{max} and f_{min} correspond to the SAE J2954 limits and S_a refers to the four MOSFET gate signals S_{1-4} of primary inverter needed for piloting the power transistors. When considering the frequency control only, the pilot signal S_a has a constant duty cycle but variable period. The control scheme takes as an input two variables: the reference battery voltage $V_{batt,ref}$, which corresponds to the upper cut-off limit of the battery pack (420V considering the object of this study, Tab. 3.6) and the I_{CC} , which corresponds to the current value during CC stage. When considering real applications, these two variables are set by the user or given by external control units, such as Battery Management System (BMS). As a first step, the difference between the reference voltage and the actual battery voltage enters the PI regulator, which returns in the range $0 - I_{CC}$ a current reference signal, which is in turn compared with the actual battery current and the error enters the second PI regulator. The reference current is negative polarized due to the voltage gain and transconductance gain characteristic. In fact, when the battery voltage (or battery current) has to increase the frequency needs to be decreased. The output of the current PI regulator is a frequency reference value in the range $0 - (f_{max} - f_{min})$. It is compared with f_{max} since at the first iteration, in order to start in safety conditions and to apply minimum voltage, the frequency value needs to be the maximum

one. Then, the actual frequency enters the PWM regulator, which is set to constant duty cycle, and in turn generates the MOSFETs gate signals S_a for primary inverter which returns a primary voltage $v_1(t)$ that is, a resonance, seen as a sinusoidal signal by the resonant tank. The resonant tank, independently by the compensation topology, always returns a secondary voltage $v_2(t)$ which is directly applied to the H-bridge diode rectifiers and therefore to the battery pack.

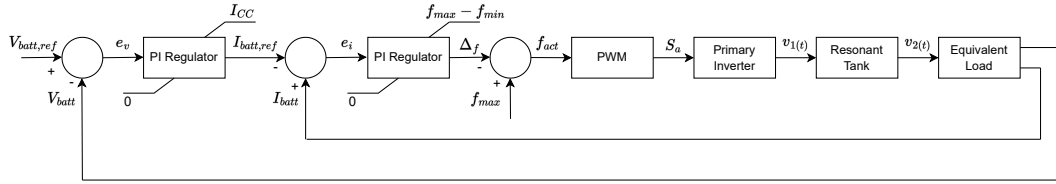


Figure 4.9: Frequency control scheme.

With reference to parameters of S-P compensation of Tab. 3.6, as already done in Section. 3.3 sampling the equivalent profile of battery voltage and current the load seen at the output terminals of the S-P resonant tank can be obtained. It spans in the range $R_{ac,SP} = 44\Omega - 293\Omega$, as recalled in Fig. 4.10a. Since the DC bus is set equal to 400V and the module of primary voltage at the input side of the resonant tank is $|\hat{V}_1| = \frac{4}{\pi}V_{dc} = 509V$ and the reference battery current is a known variable, the optimal transconductance gain, at any load, is known and illustrated in Fig. 4.10b. The FC sets the operating frequency to match the transconductance gain, as illustrated in Fig. 4.10c.

As it is noticeable, for small load, at about 50Ω , the frequency is close to resonance (82 kHz). However, as the load increases the frequency increases. In fact, due to the shape of the transconductance gain, along with module of the primary voltage and the reference battery current, the actual frequency exceeds the SAE J2954 range if the frequency is subjected to FC. The actual frequency, as shown in Fig. 4.10c, exhibits an almost linear behaviour, with a positive slope increasing as the load increases, in all the load variation range.

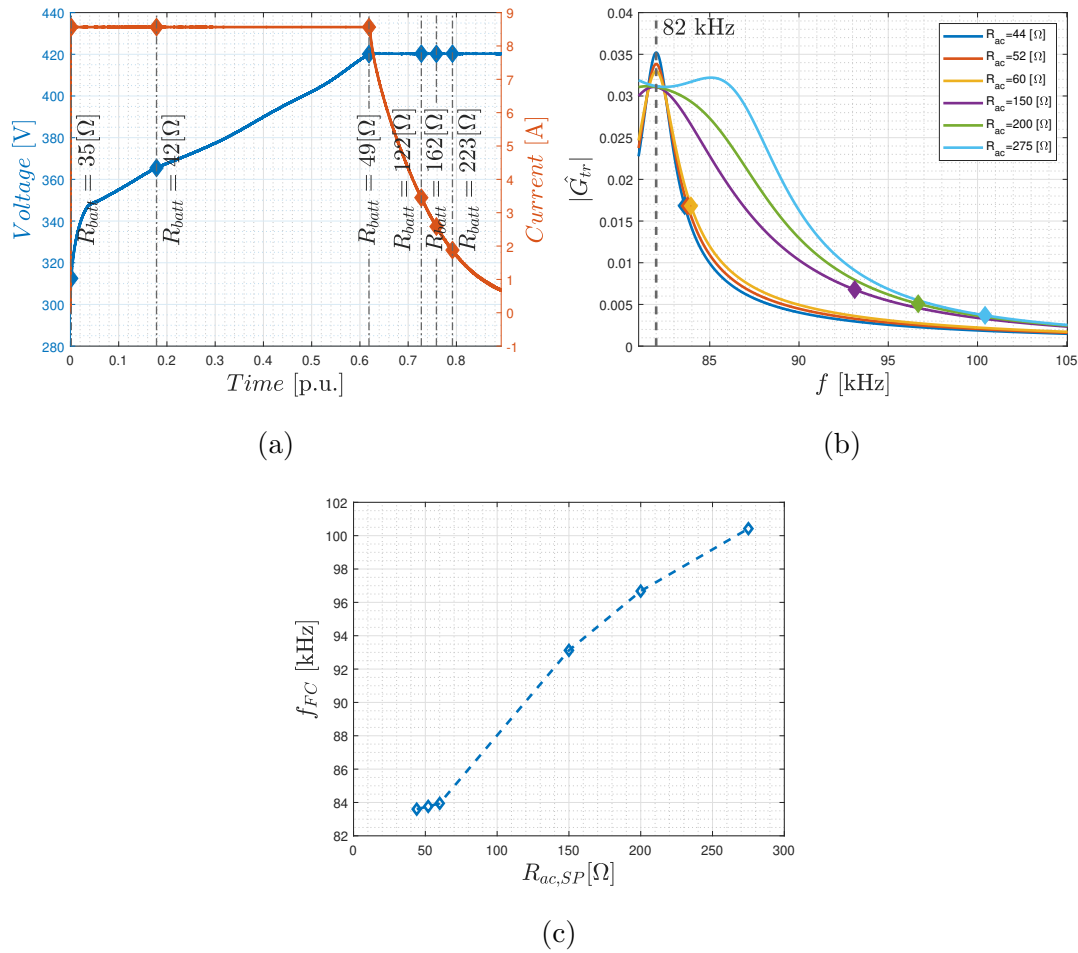


Figure 4.10: (a) Sampled battery voltage and battery current operating points at reference coupling coefficient k_0 . (b) Optimum transconductance gain to match the reference battery current and the input voltage. (c) Operating frequency in S-P compensation under FC, for controlling the battery current.

Additionally, a precise and consistent design also requires the control of the phase-shift between leading leg with switches S_1 - S_4 and lagging leg with switches S_2 - S_3 of the primary inverter of Fig. 4.8. For obvious reasons, the phase-shift varies in between 0° and 180° . For PSC, a suitable model of the power source, which in this case is a full-bridge inverter is mandatory. In particular, being it exploited to control the primary voltage, the relation between the DC bus voltage V_{dc} and the primary voltage \hat{V}_1 must be determined. Considering the fundamental component

of the primary voltage, it is possible to express $v_1(t)$ as:

$$v_1(t) = V_{dc} \sum_{n=1}^{\infty} \frac{4}{n\pi} \cos\left(\frac{n\delta}{2}\right) \cos(n\omega_1 t) \quad (4.3)$$

and then the phasor associated to the fundamental component at the switching angular frequency ω_1 is:

$$\hat{V}_1 = \frac{4}{\pi} V_{dc} \sin\left(\frac{\delta_1}{2}\right) e^{j0}. \quad (4.4)$$

The angle δ_1 corresponds to the phase angle between the outputs of the two inverter legs, which can be expressed in terms of duty cycle D as:

$$\delta_1 = 2 \arcsin D. \quad (4.5)$$

Then, considering the overall voltage gain of the system from the DC bus, downstream the front-end AC/DC converter up to the secondary voltage of the resonant tank, $\hat{G}_{Tv} = \hat{V}_2/V_{dc}$ results:

$$\hat{G}_{Tv} = \hat{G}_v \frac{4}{\pi} \sin\left(\frac{\delta_1}{2}\right). \quad (4.6)$$

Similarly, when the control variable refers to a current, \hat{G}_v must be substituted with the transconductance gain \hat{G}_{tr} , leading to $\hat{G}_{Ttr} = \hat{I}_2/V_{dc}$ results:

$$\hat{G}_{Ttr} = \hat{G}_{tr} \frac{4}{\pi} \sin\left(\frac{\delta_1}{2}\right). \quad (4.7)$$

The \hat{G}_{Ttr} , for different phase-shift values in the SAE J2954 frequency range is shown in Fig. 4.11. The graphs are plotted for different phase-shift values and for a given load. Despite the previous graphs related to the transconductance gain are plotted for different loads, here different loads require different graphs, otherwise considering different phase-shift and loads in the same graphs would result in a 3D plot which may not be representative. Comparing the three plots of Fig. 4.11 it is noticeable that the maximum gain remains fixed as the load changes, instead what changes is the shape of the gain. Some insight of bifurcation are also visible in Fig. 4.11c. In all three figures however the peak gain is regulated by the phase-shift angle, in fact as the phase-shift increases the total transconductance gain decreases.

Similarly to FC, for a given coupling coefficient and load, which are depicted in Tab. 3.6, the control variable remains the battery current and the control scheme

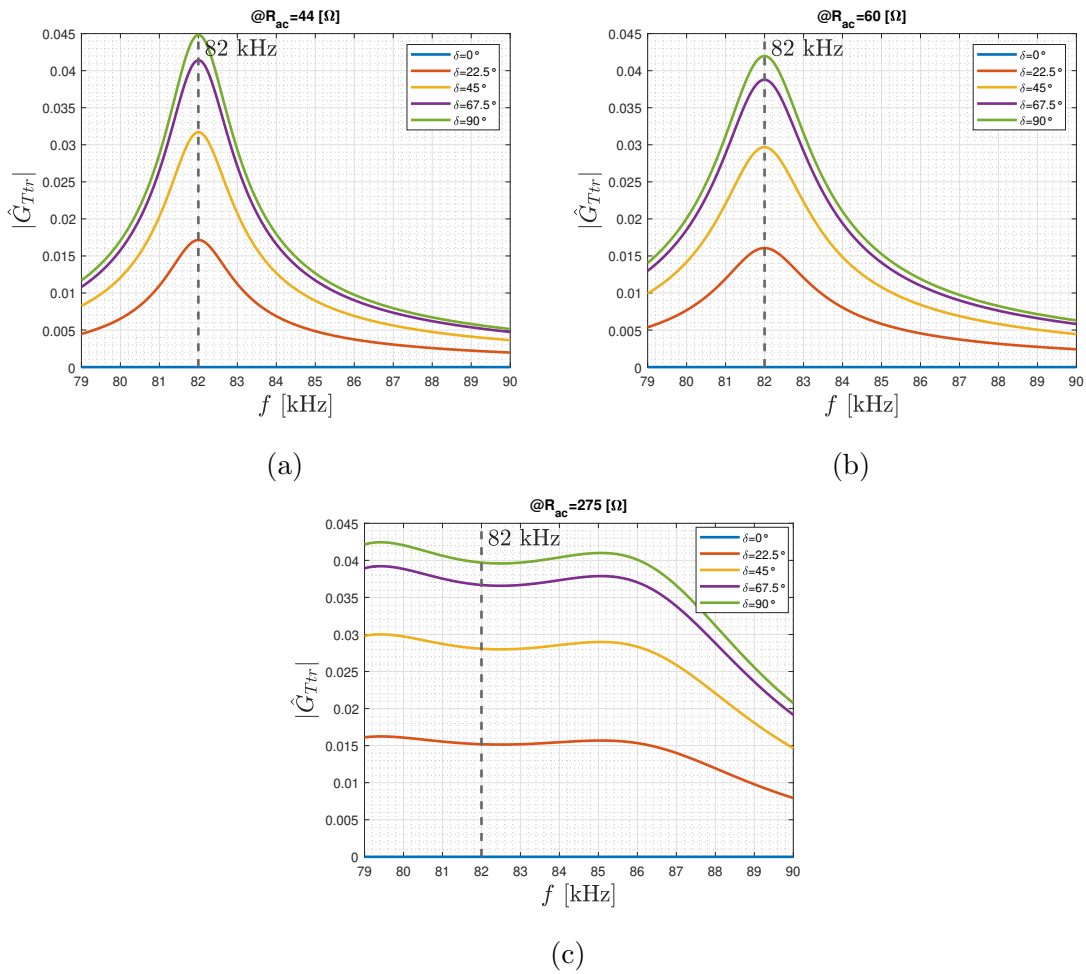


Figure 4.11: Total gain \hat{G}_{Ttr} for different phase-shift values, calculated at reference coupling coefficient k_0 . Three different equivalent loads are considered: (a) $R_{ac,min}$, (b) $R_{ac}@P_{max}$, (c) $R_{ac,max}$.

which selects the appropriate phase-shift to apply between leading and lagging inverter leg is shown in Fig. 4.12. The working principle is the same of the FC above-described, with two differences: the first one is the positive sign of the current, since if the battery voltage (or battery current) has to increase, the phase-shift needs to increase. The second one is related to saturation limits of the current PI regulator. In this case they are not anymore associated to the frequency range but with the phase-shift range.

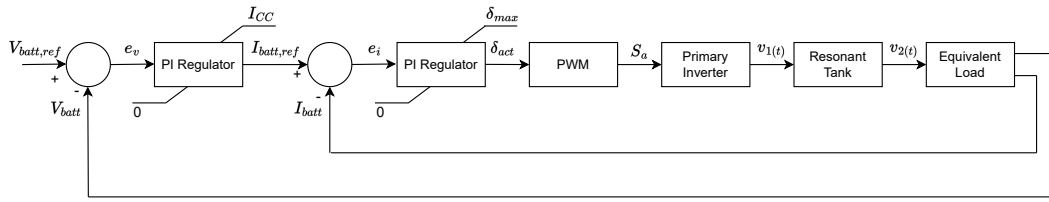


Figure 4.12: Phase-shift control scheme.

The resulting plots, considering the total \hat{G}_{Tr} gain to select the right phase-shift angle to match the reference battery current are shown in Fig. 4.13. The algorithm fixes the frequency to the optimal one, which is the resonance frequency, and outputs the δ values to be applied over the complete CC-CV charging cycle. In this case, both Fig. 4.13a and Fig. 4.13b illustrate the transconductance gain and the total gain as a function for different loads, since the appropriate phase-shift value has already been selected by the algorithm and indicated with a rhombus-shaped pointer, by the algorithm. For loads above 60Ω , specifically the curves of 150Ω , 200Ω and 275Ω the current decreases since the battery enters in the CV mode. Therefore, the total gain needs to be decreased and this is achieved by more phase-shift the legs, as also testified by Fig. 4.13c that coherently increases the phase-shift angle.

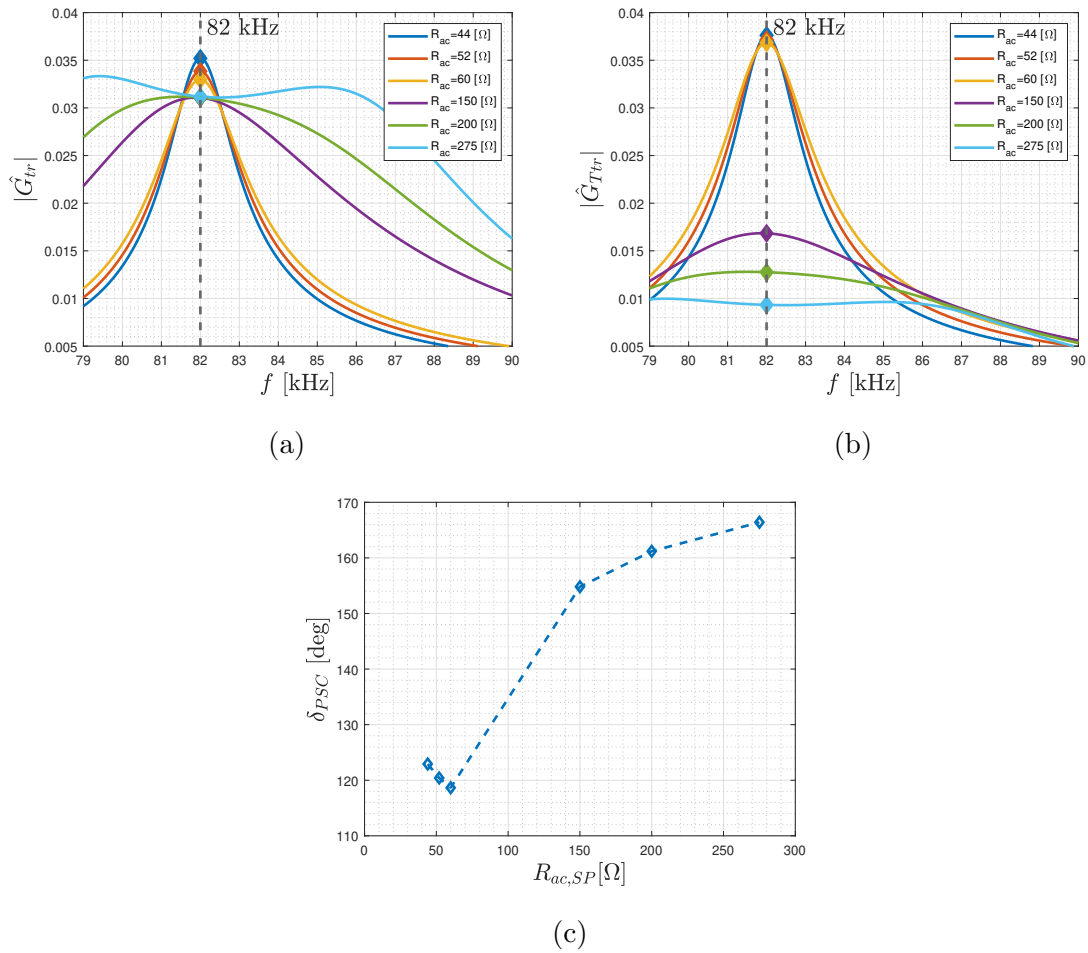


Figure 4.13: Selected operating point by the PSC control scheme for (a) transconductance gain, (b) total gain and finally (c) shows the delta values.

The hybrid phase-shift and frequency control (HPSFC) merges the benefits of FC and PSC. In order to successfully improve the performance, over the entire CC-CV charging cycle, of the above mentioned control techniques and to ensure the HPSFC to work in the optimum operating point, Fig. 4.15 illustrates the flowchart which includes point by point the steps, assumptions and calculations needed to maximize the efficiency. The entire procedure aims to create a map containing the couples f and δ suitable for ensuring maximum efficiency. Taking as an input the compensation topology, which is in this Section the S-P compensation, and the battery pack configuration of Tab. 3.3, the CC-CV profile is obtained. For congruence it is also shown in Fig. 4.10a. The equivalent resistance for S-P compensation is given in Tab. 3.4, whereas f_{min} and f_{max} are, as already said, the SAE J2954 limit

values, respectively 79-90 kHz. In order to map the entire working point region, the procedure that follows hereinafter is carried out for any load, frequency and phase-shift value. Starting from a given minimum equivalent load R_{ac}^* , the reference transconductance gain is found as:

$$G_{Tr}^{\hat{*}} = \frac{I_{batt}^*}{V_{dc}} \quad (4.8)$$

where I_{batt}^* is the reference battery current coming from Fig. 4.10a. Then, the frequency is set to a reference value f^* and the system parameters are reiterated at that frequency as:

$$\begin{aligned} \omega^* &= 2\pi f^* \\ R_1^* &= \frac{\omega^* L_1}{Q_1} \\ R_2^* &= \frac{\omega^* L_2}{Q_2} \\ \hat{Z}_1^* &= R_1^* + j \left(\omega^* L_1 - \frac{1}{\omega^* C_1} \right) \\ \hat{Z}_2^* &= R_2^* + j \left(\omega^* L_2 \right) \\ \hat{Z}_{ac}^* &= \frac{\pi^2}{8} R_{load} // \frac{1}{j\omega^* C_2}. \end{aligned} \quad (4.9)$$

Then, from Eq. 4.7 the value of δ can be derived as:

$$\delta = 2arccos \left(\frac{G_{Tr}^{\hat{*}} \pi}{|G_{Tr}^{\hat{*}}| 4} \right). \quad (4.10)$$

To guarantee ZVS operating condition for the primary inverter the angle of the resonant tank input impedance must be positive. After some simulations considering several iteration loops with positive and small resonant tank input impedance angles in the range 1° - 13° , a reasonable value is found to be 7° . Therefore, for any pair of f and δ the input impedance angle must be checked. In case of failure, the frequency must be increased of a quantity $\Delta_{f_{\varphi_{Zin}}}$. The last step before increasing the frequency is to calculate the total efficiency η_{tot} . According to Eq. 3.26, it can be obtained as the product of partial efficiencies:

$$\eta_{tot} = \eta_i \eta_{rt} \eta_{dr} \quad (4.11)$$

where η_i is the inverter efficiency calculated as:

$$\eta_i = \frac{\hat{V}_1 \hat{I}_1}{\hat{V}_1 Re[\hat{I}_1] + P_{cond}^{MOS} + P_{sw,off}^{MOS}}. \quad (4.12)$$

According to [82], the conduction losses P_{cond} on primary inverter can be calculated as:

$$P_{cond}^{MOS} = 4R_{ds,on} \hat{I}_{1,rms}^2 \quad (4.13)$$

considering the $R_{ds,on}$ the resistance value between the drain and source of a MOSFET during operation. Then, according to [83] and under the hypothesis of soft turn-on commutation, only the turn-off switching losses $P_{sw,off}^{MOS}$ are considered. Fig. 4.14 illustrates the turn-off process of switch S_1 . Assuming that the turn-off current i_{off1}

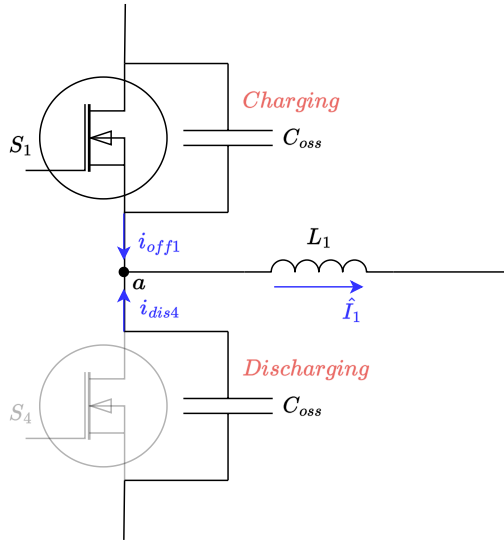


Figure 4.14: Turn-off process of MOSFET switch S_1 .

circulating on switch S_1 is linearly decreasing during turn-off, also the drain-source voltage v_{ds1} across S_1 will be linearly decreasing and the losses can be calculated through an integral during the turn-off time as:

$$\begin{aligned} P_{sw,off}^{S_1} &= \frac{1}{T_r} \int_{t_1}^{t_1+t_f} i_{off1}(t) v_{ds1}(t) dt \\ &= \frac{1}{T_r} \int_0^{t_f} [i_{off1}(t_1) - k_1 t] k_2 t dt \end{aligned} \quad (4.14)$$

where k_1 and k_2 are the slop of $i_{off1}(t)$ and $v_{ds1}(t)$, respectively obtained as:

$$\begin{aligned} k_1 &= \frac{i_{off1}}{t_f} \\ k_2 &= \frac{V_{dc}}{t_f}. \end{aligned} \quad (4.15)$$

Whereas as stated in [84, 85], the turn-off current of switch S_1 at t_1 is equal to the difference between the resonant current i_{r1} at t_1 and the discharging current i_{disc4} of output capacitance C_{oss} of switch S_4 :

$$\begin{aligned} i_{off1} &= i_{r1}(t_1) - i_{disc4} \\ &= i_{r1}(t_1) - C_{oss} \frac{V_{dc}}{t_f}. \end{aligned} \quad (4.16)$$

Finally, the ending turn-off time is found considering the gate resistance R_g , the gate-drain charge Q_{gd} and the Miller plateau voltage $V_{gs,miller}$ as:

$$t_f = \frac{R_g Q_{gd}}{V_{gs,miller}}. \quad (4.17)$$

The calculation of the total switching losses comes straightforward from the losses $P_{sw,off}^{S_1}$ calculated for the switch S_1 :

$$\begin{aligned} P_{sw,off}^{MOS} &= 4P_{sw,off}^{S_1} \\ &= 4 \left(\frac{1}{6} ||i_{r1}(t_1)| - C_{oss} \frac{V_{dc}}{t_f} | V_{dc} t_f f \right) \\ &= \frac{2}{3} ||i_{r1}(t_1)| - C_{oss} \frac{V_{dc}}{t_f} | V_{dc} t_f f. \end{aligned} \quad (4.18)$$

The second efficiency term is η_{rs} , which models the resonant tank efficiency, and is calculated according to Eq. 3.27.

The third term η_{dr} is the H-bridge diode rectifiers efficiency, obtained as:

$$\eta_{rs} = \frac{\hat{V}_2 \hat{I}_2}{V_{batt} Re[\hat{I}_{batt}] + P_{cond}^{Diodes} + P_{sw,off}^{Diodes}}. \quad (4.19)$$

Where P_{cond}^{Diodes} derived from the assumption of operating the converter at constant duty cycle D and considering the current ripple negligible, the average conduction losses are:

$$P_{cond}^{Diodes} = 4V_F I_F (1 - D) \quad (4.20)$$

where V_F and I_F are the diode forward voltage and forward current, respectively.

Indeed, the average switching losses of H-bridge diodes rectifiers are:

$$P_{sw,off}^{Diodes} = 4E_{RR} f \quad (4.21)$$

where E_{RR} is the energy loss per pulse, obtained as:

$$E_{RR} = \frac{V_{dc} I_{RRM}}{6} t_b \quad (4.22)$$

where I_{RRM} is the peak recovery current and t_b comes from:

$$t_b = t_{rr} - \frac{I_{RRM}}{\frac{di_F}{dt}} \quad (4.23)$$

being t_{rr} the reverse recovery time.

Until this point, the total efficiency is calculated for one point of the N couples of f and δ values indicated as (f_i, δ_i) pairs, returning $\eta_{tot}(f_i, \delta_i)$. The same procedure is carried out, increasing step by step the frequency as $f^* = f + \Delta f_f$ until $f^* = f_{max}$, obtaining the N couples of f and δ . The total efficiency is mapped for any (f_i, δ_i) pairs, giving the map $\eta_{tot}\forall(f_i, \delta_i)$. Finally, the total efficiency can be reiterated increasing the reference load resistance as $R_{ac}^* = R_{ac} + \Delta R_{ac}$ leading the map $\eta_{tot}\forall(f_i, \delta_i)$ to be calculated for any operating point: $\eta_{tot}\forall(f_i, \delta_i), \forall R_{ac,i}$. Taking $\eta_{tot,max}\forall(f_i, \delta_i), \forall R_{ac,i}$, for any operating condition, guarantees maximum efficiency. When the actual resistance matches the maximum equivalent resistance the algorithm stops.

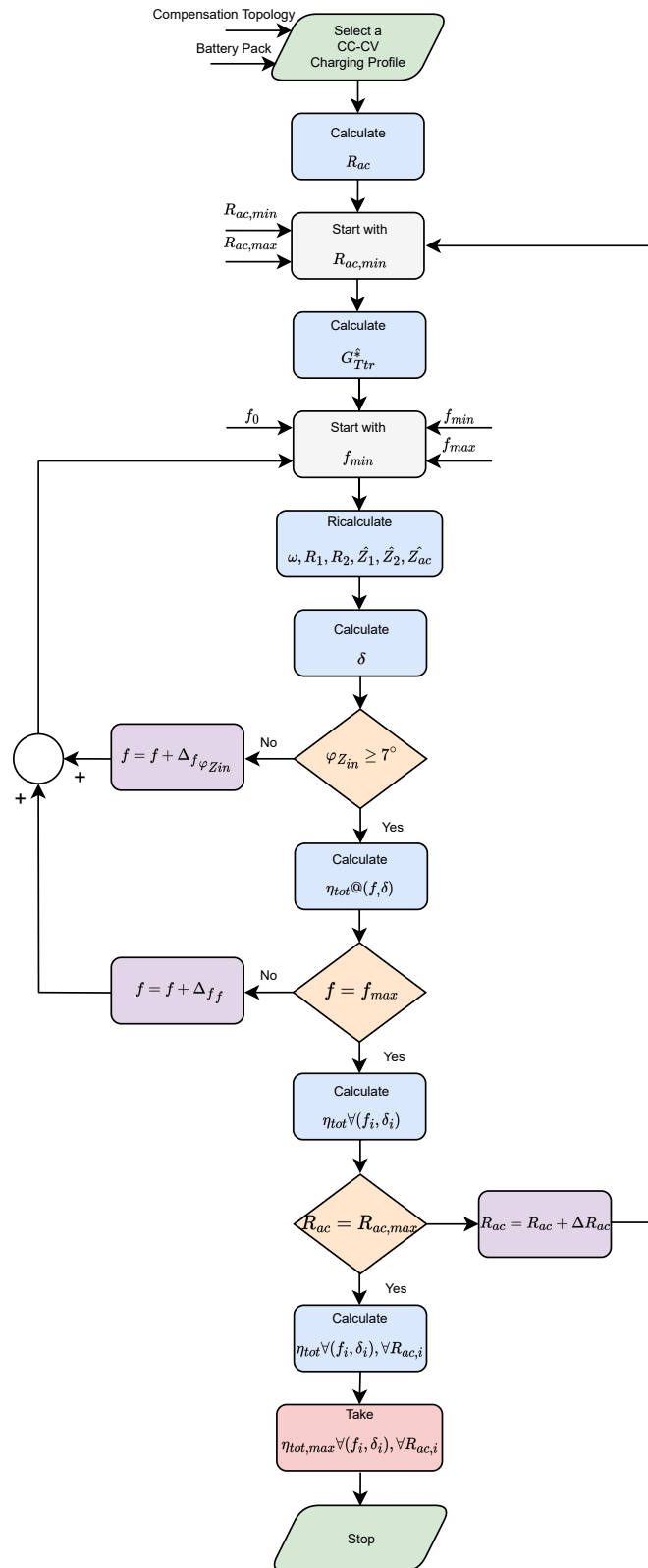


Figure 4.15: Hybrid phase-shift and frequency control flowchart for primary inverter control.

The algorithm outputs are the N pairs of hybrid f and δ control. Considering the efficiency calculated for any operating point as $\eta_{tot,max} \forall (f_i, \delta_i), \forall R_{ac,i}$, Fig. 4.16a shows the resulting, and optimized, frequency values as a function of the equivalent load resistance, while Fig. 4.16b reports the corresponding phase-shift values. What is noticeable is the very narrow frequency band. Thanks to the coordinated effect of f and δ has been possible to reduce the operating frequency close to resonance. This is a reasonable consideration since the efficiency, for the resonant tank, is maximized at resonance.

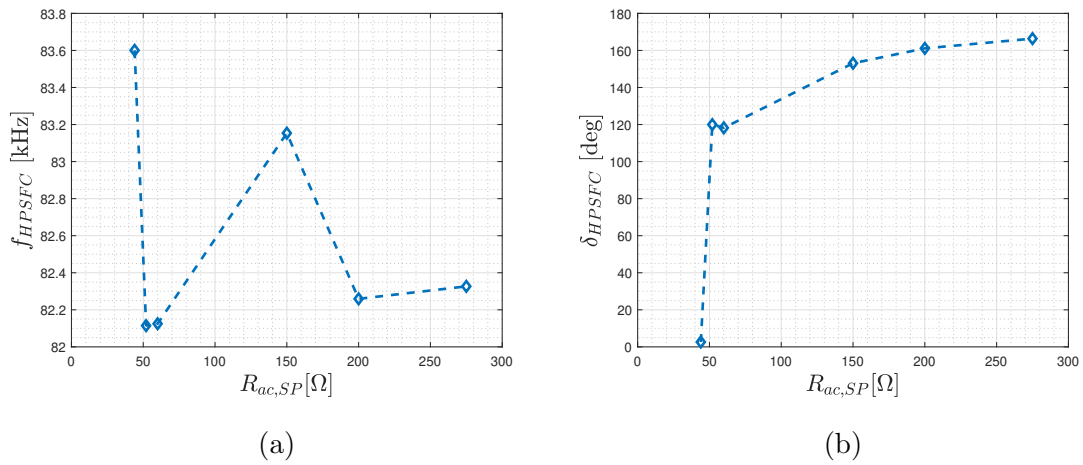


Figure 4.16: Hybrid control algorithm outputs showing, as a function of the load, (a) the frequency values and (b) the phase-shift values.

Additionally, since the choice of the phase-shift angle is subordinated to the operating frequency value, according to the flowchart procedure both variables can be represented in the same plot as a function of the equivalent load resistance, creating a MAP, as shown in Fig. 4.17a for the 2D representation and in Fig. 4.17b for the 3D representation.

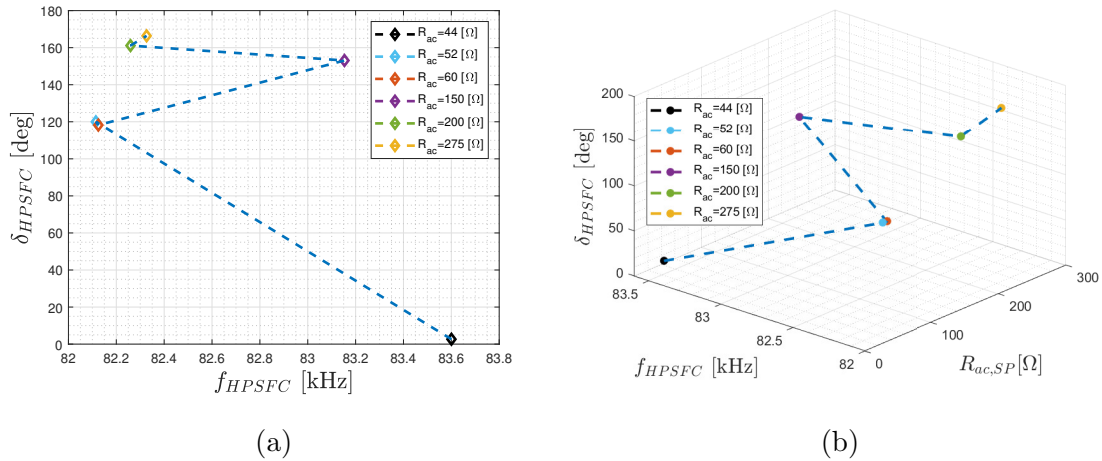


Figure 4.17: Hybrid control algorithm outputs showing (a) the resulting frequency phase-shift 2D map and (b) 3D representation of the frequency and phase-shift map for the N pairs for any operating point.

4.3.2 S-S Compensation

Similar considerations to S-P compensation can also be carried out for S-S compensation. In the following, according to Fig. 4.9 for FC and to Fig. 4.12 for PSC, the control techniques are analyzed when applied to a resonant tank series compensated. Starting with FC, the reference signals, $V_{batt,ref}$ and $I_{batt,ref}$ are exactly the same, since they all belong to the same battery pack. Moreover the anti-windup limits of the two PI regulators, I_{CC} and $(f_{max} - f_{min})$, are set according to S-P compensation. The only difference is found in the equivalent load seen at the output terminals of the resonant tank, which for S-S compensation is in the range $R_{ac,SS} = 28\Omega - 200\Omega$. The module of the primary voltage applied to the resonant tank is again equal to 509V. To select the appropriate frequency values to be applied to the primary switches, the control schemes rely on the transconductance gain. As already done for S-P compensation, Fig. 4.18a recalls the sampled battery resistance, whereas the optimum operating points needed to match the reference battery current. Therefore the reference battery voltage is chosen according to the input voltage through the transconductance gain of Fig. 4.18b. The resulting frequency values are given in Fig. 4.18c.

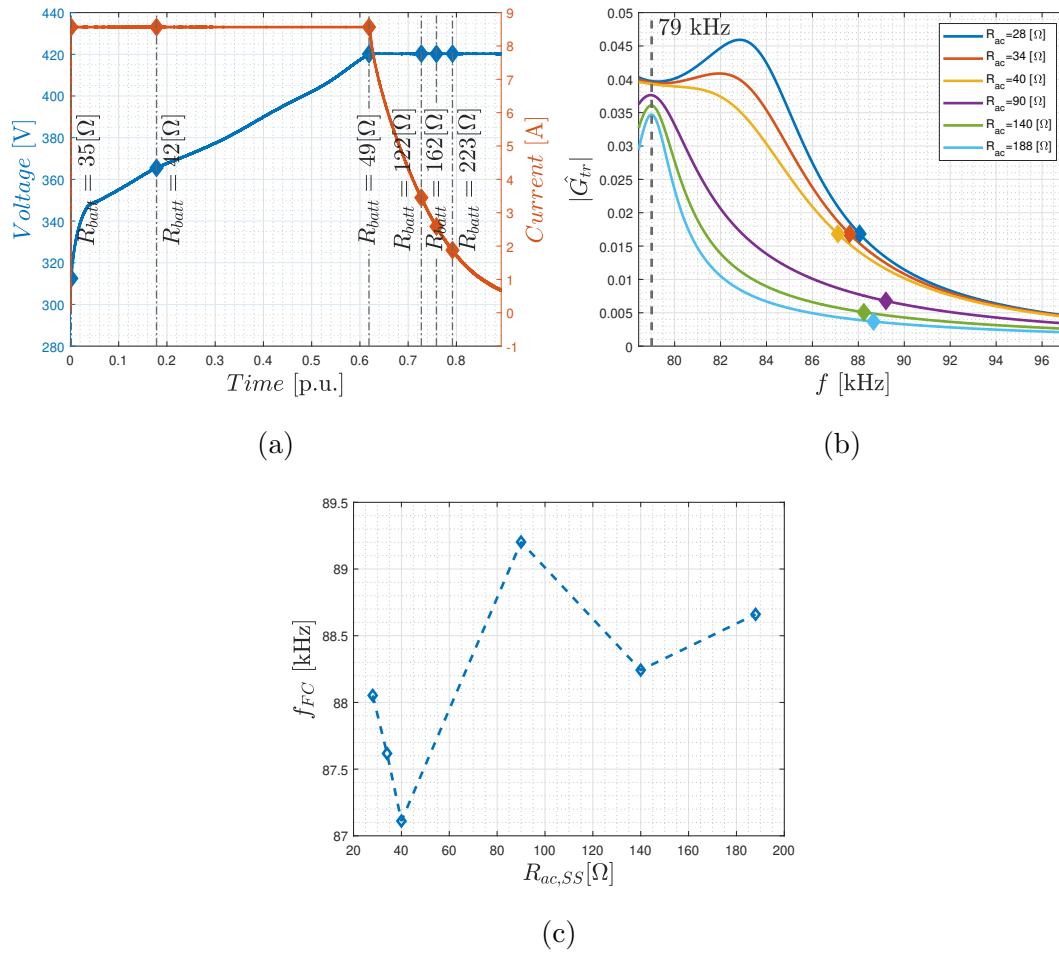


Figure 4.18: (a) Sampled battery voltage and battery current operating points at reference coupling coefficient k_0 . (b) Optimum transconductance gain to match the reference battery current and the input voltage. (c) Operating frequency in S-S compensation under FC, for controlling the battery current.

Differently from S-P compensation, here the transconductance gain presents the operating points close to $\hat{G}_{tr} = 0.17$ for the three smallest loads and $\hat{G}_{tr} = 0.005$ for the three biggest loads, returning a frequency at about 88 kHz for all the working points. Differently from S-P compensation, the FC for S-S compensation fulfil the SAE J2954 frequency range.

For what concerns PSC, as for the FC control, both the reference signals and the anti-windup limits are the same shown in Fig. 4.12 for S-P compensation. Aside from the equivalent load, the first difference with respect to S-P compensation is found

in Eq. 4.7, where \hat{G}_{tr} of course refers to this compensation topology. The resulting total gain, from input voltage \hat{V}_1 to output current I_{batt} is shown in Fig. 4.19 for several δ values, at a reference coupling coefficient. Each figure refers to a different equivalent load.

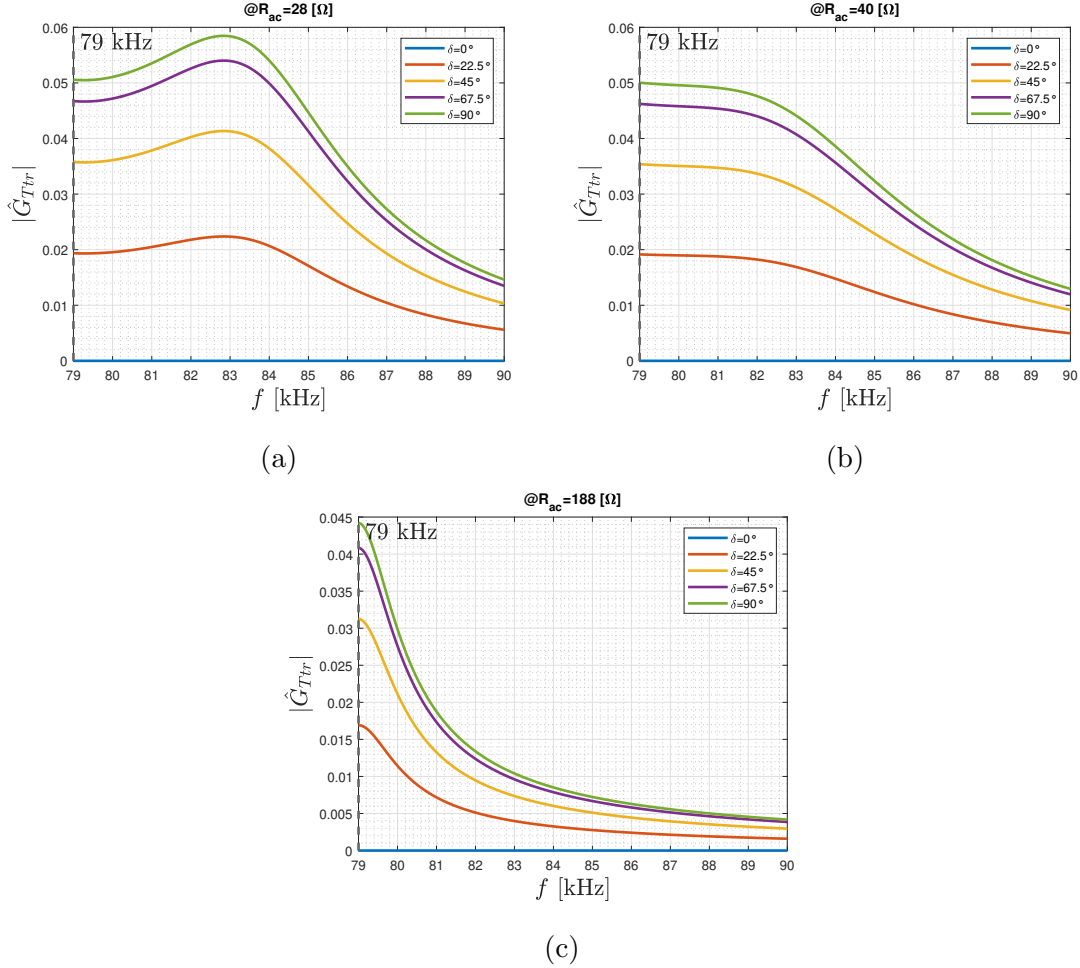


Figure 4.19: Total gain \hat{G}_{Ttr} for different phase-shift values and for S-S compensation, calculated at reference coupling coefficient k_0 . Three different equivalent loads are considered: (a) $R_{ac,min}$, (b) $R_{ac}@P_{max}$, (c) $R_{ac,max}$.

The total gain \hat{G}_{Ttr} , from the DC bus up to the battery current comes from the transconductance gain. With both \hat{G}_{tr} and \hat{G}_{Ttr} it is possible to find the δ values, Fig. 4.20.

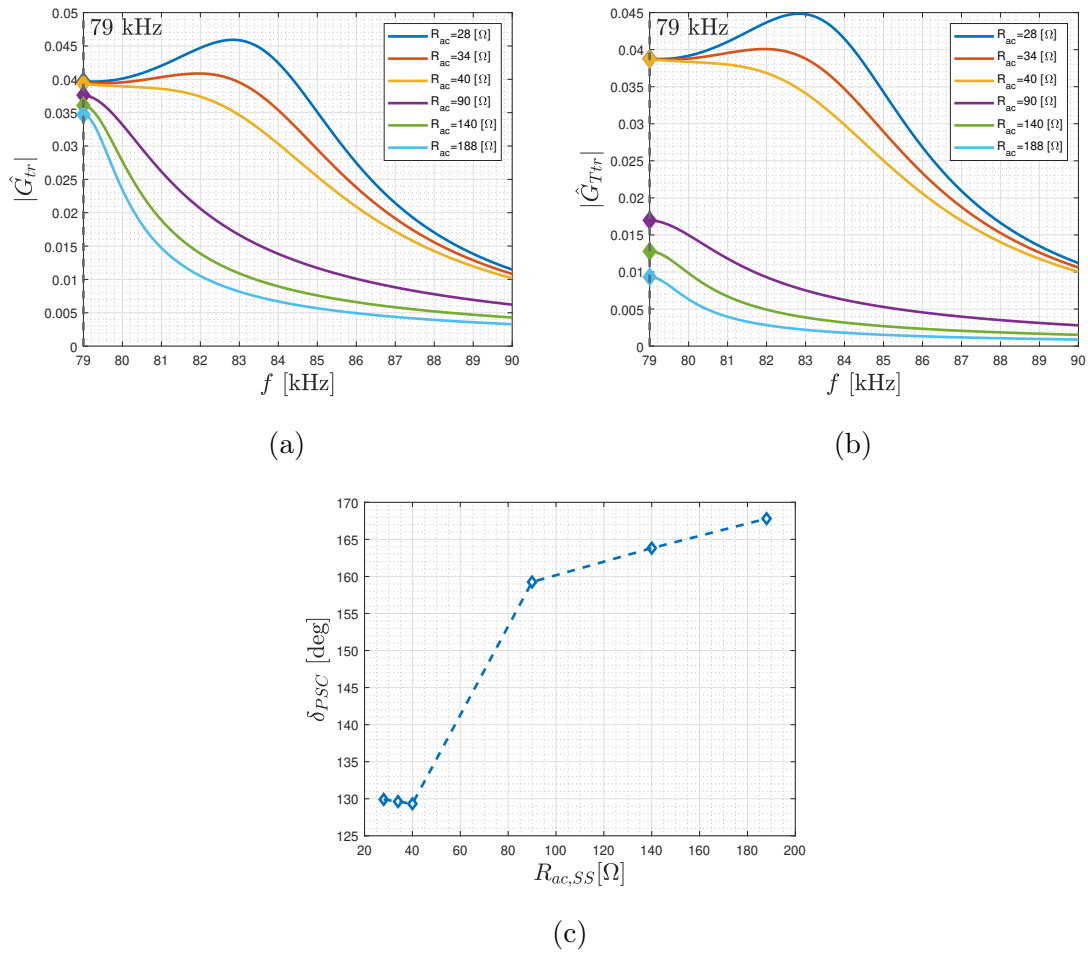


Figure 4.20: Selected operating point by the PSC control scheme for (a) transconductance gain, (b) total gain and finally (c) shows the delta values for S-S compensation.

The proposed HPSFC follows the same flowchart of Fig. 4.15. The procedure is valid for both compensation topologies, what changes are obviously the equations specific for each compensation and the associated voltage gain and transconductance gain. Substituting Eq. 4.9 with the following one the algorithm can be applied without any concern.

$$\begin{aligned}
 \omega^* &= 2\pi f^* \\
 R_1^* &= \frac{\omega^* L_1}{Q_1} \\
 R_2^* &= \frac{\omega^* L_2}{Q_2} \\
 \hat{Z}_1^* &= R_1^* + j \left(\omega^* L_1 - \frac{1}{\omega^* C_1} \right) \\
 \hat{Z}_2^* &= R_2^* + j \left(\omega^* L_2 - \frac{1}{\omega^* C_2} \right) \\
 \hat{Z}_{ac}^* &= \frac{8}{\pi^2} R_{load}.
 \end{aligned} \tag{4.24}$$

The N pairs of $(f_i \delta_i)$ which maximize the efficiency are plotted below as a function of the equivalent load resistance.

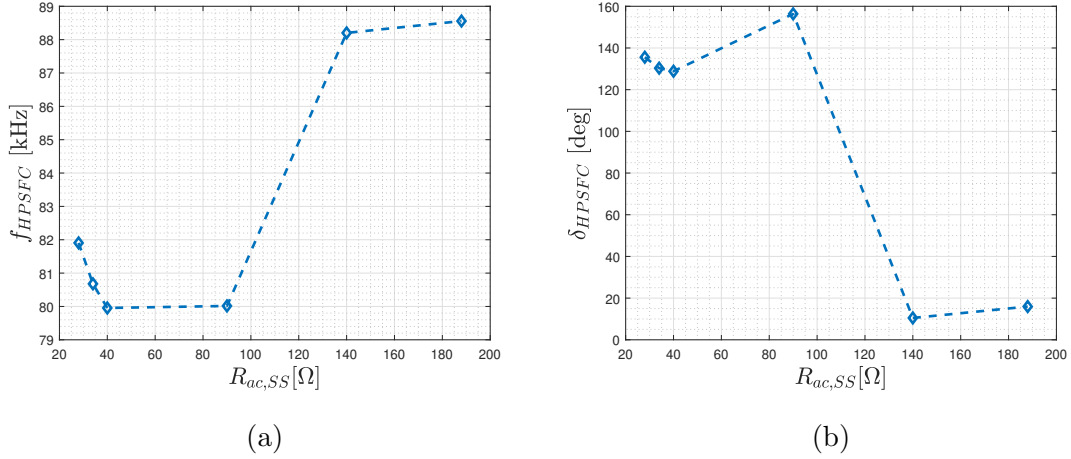


Figure 4.21: Hybrid control algorithm outputs showing, as a function of the load, (a) the frequency values and (b) the phase-shift values for S-S compensation.

Both variable can also be mapped in 2D and 3D, as illustrated in Fig. 4.22 and as previously done for S-P compensation.

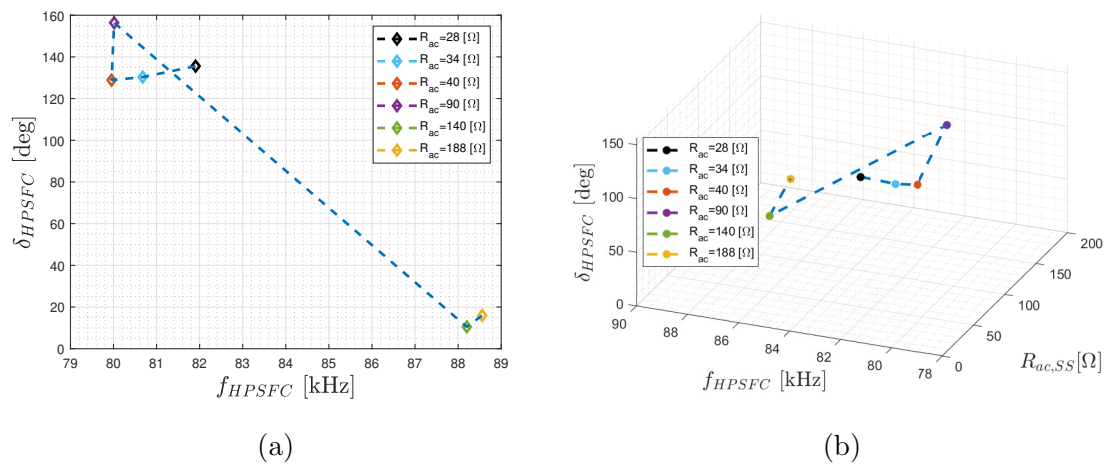


Figure 4.22: Hybrid control algorithm outputs showing (a) the resulting frequency phase-shift 2D map and (b) 3D representation of the frequency and phase-shift map for the N pairs for any operating point for S-S compensation.

Chapter 5

Results and Discussion

Within this Chapter the main results obtained from Chapter 3 and Chapter 4 are presented and discussed. Hereinafter, three main sections represent the core of this part. Starting from the resonant tank design outcomes, main results in terms of parameters variation and efficiency evaluation are given for both S-P compensation topology and S-S compensation topology. Then, the second main section highlights the benefits of hybrid phase-shift and frequency control when benchmarked with traditional frequency control and phase-shift control, for both compensations. The last part of the Chapter presents a system overview, merging the resonant tank design along with power electronics control showing results, benchmark and comparison. Lastly, an energy assessment of the three control methods, evaluated for both compensation topologies, in consideration of the powers and their period of permanence in any working point is presented at the end of this section. The tests shown have all been carried out in the Matlab/Simulink environment exposed in the previous chapters, adopting the discrete time modelling to take into account the performance of the control platform. This testing environment has been proven an effective way to verify the algorithm performance under many aspects by the experience of the LEMAD. However, experimental validation is always needed at least as a final step to work out specific issues, especially regarding signals noise and hardware non-ideality. For the purposes of this work, the experimental test bench validation are carried out by the collaborating Delft University of Technology (TU Delft). The data is therefore not presented in this thesis, but they are crucial

first and foremost to push an efficient implementation and, secondly, to validate the algorithm outputs, verifying also the simulation environment.

5.1 Resonant Tank Outcomes

5.1.1 S-P Compensation

Similarly to the sensitivity analysis carried out in Subsection 3.3.1 for the voltage gain, transconductance gain, input module and phase angle of the impedance seen at the input side of the resonant tank, the first important result to be shown refers to illustrate how the design procedure outputs, which are the resonant tank parameters $L_{1_{opt}}$, $L_{2_{opt}}$, $C_{1_{opt}}$ and $C_{2_{opt}}$ vary according to the choice of reference parameters k_0 , R_0 and f_0 . In fact, from the formulas obtained in Subsection 3.3.1, it is possible to define how each parameter behaves when changing a specific reference value, as listed in Tab. 5.1.

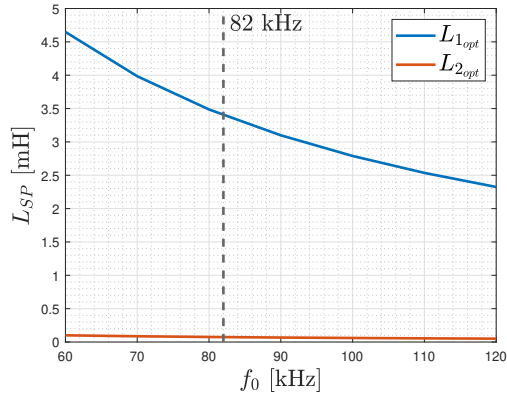
Table 5.1: S-P compensated resonant tank dependency to reference parameters.

<i>Parameter</i>	<i>Exact Formula</i>	<i>Dependency</i>		
		k_0	f_0	$R_{ac,0}$
$C_{2_{opt}}$	Eq. 3.36	$\propto \frac{1}{\sqrt{1+k_0^2}}$	$\propto \frac{1}{f_0}$	$\propto \frac{1}{R_{ac,0}}$
$L_{2_{opt}}$	Eq. 3.39	$\propto \sqrt{1+k_0^2}$	$\propto \frac{1}{f_0}$	$\propto R_{ac,0}$
$L_{1_{opt}}$	Eq. 3.42	$\propto L_{2_{opt}} \left(\frac{1}{k_0}\right)^2$	$\propto L_{2_{opt}}$	$\propto L_{2_{opt}}$
$C_{1_{opt}}$	Eq. 3.43	$\propto \frac{1}{L_{1_{opt}}(1-k_0^2)}$	$\propto \frac{1}{L_{1_{opt}}f_0^2}$	$\propto \frac{1}{L_{1_{opt}}}$

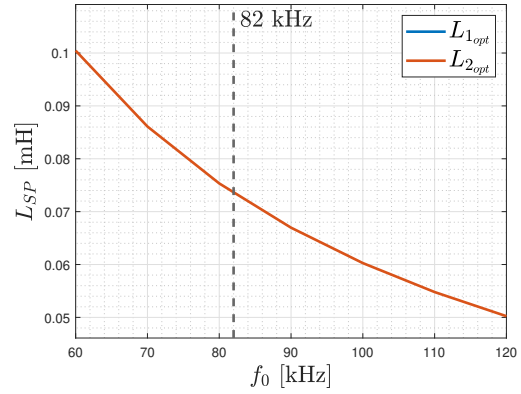
The resulting graphs from the dependency variation of the above mentioned Table are shown in Fig. 5.1 for the four parameters. The figures on the left-hand side, namely Fig. 5.1a, Fig. 5.1c, Fig. 5.1e contain, on the same y-axis both couple $L_{1_{opt}}$ and $L_{2_{opt}}$, while on the right-hand side of Fig. 5.1b, Fig. 5.1d, Fig. 5.1 since the value of $L_{2_{opt}}$ is significantly lower than $L_{1_{opt}}$ its trend is illustrated. As it is

noticeable, all trends confirm the behavior previously predicted.

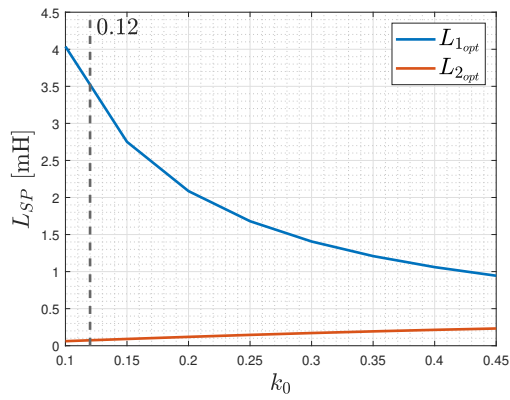
In Fig. 5.2 the analysis is carried out for the optimum primary and secondary capacitance values.



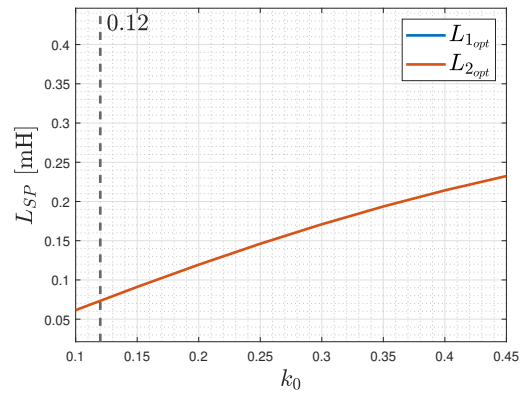
(a)



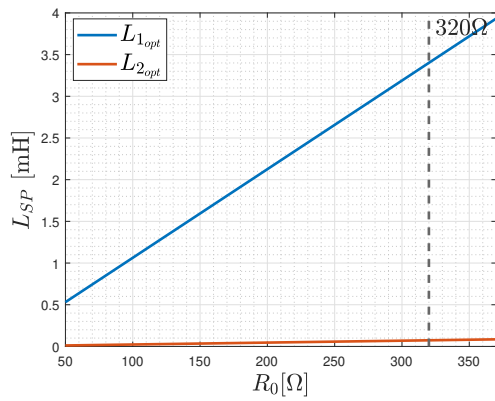
(b)



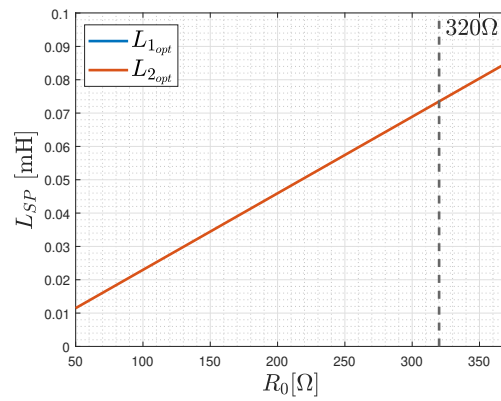
(c)



(d)



(e)



(f)

Figure 5.1: Resonant tank optimum primary and secondary inductance variation, according to reference parameters for S-P compensation. Figures (a), (c), (e) show both parameters, while figures (b), (d), (f) zoom the secondary inductance variation.

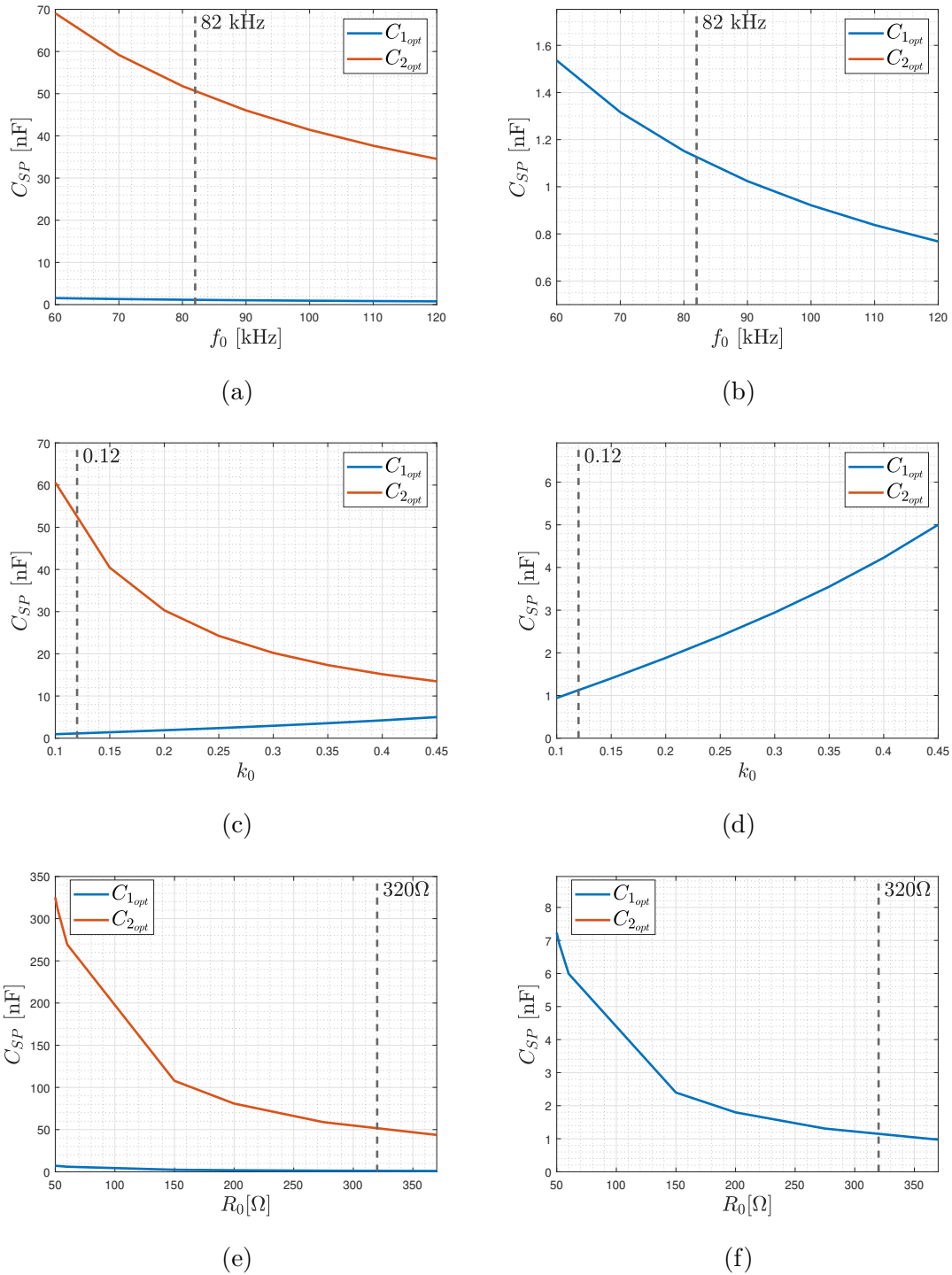


Figure 5.2: Resonant tank optimum primary and secondary capacitance variation, according to reference parameters for S-P compensation. Figures (a), (c), (e) show both parameters, while figures (b), (d), (f) zoom the primary capacitance variation.

What is missing until now for S-P compensation is the efficiency evaluation as a function of the frequency, for different loads and for different coupling coefficients. Fig. 5.3a shows the efficiency, for different loads, in a wide frequency range that can be useful also for different applications, while Fig. 5.3b zooms the efficiency in a SAE J2954 frequency range, according to the target application. Fig. 5.3c and Fig. 5.3d illustrate the same concept but for different coupling coefficients. As it is noticeable, in both cases the efficiency is maximized at resonance. Even if the system has been designed for a reference load of 320Ω , the maximum efficiency for all loads, does not correspond to that value. In fact, it is evident that for smaller loads, such as 150Ω and 200Ω the efficiency peaks at higher value. This is due to the fact that the system is not designed for having the maximum overall efficiency at reference load, but for having the maximum possible efficiency at that load. It means that it may be possible to have combinations of loads and parameters that exceed that efficiency value. Indeed, what the coupling coefficients variation reports is the fact that, as predicted, as the coupling coefficient increases the efficiency increases. This is due to the fact that as k increases the leakage flux of the resonant tank decreases, leading to concatenate more and to have lower losses.

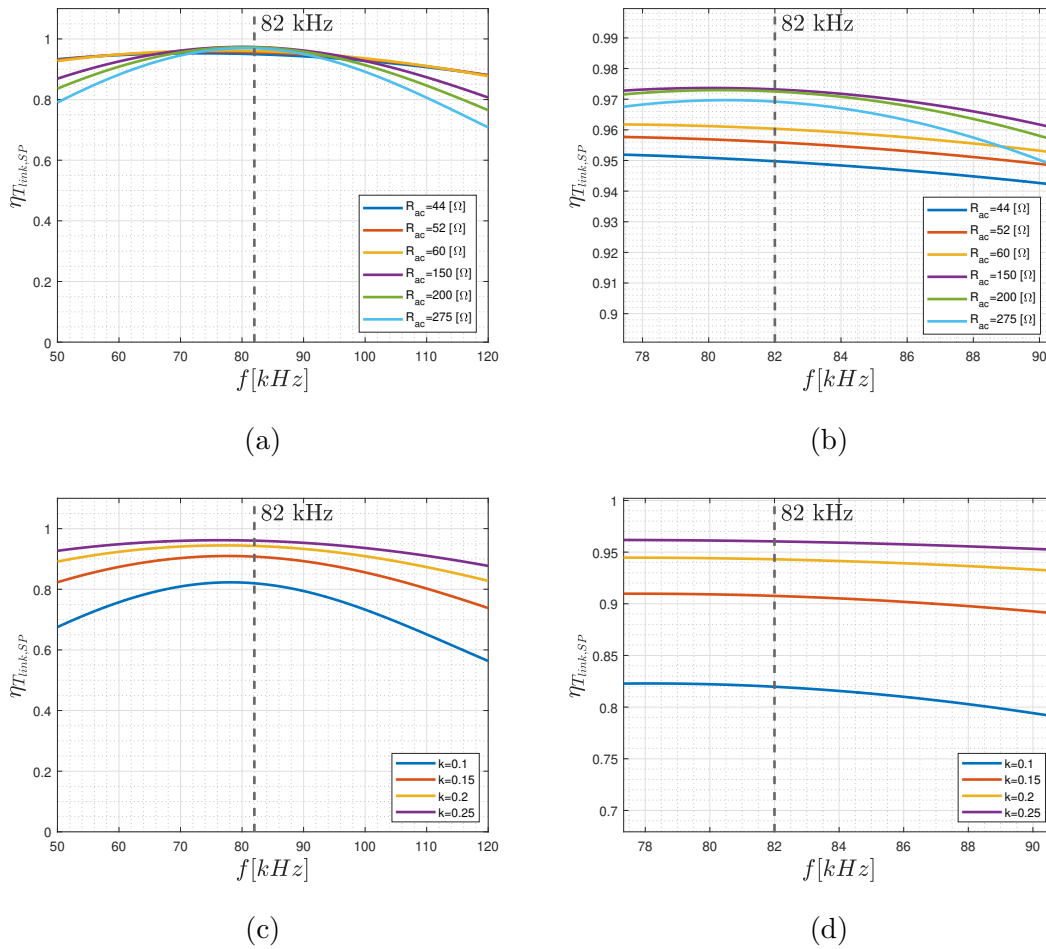


Figure 5.3: Efficiency evaluation for S-P compensation as a function of the frequency for (a) different loads in a wide frequency range, (b) different loads in the SAE J2954 range, (c) different coupling coefficients in a wide frequency range and (d) different coupling coefficients in the SAE J2954 range.

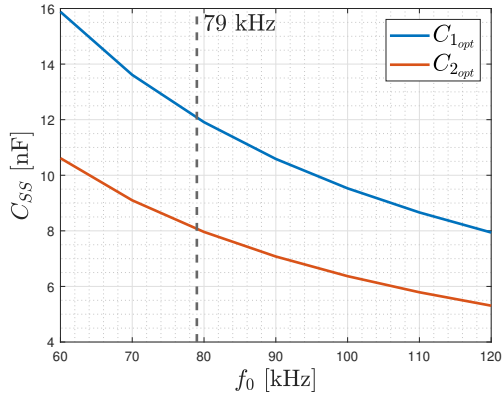
5.1.2 S-S Compensation

The same evaluation of the previous Subsection can also be carried out for S-S compensation. As for S-P compensation, the resonant tank dependency to resonant parameters is listed in Tab. 5.2.

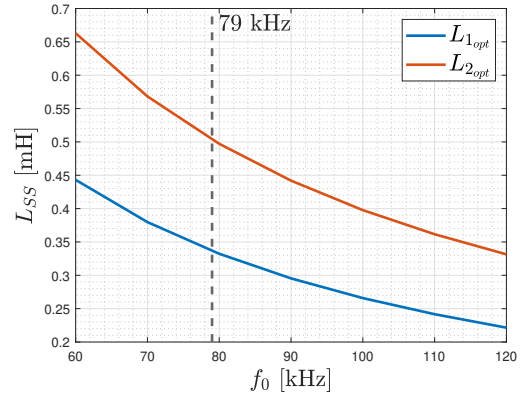
Table 5.2: S-S compensated resonant tank dependency to reference parameters.

<i>Parameter</i>	<i>Exact Formula</i>	<i>Dependency</i>		
		k_0	f_0	$R_{ac,0}$
$C_{2_{opt}}$	Eq. 3.47	$\propto \sqrt{1 + k_0^2}$	$\propto \frac{1}{f_0}$	$\propto \frac{1}{R_{ac,0}}$
$L_{2_{opt}}$	Eq. 3.48	$\propto \frac{1}{\sqrt{1 + k_0^2}}$	$\propto \frac{1}{f_0}$	$\propto R_{ac,0}$
$L_{1_{opt}}$	Eq. 3.50	$\propto L_{2_{opt}} \left(\frac{1}{k_0} \right)^2$	$\propto L_{2_{opt}}$	$\propto L_{2_{opt}}$
$C_{1_{opt}}$	Eq. 3.52	$\propto \frac{1}{L_{1_{opt}}}$	$\propto \frac{1}{L_{1_{opt}} f_0^2}$	$\propto \frac{1}{L_{1_{opt}}}$

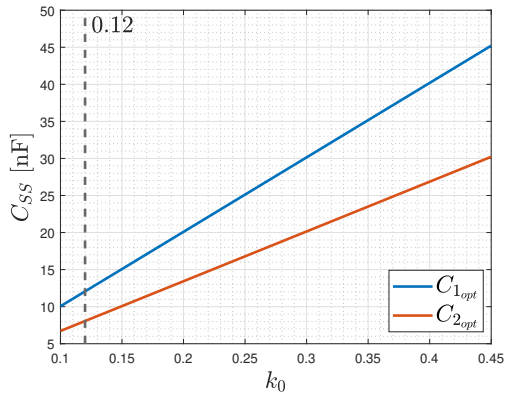
What comes out comparing the S-P and S-S dependency table is the fact that although for the reference frequency and for the reference load there is no differences between the two compensations, for the reference coupling coefficient the dependency of $C_{2_{opt}}$ and $L_{2_{opt}}$ is switched. The results are plotted in Fig. 5.4. Unlike S-P compensation, here primary self-inductance and secondary self-inductance have the same order of magnitude as well as primary compensation capacitor and secondary compensation capacitor are comparable to each other.



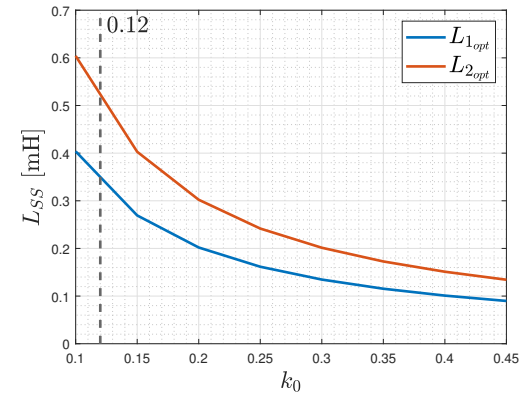
(a)



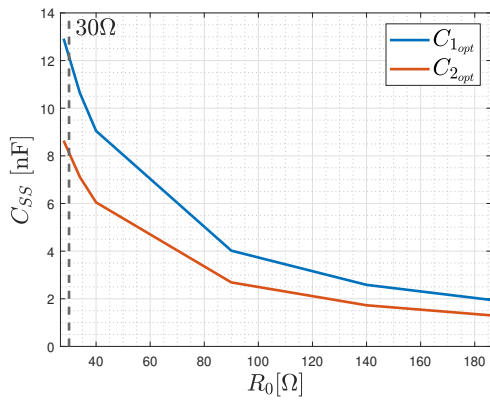
(b)



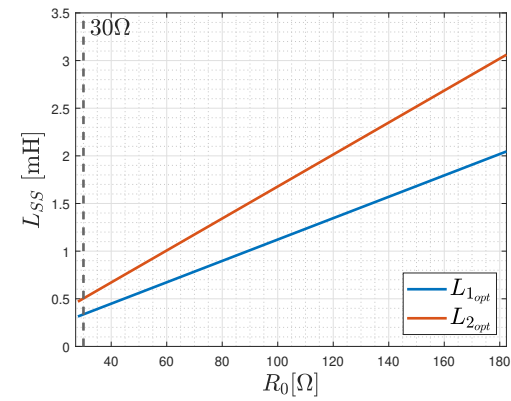
(c)



(d)



(e)



(f)

Figure 5.4: Resonant tank optimum primary and secondary side inductances and capacitances variation, for S-S compensation, as a function of (a) and (b) reference frequency, (c) and (d) reference coupling coefficient, (e) and (f) reference load.

As it was for S-P compensation, the efficiency is maximized at resonance. However, with S-P compensation there is a little difference when comparing small loads and big loads of Fig. 5.5d. In fact, since the system is designed for a reference load of 30Ω , the efficiency peaks at resonance, for small loads. While for big loads, from 140Ω to above the efficiency is higher than small loads for a wider frequency range as shown in Fig. 5.5a, but the peak appears at higher frequency. Indeed, for what concerns the behavior regarding the coupling coefficient variation it is confirmed that as it increases, the efficiency increases.

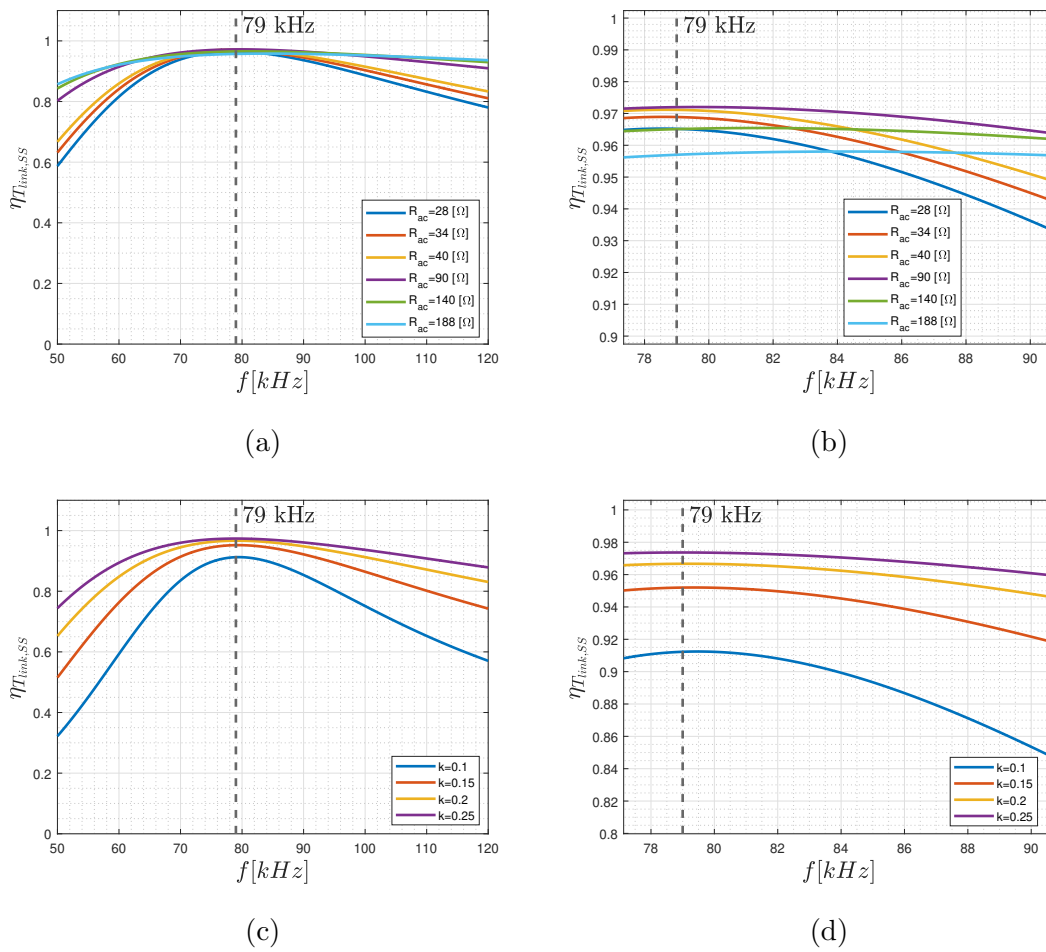


Figure 5.5: Efficiency evaluation for S-S compensation as a function of the frequency for (a) different loads in a wide frequency range, (b) different loads in the SAE J2954 range, (c) different coupling coefficients in a wide frequency range and (d) different coupling coefficients in the SAE J2954 range.

5.2 Power Electronics Control Outcomes

This subsection is an extension of Subsection 4.3 and provides additional results as well as efficiency evaluation and comparison among FC, PSC, HPSFC. For efficiency evaluation purpose, the components mounted on the experimental prototype realized by the collaborating Delft University of Technology (TU Delft) shown in Tab. 5.3 are considered. The table includes all the values of the experimental set-up, including part numbers and details of each component mounted on the resonant tank and in the power electronics mother board.

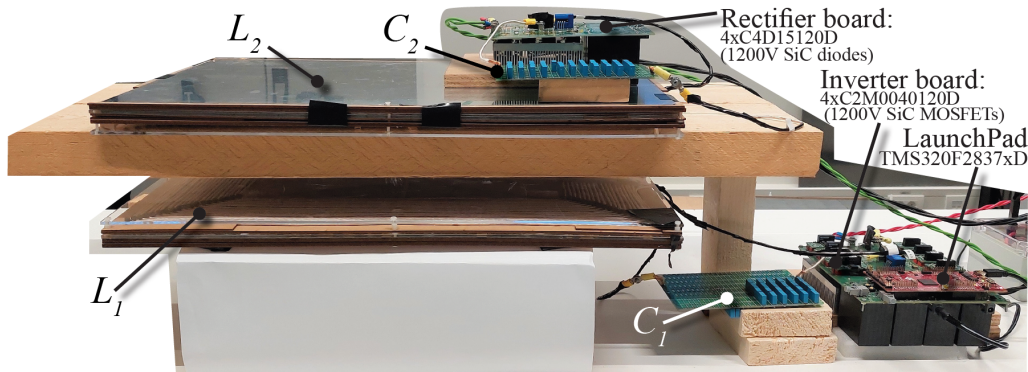
Table 5.3: Components mounted on the experimental set-up.

<i>Components</i>	<i>Function</i>	<i>Manufacturer</i>	<i>Part Number</i>
1200V SiC Mosfet	Inverter	Wolfspeed	C2M0040120D
1200V SiC Diode	Rectifier	Wolfspeed	C4D15120D
6.8 nF 500V _{rms}	Capacitor	EPCOS	B32671L
C2000 Delfino	DSP	Texas Instruments	LaunchPad TMS320F2837xD

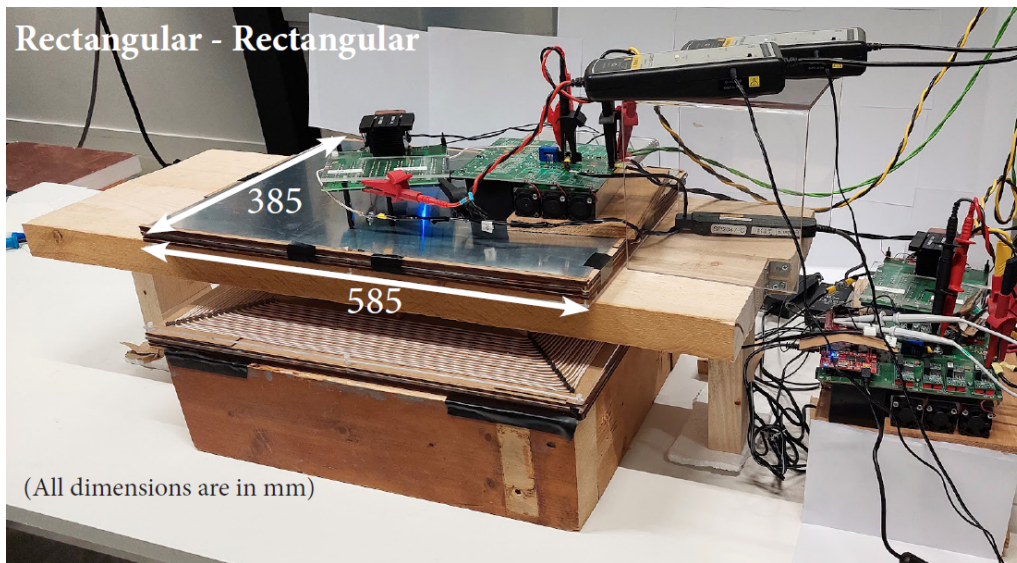
<i>Quantity</i>	<i>Symbol</i>	<i>Value</i>
Mosfet drain-source resistance	R_{DS}	50 m Ω
Mosfet output capacitance	C_{ossl}	171 pF
Mosfet gate-drain charge	Q_{gd}	42 nC
Mosfet miller plateau voltage	$V_{gs,miller}$	10 V
Diode maximum forward current	I_F	4.5 A
Diode maximum forward voltage	V_F	1.3 V
Diode peak recovery current	I_{RRM}	0 A
Diode reverse recovery time	t_{rr}	0 s

According to Tab. 5.3, the system prototype of WPT coupling coils, along with compensation capacitors, are shown in Fig. 5.6. The transmitting and receiving pads are in the rectangular-rectangular configuration and they are sized for a peak

power of 3.7 kW, according to SAE J2954 WPT1 class. The values of L_1 and L_2 are matched to the ones obtained in Chapter 3 and they change according to the compensation topology. Primary compensation capacitor and secondary compensation capacitor is obtained by a $N \times M$ combination of the EPCOS capacitors shown in the previous table, where N is the number of EPCOS in series and M in parallel. To avoid parasitic effects they are placed as close as possible to the coil terminals.



(a)



(b)

Figure 5.6: Experimental prototype realized by Delft University of Technology. Transmitting and receiving coils are shown in (a) front view, while (b) shows a different angulation and includes pad dimensions.

The power electronics devices, the primary inverter and secondary H-bridge diodes rectifier are shown in Fig. 5.7a and Fig. 5.7b, respectively. While secondary

H-bridge diode rectifiers are passive device and their turn-on / turn-off only depends on the circuit condition, the primary inverter needs to be controlled by a high speed DSP. For the purpose, a C2000 Delfino DSP has been selected to match the required performance and its characteristics are listed in Tab. 5.4. The output pins of the LaunchPad TMS320F2837xD coincide with the input pins of the inverter motherboard, so that of it results in a "plug and play" configuration and it can be mounted on the inverter motherboard directly.



Figure 5.7: Experimental prototype realized by Delft University of Technology. (a) Primary inverter and LaunchPad while (b) H-bridge diodes rectifiers.

Table 5.4: C2000 Delfino DSP characteristics.

CPU	2x C28x, 2x CLA
Frequency [MHz]	200
Flash memory [KB]	1024
RAM [KB]	204
DC resolution	12-bit, 16-bit
Total processing [MIPS]	800
Features	Configurable logic block, FPU32
UART	4
CAN [Ch]	2
PWM [Ch]	24
Sigma-delta filter	8
TI functional safety category	Functional Safety-Compliant

As already stated in Abstract and in the preamble of this chapter, on behalf of the collaboration between LEMAD - University of Bologna and Delft University of Technology (TU Delft), experimental results will not be discussed in this thesis.

5.2.1 S-P Compensation

Starting from the algorithm output shown in Chapter 4, which include the selected:

- Frequency points for FC
- Phase-shift points for PSC
- Frequency and phase-shift points for HPSFC.

The first interesting outcome takes as a benchmark the FC and the PSC and compares them with the proposed control. The comparison is shown in Fig. 5.8a for the FC and in Fig. 5.8b for the PSC. It is worth notice that the algorithm starts, at very low load, such as $R_{ac} = 44\Omega$, controlling only the frequency and keeping the

phase-shift equal to 0. Whereas, as the load increases the HPSFC basically follow the shape of the PSC. As it is reasonable to know, at least for S-P compensation, the algorithm tries to work at resonance, or close to it, and adjust the phase-shift value to match the required reference value, which in this case is the battery current. In fact, excluding the test point number one, in which there is no need to phase-shift the inverter legs, for all the other the frequency is few kHz greater than resonance (for ensuring ZVS on primary inverter) and the modulation of the transconductance gain occurs through phase-shift. It is also important to highlight that, although the HPSFC follows the shape of the PSC, it does not overlap any of those.

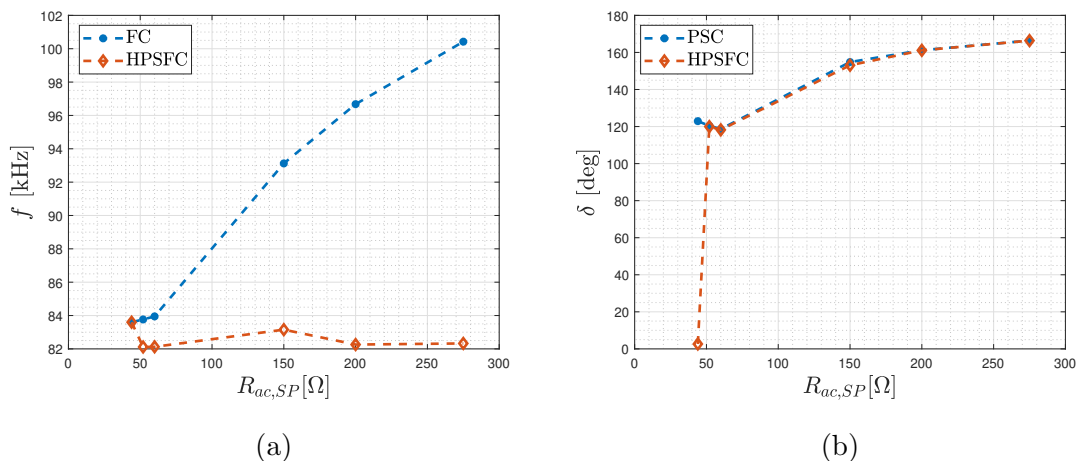


Figure 5.8: The resulting frequency and phase-shift value of the HPSFC are benchmarked with (a) FC and (b) PSC for S-P compensation.

The bench test to prove the effectiveness of the proposed control technique is the efficiency comparison. In fact, under FC the shape of the transconductance gain of Fig. 4.10b imposes the operating point to work at many kHz more than resonance, leading the control system to decrease the efficiency. In fact, always from that graph it is noticeable that as the load increases the frequency increases and, consequently, the efficiency decreases. The most critical points for FC are of course the ones in the CV mode, since the equivalent load resistance is bigger. Quite a different situation for PSC. The efficiency starts at 75% and increases up to the peak, at about 88%. Contrary to FC, the CC mode does not correspond to the most critical one for PSC. In fact, this type of control performs better at big loads with respect to small loads.

Finally, HPSFC tanks to the modulation of both frequency and phase-shift is able to overlap for about 1% the best performance obtained by PSC.

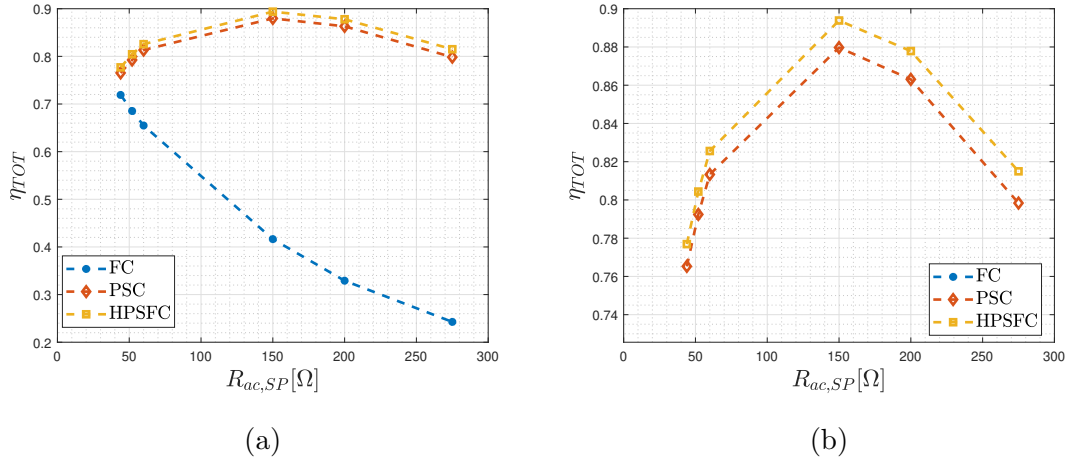


Figure 5.9: (a) Efficiency of the proposed HPSFC compared with stand-alone FC and PSC, while (b) highlights the improvement between HPSFC and PSC.

The efficiency of HPSFC is also mapped in 3D, as a function of the frequency, and therefore to the phase-shift, and to the equivalent load resistance. According to Fig. 5.10a, the efficiency of S-P compensation:

- For small loads, as the frequency increases the efficiency increases up to resonance, then it starts to decrease again.
- For big loads, the efficiency, as a function of the frequency, behaves similarly to the previous point. However, the Δf is lower, leading to have higher efficiency at resonance and higher at the frequency boundaries, Fig. 5.10b.
- At resonance, or close to resonance in the inductive region, the frequency increases as the load increases, as it is for PSC. While as the frequency reaches the boundaries, the trend is reversed. This leads to the consideration that if for some reasons the control system that is forced to work at high frequency, the efficiency is higher for small loads. This is the case of FC, Fig. 5.10c.

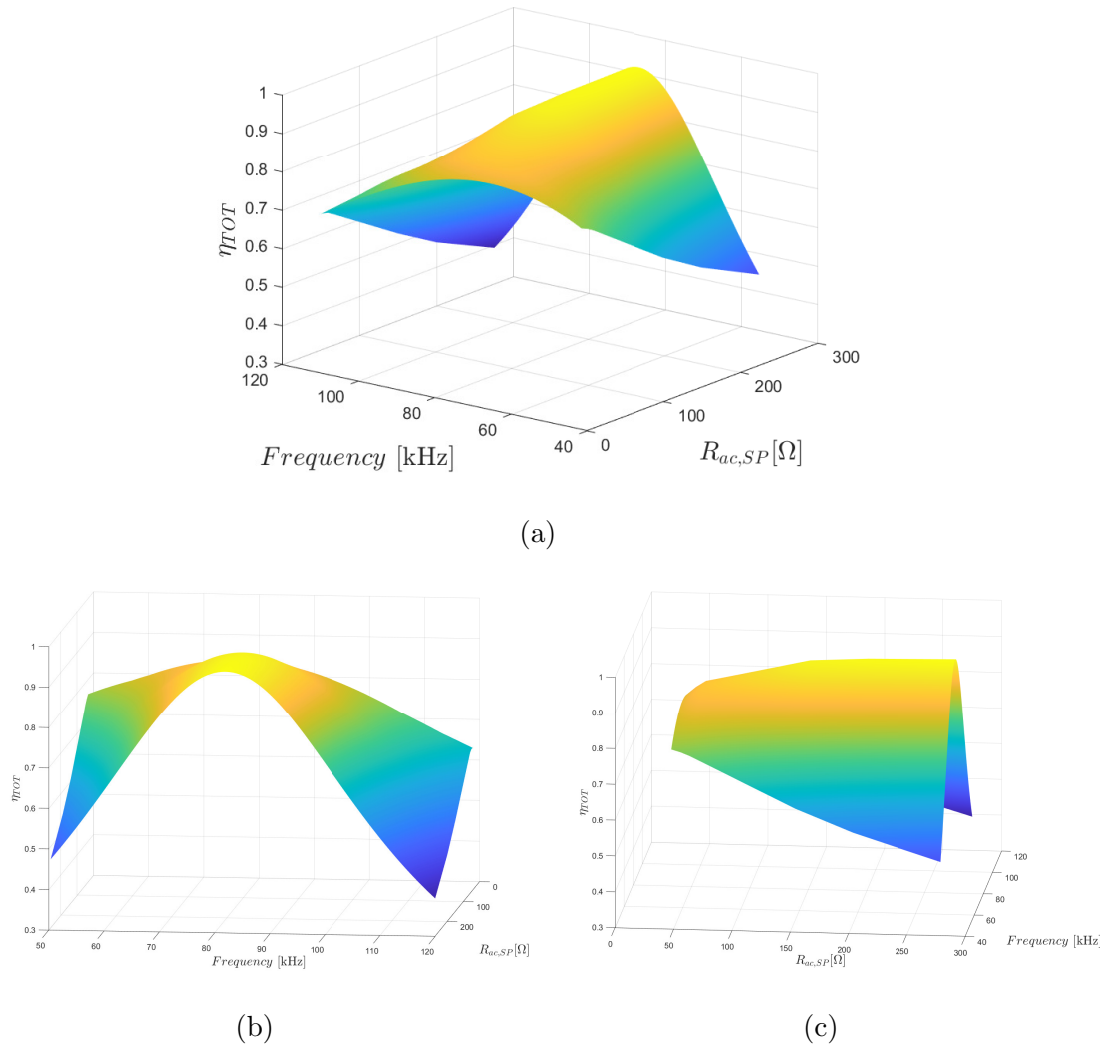


Figure 5.10: (a) 3D efficiency-frequency-load map for S-P compensation, while (b) highlights the frequency influence and (c) the load influence.

5.2.2 S-S Compensation

Similarly to S-P compensation, the same outcomes can also be illustrated for power electronic control of S-S compensation. Benchmarking the variation of frequency and phase-shift with respect to FC and PSC might be considered again the first result. Differently from S-P compensation, for this compensation topology the resonant frequency is 79 kHz and the load varies from 28Ω to 200Ω . Fig. 5.11a illustrates the frequency behavior of FC and HPSFC. The first difference is about the working frequency in the CC mode. Remembering that the transition from CC mode to CV

mode happens at $R_{ac} = 40\Omega$, it is noticeable the fact that FC works in a frequency range close to 87kHz - 88kHz, whereas HPSFC is much closer to resonance since it works in the range 80kHz - 82kHz. In addition, HPSFC keeps the frequency close to resonance, at 80kHz also at the beginning of CV mode, while FC increases the frequency up to almost 90 kHz. Then, from 90Ω to 140Ω the proposed control increases the frequency and, for very big loads, it basically works in the same working points as FC. Of course for matching the reference total gain G_{Tr} , and consequently the reference battery current, when the frequency of HPSFC is different from the FC, the phase-shift is different from zero. In fact, Fig. 5.11b proofs that up to 90Ω the HPSFC works close to resonance phase-shifting the inverter legs, while for big loads it works in the opposite way. In fact, for the last two sample points the phase-shift is really close to zero and the battery current is almost frequency controlled. It must be pointed out that the transition from working close to PSC and close to FC does not occur when passing from CC mode to CV mode.

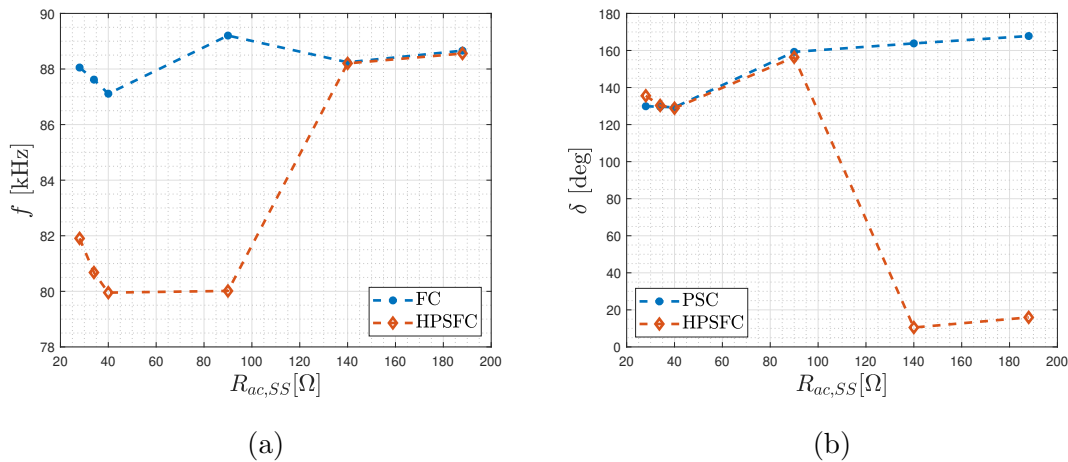


Figure 5.11: The resulting frequency and phase-shift value of the HPSFC are benchmarked with (a) FC and (b) PSC for S-S compensation.

Due to the logic of the proposed algorithm, the operating points are chosen according to a maximum efficiency criteria. In fact, looking at Fig. 5.12a it is understandable why the operating frequency is close to resonance for the first three sample points while the control system follows the reference signal with the phase-shift control. With the proposed control the efficiency for small loads increases up

to 1% with respect to the PSC, which is the reference control algorithm for small loads in S-S compensation, as confirmed by Fig. 5.12b. However, what turns out is the fact that in case of S-S compensation, for small loads is more convenient to work close to resonance and phase-shifting the inverter legs, while for big loads the trend is reserved. The HPSFC also presents benefits at very small loads, being 1% more efficient, and for medium load, which corresponds to the transition from PSC to FC, being also in this region 1% more efficient.

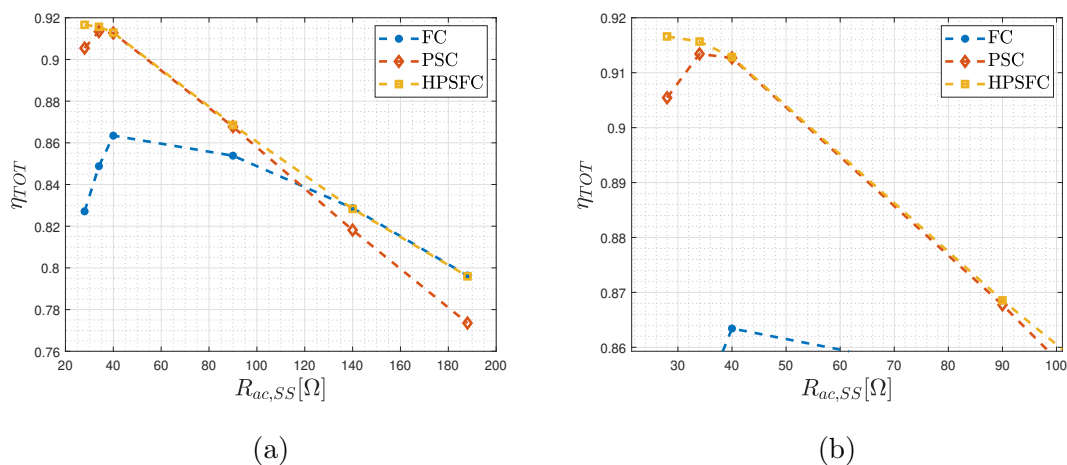
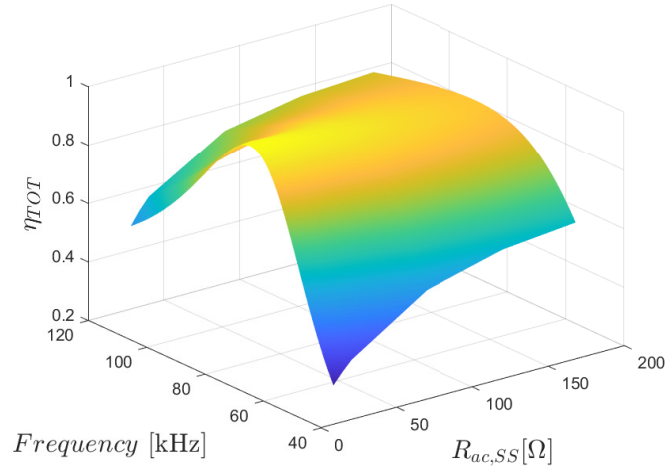


Figure 5.12: (a) Efficiency of the proposed HPSFC compared with stand-alone FC and PSC, while (b) highlights the improvement between HPSFC and PSC for S-S compensation.

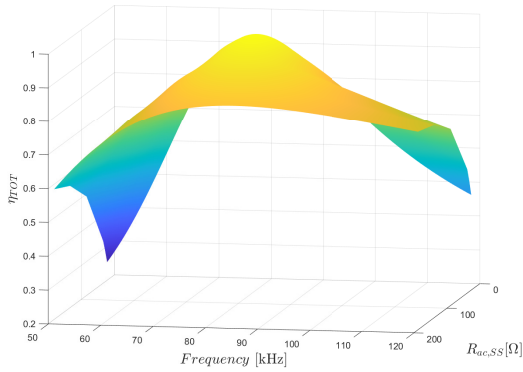
The total system efficiency is then 3D plotted in Fig. 5.13 as a function of the frequency (and therefore of the phase-shift) and the equivalent load resistance. According to the output results of the algorithm of the above cited picture, the efficiency of the S-S compensation:

- For small loads, as illustrated in the 3D map of Fig. 5.13b the efficiency is maximized at resonance and it peaks at value greater than 90%. However, the boundary points at maximum and minimum frequency peak at about 60% and 35%, respectively.
- For big loads, the efficiency is much more constant over the entire frequency span, however the peak efficiency at resonance is decreased up to 83%.

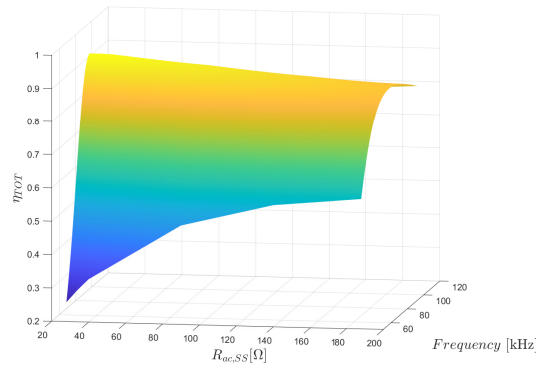
- The 3D map of Fig. 5.13c shows how the efficiency changes over the load range. In fact, at resonance the efficiency is much more constant and varies from 88% for big loads up to 95% for small loads. When the frequency tends to increase (or decrease) the trend is reversed).



(a)



(b)



(c)

Figure 5.13: (a) 3D efficiency-frequency-load map for S-P compensation, while (b) highlights the frequency influence and (c) the load influence for S-S compensation.

5.3 System Comparison

As highlighted in the previous sections and chapters, S-P compensation and S-S compensation behave in a different way with respect to the reference CC-CV charg-

ing cycle when considering the same battery pack. In the following, the main design and control differences between those topologies are presented.

The first difference refers to Tab. 3.4, in which it is noticeable the load variation between S-P to S-S. Taking as a benchmark the battery load variation, the S-S compensation exhibit a 19% less compared to it, while the S-P compensation is found to have 18% more.

For what concerns the parameters found in Chap. 3, even though the primary self-inductance of S-P compensation is one order of magnitude greater than S-S compensation, the secondary self-inductance is two order of magnitude lesser, Tab. 5.5. Additionally, the resonant tank outcomes presented in Sec. 5.1 shows the parameters dependency according to the reference quantities. Both compensations show the same trend with respect to the reference frequency for all the parameters. On the other hand, the sensitivity analysis with respect to the reference coupling coefficient returns that, while S-S compensation exhibits a decreasing trend for both inductances and increasing trend for both capacitances as k_0 increases, S-P compensations show a decreasing trend for L_1 and C_2 and a increasing trend for L_2 and C_1 . For what concerns the dependency on the reference load, for S-S the trend is opposite with respect to the previous case. S-P behaves similarly, Tab. 5.5.

Table 5.5: Comparison between resonant tank parameters of S-P and S-S compensation.

<i>Quantity</i>	<i>S-P</i>	<i>S-S</i>	<i>Unit of Measure</i>
ΔR_{ac}	44-293	28-200	Ω
L_1	3.4	0.336	mH
L_2	0.0735	0.503	mH
C_1	1.12	12.06	nF
C_2	50.5	8.06	nF

<i>Dependencies of Reference Parameters</i>			
<i>Quantity</i>	$f_0 \nearrow$	$k_0 \nearrow$	$R_0 \nearrow$
$L_{1,SS}$	\searrow	\searrow	\nearrow
$L_{2,SS}$	\searrow	\searrow	\nearrow
$C_{1,SS}$	\searrow	\nearrow	\searrow
$C_{2,SS}$	\searrow	\nearrow	\searrow
$L_{1,SP}$	\searrow	\searrow	\nearrow
$L_{2,SP}$	\searrow	\nearrow	\nearrow
$C_{1,SP}$	\searrow	\nearrow	\searrow
$C_{2,SP}$	\searrow	\searrow	\searrow

Also, in the same section it can be found that the efficiency is comparable, at resonance, as the load varies and peaks at about the range 96% – 97%, while it changes at the upper bound of SAE J2954 limit. In fact, while S-P loses only a percentage point at minimum load and therefore equals to 94%, S-S drops at 93%. However, these values are not fully representative for the choice of the resonant tank since it depends also on the control technique and operative working point.

The difference is more remarkable as the coupling coefficient changes. In fact, when k drops inside the range [0.15 – 0.25], S-S never drop below 92%, while S-P decreases up to 89%. The trend is even more accentuated when the coupling coefficient is very low, at $k = 0.1$.

However, to evaluate the performance of the WPT system, it must also be included the primary inverter control. In fact, by comparing the results it is noticeable that, for frequency control, the range variation of S-P is wider and it spans from 83.5kHz - 100.5kHz also exceeding the SAE J2954 range, while S-S is able to confine the frequency variation into the range 87kHz - 89kHz. This leads to have a decreasing trend efficiency from 72% to 66% for S-P, while for S-S it increases from 82kHz to 86.5kHz in the CC mode and decreases from 86.5% to 79.5% in CV mode, as shown in Fig. 5.9a and Fig. 5.12a.

Indeed, the phase-shift control shows good results for both compensations, having the efficiency in the range 77% – 88% for S-P and 77% – 91.5% for S-S. Also the phase-shift value is pretty similar for both, varying from $\simeq 120deg$ to $\simeq 165deg$ for S-P and from $\simeq 130deg$ to $\simeq 165deg$ for S-S.

Finally, the proposed hybrid control returns a narrow frequency range, especially for S-P compensation, which spans between 82kHz and 83.5kHz, while for S-S, having the resonance at 79kHz drops in the range 80kHz - 88kHz. Basically, the reason why it happens is because the S-P stays really close to resonance matching the reference total transconductance gain with the phase-shift. On the contrary, the S-S compensation of the control system uses the phase-shift and works close to resonance up to about an equivalent load resistance equal to 100Ω , from that value onwards, switching the controls works. As a result, the shape of the resulting efficiency is pretty different comparing both cases, as shown in Fig. 5.9a and Fig. 5.12a. In CC mode the efficiency increases from 78% to 82% for S-P, while for S-S it stays almost constant at about 91.5%. When entering in CV mode for S-P the efficiency increases from 83% to 89% when reaching an equivalent load equal to 150Ω , then decreases up to 81.5%, while for S-S the efficiency decreases from 91.5% to about 79.5%. The efficiency peaks at 89% in CV mode at 150Ω for S-P, while for S-S it peaks at 91.5% when the load is minimum, therefore at the beginning of CC mode. The considerations are summarized in Tab. 5.6.

Table 5.6: Efficiency comparison including resonant tank and primary inverter control, between S-P and S-S compensation.

	<i>Efficiency [%]</i>					
		$\Delta f [kHz]$	$\Delta \delta [deg]$	<i>CC Mode</i>	<i>CV Mode</i>	<i>Peak</i>
<i>FC</i>	S-P Comp.	83.5-100.5	-	66-72	66-24	72
	S-S Comp.	87-89	-	82-86.5	79.5-86.5	86.5
<i>PSC</i>	S-P Comp.	-	120-165	77-81	80-88	88
	S-S Comp.	-	130-165	90.5-91.5	77.5-91.5	91.5
<i>HPSFC</i>	S-P Comp.	82-83.5	2.5-165	78-82	81.5-89	89
	S-S Comp.	80-88	10-160	$\simeq 91.5$	79.5-91.5	91.5

5.3.1 Energy Assessment

In order to both validate the efficiency analysis above-mentioned and to assess which control techniques consumes less energy in a CC-CV charging cycle, an evaluation of the energy consumption is carried out hereinafter. By discrete modelling the battery power profile of Fig. 3.11 and integrating the area between two consecutive sample points, the cumulative energy comes out. Fig. 5.14a and Fig. 5.14b show the energy assessment for the three control methods, for S-S compensation and S-P compensation, respectively. Considering the BEV configuration of Tab. 3.3, the battery energy at full load results to be:

$$\begin{aligned}
 E &= N_s N_p C_{c, rated} V_{c, max} \\
 &\simeq 85 kW/h
 \end{aligned} \tag{5.1}$$

and it is taken as a reference profile. In fact, Fig. 5.14 compares the battery energy, which came from the power profile delivered to the battery pack considering the ideal system efficiency equal to one and displayed in light blue, with the energy delivered to the battery considering the whole system efficiency when subjected to FC, PSC, HPSFC and coloured in orange, yellow and violet with dotted line for S-S and S-P compensation, respectively. Therefore, the higher the whole system

efficiency, the closer a curve will be with respect to the reference battery energy.

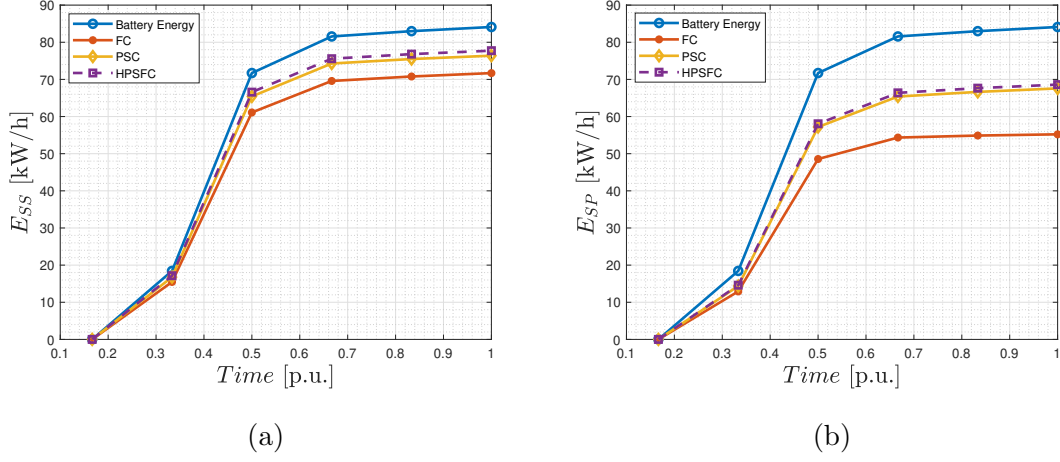


Figure 5.14: Cumulative energy assessment for (a) S-S compensation and for (b) S-P compensation. Time is normalized with respect to the time of end of charge.

In addition, it is also possible to normalize each cumulative energy curve with respect to the reference battery energy for obtaining, for each control technique and compensation topology, the normalized total energy in the CC-CV charging cycle. For S-S compensation their are calculated as:

$$\begin{aligned}
 E_{n,FC}^{SS} &= \frac{E_{tot,FC}^{SS}}{E_{batt,ref}} \\
 E_{n,PSC}^{SS} &= \frac{E_{tot,PSC}^{SS}}{E_{batt,ref}} \\
 E_{n,HPSFC}^{SS} &= \frac{E_{tot,HPSFC}^{SS}}{E_{batt,ref}}
 \end{aligned} \tag{5.2}$$

and for S-P compensation results to be:

$$\begin{aligned}
 E_{n,FC}^{SP} &= \frac{E_{tot,FC}^{SP}}{E_{batt,ref}} \\
 E_{n,PSC}^{SP} &= \frac{E_{tot,PSC}^{SP}}{E_{batt,ref}} \\
 E_{n,HPSFC}^{SP} &= \frac{E_{tot,HPSFC}^{SP}}{E_{batt,ref}}
 \end{aligned} \tag{5.3}$$

where E_{tot} is the total energy considering the system efficiency and E_n is the normalized total energy. $E_{batt,ref}$ corresponds to the BEV energy stored on-board

and it is equal to 85 kW/h. Tab. 5.7 collects the normalized energy values obtained from the above-cited formulas.

Table 5.7: Energy values for each control techniques, for both compensation topologies, normalized with respect to the reference battery energy of 85 kW/h.

E_n	$S-S[p.u.]$	$S-P[p.u.]$
Battery Reference	1	1
FC	0.8477	0.5929
PSC	0.8917	0.8147
HPSFC	0.9092	0.8274

The values of Tab. 5.7 are also depicted in a bar chart of Fig. 5.15. As it was predictable based on the efficiency results presented in the previous Sections, from a purely energy point of view, the S-S compensation achieves better results for all the control techniques. The HPSFC confirms to have the highest efficiency, and therefore it wastes less energy. The biggest energy difference between the two compensation topologies appears for FC, which is up to 2.5 [p.u], while for PSC and for HPSFC the difference is less accentuated and peaks at 0.8 [p.u].

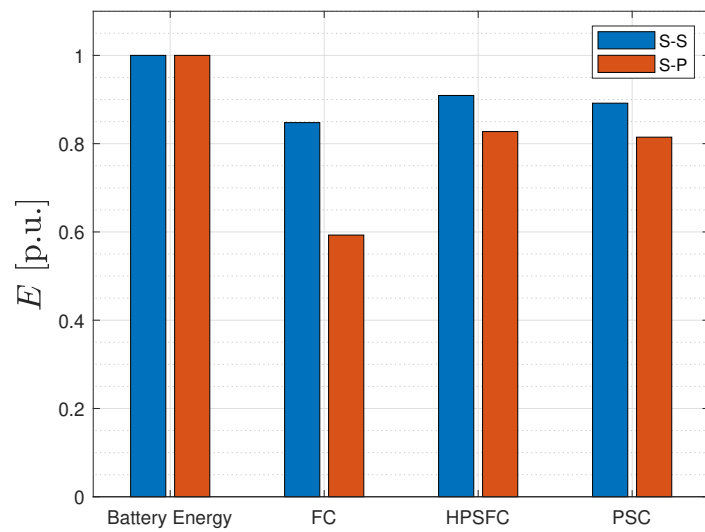


Figure 5.15: Bar chart in [p.u.]

Chapter 6

Conclusions and Future Work

6.1 Conclusions

The work presented in this thesis relies on two stages of the architecture of a WPT battery charger, covering analysis and design of the resonant tank as well as the optimization of the primary inverter control algorithm. Both stages are derived to be compliant with SAE J2954 standard. For industrial applications, the best trade off among number of components, complexity, size and reliability when selecting the compensation topology results to be the S-S compensation and the S-P compensation. In this regard, a general design procedure for maximizing the resonant tank efficiency has been presented. Contrary to what is usually found in literature, the presented design procedure outputs, in addition to optimum primary compensation capacitor $C_{1_{opt}}$ and secondary compensation capacitor $C_{2_{opt}}$, also the optimum value of primary-self inductance $L_{1_{opt}}$ and secondary-self inductance $L_{2_{opt}}$. The comparison showed that, although S-P compensation exhibits the primary self-inductance one order of magnitude higher, the secondary self-inductance results to be two orders of magnitude lower than S-S compensation.

The primary inverter has been controlled with an innovative control technique able to combine frequency control and phase-shift control. Given a reference compensation topology, a reference battery pack and a reference CC-CV charging profile, the algorithm creates a map for any working point and selects the best combinations of frequency and phase-shift couples that achieve maximum efficiency. Then, the

algorithm has been benchmarked with traditional controls to prove its effectiveness and applied to both compensation topologies.

Results showed that adopting the proposed control is possible to reduce the frequency range and to work closer to resonance, in order that the efficiency increases. In fact, with HPSFC the efficiency increases up to 1% with respect to the best performance of traditional controls in CC mode for both S-P and S-S, while in CV mode the proposed control gains 1.5% for S-P and 2% for S-S. This trend is also confirmed by the energy assessment. In addition, from a purely energy point of view the S-S compensation consumes less energy than the S-P compensation for all the three control techniques, saving up to 0.08 [p.u.] energy throughout the reference CC-CV charging cycle for the PSC and the HPSC and up to 2.5 [p.u.] for FC.

6.2 Future Work

With reference to the resonant tank, future developments would see the design procedure presented in this work applied on more complex compensation topologies, such as LCC-S or LCC-LCC, according to different target applications and different research purposes beyond the industrial field. The modular flowchart process based on close-form equations is well suited to further validate its generality and robustness.

Another wide area of improvement and development would be the extension of the presented primary inverter control technique for cutting-edge bidirectional WPT system architectures, in the context of V2G applications. For reaching that goal, the front-end bidirectional AC/DC converter along with the secondary side rectifier stage must be equipped with active switches as well as controlled by a proper algorithm to maximize efficiency and performance.

Bibliography

- [1] The Intergovernmental Panel on Climate Change, “IPCC report,” <https://www.ipcc.ch/sr15/>, accessed on 18/09/2022.
- [2] World Health Organization, “Air pollution,” <https://www.who.int/airpollution/ambient/en/>, accessed on 18/09/2022.
- [3] I. E. Agency, “EU - Energy, Climate change, Environment,” https://ec.europa.eu/clima/policies/transport_en, accessed on 18/09/2022.
- [4] —, “Global EV Outlook 2020,” <https://www.iea.org/reports/global-ev-outlook-2020>, accessed on 18/09/2022.
- [5] CAIT, “Climate data explorer via climate watch,” https://ec.europa.eu/clima/policies/eu-climate-action_en, accessed on 18/09/2022.
- [6] A. Khaligh and M. D’Antonio, “Global trends in high-power on-board chargers for electric vehicles,” *IEEE Transactions on Vehicular Technology*, vol. 68, no. 4, pp. 3306–3324, 2019.
- [7] X. Ding, J. Cheng, and F. Chen, “Impact of silicon carbide devices on the powertrain systems in electric vehicles,” *Energies*, vol. 10, no. 4, 2017. [Online]. Available: <https://www.mdpi.com/1996-1073/10/4/533>
- [8] V. Cirimele, M. Diana, F. Freschi, and M. Mitolo, “Inductive Power Transfer for Automotive Applications: State-of-the-Art and Future Trends,” *IEEE Transactions on Industry Applications*, vol. 54, no. 5, pp. 4069–4079, sep 2018.
- [9] D. Patil, M. K. McDonough, J. M. Miller, B. Fahimi, and P. T. Balsara, “Wireless Power Transfer for Vehicular Applications: Overview and Challenges,”

- IEEE Transactions on Transportation Electrification*, vol. 4, no. 1, pp. 3–37, Dec 2017.
- [10] G. A. Covic and J. T. Boys, “Modern trends in inductive power transfer for transportation applications,” *IEEE Journal of Emerging and Selected Topics in Power Electronics*, vol. 1, no. 1, pp. 28–41, 2013.
- [11] “Wireless Power Transfer for Light-Duty Plug-in/Electric Vehicles and Alignment Methodology,” SAEJ2954, 2016, http://standards.sae.org/j2954_201605/.
- [12] I. C. on Non-Ionizing Radiation Protection, “Guidelines for limiting exposure to time-varying electric and magnetic fields (1 Hz to 100 kHz),” *Health Physics*, vol. 99, pp. 818–836, 2010.
- [13] “Electrically Propelled Road Vehicles—Magnetic Field Wireless Power Transfer—Safety and Interoperability Requirements,” Document ISO/PAS 19363:2017, <https://www.iso.org/standard/64700.html>.
- [14] “Road Vehicles—Vehicle to Grid Communication Interface—Part 1: General Information and Use-Case Definition,” <https://www.iso.org/standard/55365.html>, accessed on 21/09/2022.
- [15] “Road Vehicles—Vehicle to Grid Communication Interface—Part 8: Physical Layer and Data Link Layer Requirements for Wireless Communication,” <https://www.iso.org/standard/62984.html>, accessed on 21/09/2022.
- [16] S. SAEJ2954, “SAE Taskforce J2954 on Wireless Charging and Positioning Standards Looking to Have Final Draft of Guideline This Year; Significant Industry Involvement,” <http://www.greencarcongress.com/2012/01/j2954-20120122.html>, accessed on 21/09/2022.
- [17] W. Zhang and C. C. Mi, “Compensation topologies of high-power wireless power transfer systems,” *IEEE Transactions on Vehicular Technology*, vol. 65, no. 6, pp. 4768–4778, 2016.

- [18] M. T. Outeiro, G. Buja, and D. Czarkowski, “Resonant power converters: An overview with multiple elements in the resonant tank network,” *IEEE Industrial Electronics Magazine*, vol. 10, no. 2, pp. 21–45, 2016.
- [19] J. Sallan, J. L. Villa, A. Llombart, and J. F. Sanz, “Optimal design of icpt systems applied to electric vehicle battery charge,” *IEEE Transactions on Industrial Electronics*, vol. 56, no. 6, pp. 2140–2149, 2009.
- [20] A. Khaligh and S. Dusmez, “Comprehensive topological analysis of conductive and inductive charging solutions for plug-in electric vehicles,” *IEEE Transactions on Vehicular Technology*, vol. 61, no. 8, pp. 3475–3489, 2012.
- [21] P. Knaup and K. Hasse, “Zero voltage switching converter for magnetic transfer of energy to movable systems,” in *European Conference on Power Electronics and Applications*, vol. 2. PROCEEDINGS PUBLISHED BY VARIOUS PUBLISHERS, 1997, pp. 2–168.
- [22] M. Simonazzi, A. Campanini, L. Sandrolini, and C. Rossi, “Design procedure based on maximum efficiency for wireless power transfer battery chargers with lightweight vehicle assembly,” *Energies*, vol. 15, no. 1, p. 70, 2021.
- [23] W. Zhang, S.-C. Wong, K. T. Chi, and Q. Chen, “An optimized track length in roadway inductive power transfer systems,” *IEEE Journal of Emerging and Selected Topics in Power Electronics*, vol. 2, no. 3, pp. 598–608, 2014.
- [24] C.-S. Wang, G. A. Covic, and O. H. Stielau, “General stability criterions for zero phase angle controlled loosely coupled inductive power transfer systems,” in *IECON’01. 27th Annual Conference of the IEEE Industrial Electronics Society (Cat. No. 37243)*, vol. 2. IEEE, 2001, pp. 1049–1054.
- [25] M. K. McDonough, *A multi-port power electronics interface for battery powered electric vehicles: Application of inductively coupled wireless power transfer and hybrid energy storage system*. The University of Texas at Dallas, 2014.
- [26] N. A. Keeling, G. A. Covic, and J. T. Boys, “A unity-power-factor ipt pickup for

- high-power applications,” *IEEE Transactions on Industrial Electronics*, vol. 57, no. 2, pp. 744–751, 2009.
- [27] A. Khaligh and S. Dusmez, “Comprehensive topological analysis of conductive and inductive charging solutions for plug-in electric vehicles,” *IEEE Transactions on Vehicular Technology*, vol. 61, no. 8, pp. 3475–3489, 2012.
- [28] J. M. Miller and B. R. Long, “What all technology adoptors should know about wpt for high power charging,” in *A Tutorial Presentation at IEEE PELs Workshop on Emerging Technologies: Wireless Power, WOW2016, Knoxville, TN*, 2016, pp. 4–6.
- [29] R. L. Steigerwald, “A comparison of half-bridge resonant converter topologies,” *IEEE transactions on Power Electronics*, vol. 3, no. 2, pp. 174–182, 1988.
- [30] Y. H. Sohn, B. H. Choi, E. S. Lee, G. C. Lim, G.-H. Cho, and C. T. Rim, “General unified analyses of two-capacitor inductive power transfer systems: Equivalence of current-source ss and sp compensations,” *IEEE Transactions on Power Electronics*, vol. 30, no. 11, pp. 6030–6045, 2015.
- [31] F. Grazian, T. B. Soeiro, and P. Bauer, “Inductive power transfer based on variable compensation capacitance to achieve an ev charging profile with constant optimum load,” *IEEE Journal of Emerging and Selected Topics in Power Electronics*, pp. 1–1, 2022.
- [32] Batemo Cell Library, “Molicel INR21700-P42B Datasheet,” <https://www.batemo.de/products/batemo-cell-library/molicel-inr21700-p42b/>, accessed on 27/09/2022.
- [33] X. Zhang, J. Lu, S. Yuan, J. Yang, and X. Zhou, “A novel method for identification of lithium-ion battery equivalent circuit model parameters considering electrochemical properties,” *Journal of Power Sources*, vol. 345, pp. 21–29, 2017.
- [34] A. Seaman, T.-S. Dao, and J. McPhee, “A survey of mathematics-based

- equivalent-circuit and electrochemical battery models for hybrid and electric vehicle simulation,” *Journal of Power Sources*, vol. 256, pp. 410–423, 2014.
- [35] S. S. Madani, E. Schaltz, and S. Knudsen Kær, “An electrical equivalent circuit model of a lithium titanate oxide battery,” *Batteries*, vol. 5, no. 1, 2019.
- [36] A. Nyman, T. G. Zavalis, R. Elger, M. Behm, and G. Lindbergh, “Analysis of the polarization in a li-ion battery cell by numerical simulations,” *Journal of The Electrochemical Society*, vol. 157, no. 11, p. A1236, 2010.
- [37] M. Simonazzi, L. Sandrolini, A. Campanini, J. Alberto, and A. Mariscotti, “Center-fed resonator array for increased misalignment tolerance in automotive wireless power transfer,” in *2022 IEEE 21st Mediterranean Electrotechnical Conference (MELECON)*, 2022, pp. 775–779.
- [38] K. Aditya and S. S. Williamson, “Comparative study of series-series and series-parallel compensation topologies for electric vehicle charging,” in *in Proc. IEEE 23rd International Symposium on Industrial Electronics (ISIE)*, Istanbul, Turkey, Jun. 1-4 2014, pp. 426–430.
- [39] V.-B. Vu, D.-H. Tran, and W. Choi, “Implementation of the constant current and constant voltage charge of inductive power transfer systems with the double-sided lcc compensation topology for electric vehicle battery charge applications,” *IEEE Transactions on Power Electronics*, vol. 33, no. 9, pp. 7398–7410, 2018.
- [40] Z. Huang, S.-C. Wong, and C. K. Tse, “Design methodology of a series-series inductive power transfer system for electric vehicle battery charger application,” in *in Proc. IEEE Energy Conversion Congress and Exposition (ECCE)*, Pittsburgh, PA, USA, Sept. 14-18 2014, pp. 1778–1782.
- [41] W. Zhang, S.-C. Wong, C. K. Tse, and Q. Chen, “Design for efficiency optimization and voltage controllability of series-series compensated inductive power transfer systems,” *IEEE Transactions on Power Electronics*, vol. 29, no. 1, pp. 191–200, 2014.

- [42] M. Simonazzi, A. Campanini, L. Sandrolini, and C. Rossi, "Single stage wireless power transfer battery charger for electric vehicles," in *2021 IEEE 15th International Conference on Compatibility, Power Electronics and Power Engineering (CPE-POWERENG)*, 2021, pp. 1–6.
- [43] R. Mai, Y. Chen, Y. Li, Y. Zhang, G. Cao, and Z. He, "Inductive power transfer for massive electric bicycles charging based on hybrid topology switching with a single inverter," *IEEE Transactions on Power Electronics*, vol. 32, no. 8, pp. 5897–5906, 2017.
- [44] G. Monti, M. Mongiardo, B. Minnaert, A. Costanzo, and L. Tarricone, "Multiple input multiple output resonant inductive wpt link: Optimal terminations for efficiency maximization," *Energies*, vol. 14, no. 8, 2021.
- [45] J. M. Stankiewicz, A. Choroszucho, and A. Steckiewicz, "Estimation of the maximum efficiency and the load power in the periodic wpt systems using numerical and circuit models," *Energies*, vol. 14, no. 4, 2021.
- [46] H. Weerasekara, K. Hata, T. Imura, H. Fujimoto, and Y. Hori, "Efficiency maximization in wireless power transfer systems for resonance frequency mismatch," in *in Proc. IEEE PELS Workshop on Emerging Technologies: Wireless Power Transfer (WoW)*, London, UK, Jun. 18-21 2019, pp. 363–366.
- [47] B. Pakhaliuk, V. Shevchenko, J. Mućko, O. Husev, M. Lukianov, P. Kołodziejek, N. Strzelecka, and R. Strzelecki, "Optimal rotating receiver angles estimation for multicoil dynamic wireless power transfer," *Energies*, vol. 14, no. 19, 2021.
- [48] M. Simonazzi, L. Sandrolini, L. Zarri, U. Reggiani, and J. Alberto, "Model of misalignment tolerant inductive power transfer system for ev charging," in *in Proc. IEEE 29th International Symposium on Industrial Electronics (ISIE)*, Delft, The Netherlands, June 17-19 2020, pp. 1617–1622.
- [49] T. Campi, S. Cruciani, F. Maradei, and M. Feliziani, "Conducted emission of wireless power transfer charging system in electric vehicle," in *in Proc. IEEE*

- International Symposium on Electromagnetic Compatibility*, Washington DC, USA, Aug. 7-11 2017, pp. 619–622.
- [50] G. Spadacini, F. Grassi, and S. A. Pignari, “Modelling and simulation of conducted emissions in the powertrain of electric vehicles,” *Progress In Electromagnetics Research B*, vol. 69, no. 1, pp. 1–15, 2016.
- [51] Z. M. Guilizzoni R., Harmon S., “Best practice guide for the assessment of emf exposure from vehicle wireless power transfer systems,” *16ENG08 EMPIR MICEV consortium*, 2021.
- [52] S. Cruciani, T. Campi, F. Maradei, and M. Feliziani, “Active shielding design and optimization of a wireless power transfer (wpt) system for automotive,” *Energies*, vol. 13, no. 21, 2020.
- [53] K. V. Schuylenbergh and R. Puers, *Inductive Powering: Basic Theory and Application to Biomedical Systems*, 1st ed. Springer Science, 2009.
- [54] V. Shevchenko, O. Husev, R. Strzelecki, B. Pakhaliuk, N. Poliakov, and N. Strzelecka, “Compensation topologies in ipt systems: Standards, requirements, classification, analysis, comparison and application,” *IEEE Access*, vol. 7, pp. 120 559–120 580, 2019.
- [55] Z. Pantic and S. M. Lukic, “Framework and topology for active tuning of parallel compensated receivers in power transfer systems,” *IEEE Transactions on Power Electronics*, vol. 27, no. 11, pp. 4503–4513, 2012.
- [56] D. Patil, M. Sirico, L. Gu, and B. Fahimi, “Maximum efficiency tracking in wireless power transfer for battery charger: Phase shift and frequency control,” in *2016 IEEE Energy Conversion Congress and Exposition (ECCE)*, 2016, pp. 1–8.
- [57] S. Samanta and A. K. Rathore, “Analysis and design of current-fed (l)(c) (lc) converter for inductive wireless power transfer (iwpt),” in *2015 IEEE Energy Conversion Congress and Exposition (ECCE)*, 2015, pp. 5724–5731.

- [58] —, “A new current-fed clc transmitter and lc receiver topology for inductive wireless power transfer application: Analysis, design, and experimental results,” *IEEE Transactions on Transportation Electrification*, vol. 1, no. 4, pp. 357–368, 2015.
- [59] —, “Wireless power transfer technology using full-bridge current-fed topology for medium power applications,” *IET Power Electronics*, vol. 9, no. 9, pp. 1903–1913, 2016. [Online]. Available: <https://ietresearch.onlinelibrary.wiley.com/doi/abs/10.1049/iet-pel.2015.0775>
- [60] A. Hu, J. Boys, and G. Covic, “Frequency analysis and computation of a current-fed resonant converter for icpt power supplies,” in *PowerCon 2000. 2000 International Conference on Power System Technology. Proceedings (Cat. No.00EX409)*, vol. 1, 2000, pp. 327–332 vol.1.
- [61] N. Xuan Bac, D. M. Vilathgamuwa, and U. K. Madawala, “A sic-based matrix converter topology for inductive power transfer system,” *IEEE Transactions on Power Electronics*, vol. 29, no. 8, pp. 4029–4038, 2014.
- [62] H. L. Li, A. P. Hu, and G. A. Covic, “A direct ac–ac converter for inductive power-transfer systems,” *IEEE Transactions on Power Electronics*, vol. 27, no. 2, pp. 661–668, 2012.
- [63] M. Bojarski, E. Asa, K. Colak, and D. Czarkowski, “Analysis and control of multiphase inductively coupled resonant converter for wireless electric vehicle charger applications,” *IEEE Transactions on Transportation Electrification*, vol. 3, no. 2, pp. 312–320, 2017.
- [64] —, “A 25 kw industrial prototype wireless electric vehicle charger,” in *2016 IEEE Applied Power Electronics Conference and Exposition (APEC)*, 2016, pp. 1756–1761.
- [65] A. Daga, J. M. Miller, B. R. Long, R. Kacergis, P. Schrafel, and J. Wolgemuth, “Electric fuel pumps for wireless power transfer: Enabling rapid growth in the

- electric vehicle market,” *IEEE Power Electronics Magazine*, vol. 4, no. 2, pp. 24–35, 2017.
- [66] B. X. Nguyen, D. M. Vilathgamuwa, G. Foo, A. Ong, P. K. Sampath, and U. K. Madawala, “Cascaded multilevel converter based bidirectional inductive power transfer (bipt) system,” in *2014 International Power Electronics Conference (IPEC-Hiroshima 2014 - ECCE ASIA)*, 2014, pp. 2722–2728.
- [67] H. Hao, G. A. Covic, and J. T. Boys, “A parallel topology for inductive power transfer power supplies,” *IEEE Transactions on Power Electronics*, vol. 29, no. 3, pp. 1140–1151, 2014.
- [68] Y. Li, R. Mai, M. Yang, and Z. He, “Cascaded multi-level inverter based ipt systems for high power applications,” *Journal of Power Electronics*, vol. 15, no. 6, pp. 1508–1516, 2015.
- [69] Y. Wei, Q. Luo, and A. Mantooh, “Overview of modulation strategies for llc resonant converter,” *IEEE Transactions on Power Electronics*, vol. 35, no. 10, pp. 10 423–10 443, 2020.
- [70] R. Bosshard, U. Badstübner, J. W. Kolar, and I. Stevanović, “Comparative evaluation of control methods for inductive power transfer,” in *2012 International Conference on Renewable Energy Research and Applications (ICRERA)*, Nagasaki, Japan, Nov. 11-14, 2012, pp. 1–6.
- [71] C.-S. Wang, O. Stielau, and G. Covic, “Design considerations for a contactless electric vehicle battery charger,” *IEEE Transactions on Industrial Electronics*, vol. 52, no. 5, pp. 1308–1314, Sep. 2005.
- [72] Y. Liu, U. K. Madawala, R. Mai, and Z. He, “Control of wireless power transfer systems under large coil misalignments,” in *2019 IEEE 15th Brazilian Power Electronics Conference and 5th IEEE Southern Power Electronics Conference (COBEP/SPEC)*, Santos, Brazil, 1-4 Dec., 2019, pp. 1–4.
- [73] H. Wu, X. Zhan, and Y. Xing, “Interleaved llc resonant converter with hybrid rectifier and variable-frequency plus phase-shift control for wide output voltage

- range applications,” *IEEE Transactions on Power Electronics*, vol. 32, no. 6, pp. 4246–4257, 2017.
- [74] A. Koran and K. Badran, “Adaptive frequency control of a sensorless-receiver inductive wireless power transfer system based on mixed-compensation topology,” *IEEE Transactions on Power Electronics*, vol. 36, no. 1, pp. 978–990, Jun. 2021.
- [75] C. Baguley, S. Jayasinghe, and U. Madawala, “Chapter 22 - theory and control of wireless power transfer systems,” in *Control of Power Electronic Converters and Systems*, F. Blaabjerg, Ed. Academic Press, 2018, pp. 291–307.
- [76] S. M. S. I. Shakib and S. Mekhilef, “A frequency adaptive phase shift modulation control based llc series resonant converter for wide input voltage applications,” *IEEE Transactions on Power Electronics*, vol. 32, no. 11, pp. 8360–8370, Dec. 2017.
- [77] A. Campanini, M. Simonazzi, M. Bosi, and C. Rossi, “Design and comparison between psfb and llc 400/48v dc/dc stage for on-board battery charger during total and partial cc-cv charging cycles,” in *2022 IEEE 21st Mediterranean Electrotechnical Conference (MELECON)*, 2022, pp. 1102–1106.
- [78] Y. Chen, J. Xu, Y. Gao, L. Lin, J. Cao, and H. Ma, “Analysis and design of phase-shift pulse-frequency-modulated full-bridge lcc resonant converter,” *IEEE Transactions on Industrial Electronics*, vol. 67, no. 2, pp. 1092–1102, 2019.
- [79] Y. Jiang, J. Liu, X. Hu, L. Wang, Y. Wang, and G. Ning, “An optimized frequency and phase shift control strategy for constant current charging and zero voltage switching operation in series-series compensated wireless power transmission,” in *2017 IEEE Energy Conversion Congress and Exposition (ECCE)*, 2017, pp. 961–966.
- [80] J. Byun, M. Kim, D. Joo, W.-Y. Lee, G.-Y. Choe, and B. K. Lee, “Frequency and phase-shift control of inductive power transfer for ev charger with llc-ls

- resonant network considering misalignment,” *Journal of Electrical Engineering & Technology*, vol. 14, no. 6, pp. 2409–2419, 2019.
- [81] Y. Jiang, L. Wang, Y. Wang, J. Liu, M. Wu, and G. Ning, “Analysis, design, and implementation of wpt system for ev’s battery charging based on optimal operation frequency range,” *IEEE Transactions on Power Electronics*, vol. 34, no. 7, pp. 6890–6905, 2019.
- [82] A. Babaki, S. Vaez-Zadeh, A. Zakerian, and G. A. Covic, “Variable-frequency retuned wpt system for power transfer and efficiency improvement in dynamic ev charging with fixed voltage characteristic,” *IEEE Transactions on Energy Conversion*, vol. 36, no. 3, pp. 2141–2151, 2021.
- [83] T. Zhu, F. Zhuo, F. Zhao, F. Wang, H. Yi, and T. Zhao, “Optimization of extended phase-shift control for full-bridge clc resonant converter with improved light-load efficiency,” *IEEE Transactions on Power Electronics*, vol. 35, no. 10, pp. 11 129–11 142, 2020.
- [84] J.-H. Kim, C.-E. Kim, J.-K. Kim, J.-B. Lee, and G.-W. Moon, “Analysis on load-adaptive phase-shift control for high efficiency full-bridge llc resonant converter under light-load conditions,” *IEEE Transactions on Power Electronics*, vol. 31, no. 7, pp. 4942–4955, 2016.
- [85] J.-Y. Lee, Y.-S. Jeong, and B.-M. Han, “An isolated dc/dc converter using high-frequency unregulated llc resonant converter for fuel cell applications,” *IEEE Transactions on Industrial Electronics*, vol. 58, no. 7, pp. 2926–2934, 2011.